Feary, D.A., Hine, A.C., Malone, M.J., et al., 2000
Proceedings of the Ocean Drilling Program, Initial Reports Volume 182

4. Site 1126[1]

Shipboard Scientific Party[2]

BACKGROUND AND OBJECTIVES

Site 1126 is located on the eastern Eyre Terrace upper slope in 783.8 m of water (Fig. F1). This site was designed to intersect Cenozoic seismic Sequences 2, 3, and 4 and Lobes 1 and 3 of Sequence 6A (Feary and James, 1998, reprinted as Chap. 2) and to intersect as much of the upper part of the Cretaceous section as time permitted (Fig. F2). The target depth at this site was a high-amplitude reflector of probable Cenomanian age, estimated before drilling (on the basis of stacking velocities) to be at 525 meters below seafloor (mbsf). Because this was also the first ODP site in this basin, it provided the opportunity to establish a basic stratigraphy for the Cenozoic sequences that could then be refined at later sites.

The principal objectives at this site were (1) to collect a detailed record of Paleogene–lower Neogene temperate to subtropical midlatitude sedimentation in an upper slope environment and (2) to recover a record of marine flooding of the evolving rift basin in Cenomanian time. Seismic interpretation (Feary and James, 1998, reprinted as Chap. 2) indicated that the lowermost Cenozoic sequence at this site (Sequence 6A) should be broadly contemporaneous with the Eocene?–middle? Miocene carbonate platform exposed on land and underlying the modern mid-inner shelf. Although seismic data show that a significant portion of this time interval (Sequence 6A, Lobe 2) is missing at this location, Site 1126 represents an ideal opportunity to sample the upper (Lobe 3) and lowermost (Lobe 1) parts of the deep-water sequence deposited apparently contemporaneous with this platform. Despite the absence of Lobe 2 at this location, it is likely that these deeper water deposits should contain a more complete sequence than coeval shallow-water sediments, without lowstand hiatuses.

This site also constitutes an upper slope component of the Leg 182 shelf-to-basin transect, designed to address a number of paleoceano-

F1. Map showing Site 1126 in relation to other Leg 182 sites and the AGSO169 site-survey seismic lines, p. 46.

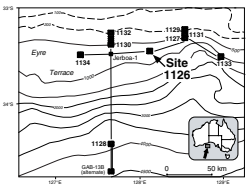

F2. Portion of seismic Line AGSO169/03g showing seismic stratigraphic sequences at Site 1126, p. 47.

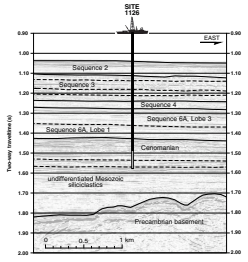

[1]Examples of how to reference the whole or part of this volume.
[2]Shipboard Scientific Party addresses.

Ms 182IR-104

graphic problems: (1) the relationship between circulation patterns in the deep ocean and on the shelf during times of warm vs. cold oceanic conditions, (2) the precise timing and nature of the opening of the Tasman Gateway, (3) the evolution and effect of the Leeuwin Current, and (4) the relationship between primary productivity and cool-water carbonate development. In addition, Site 1126 presented an opportunity to use in situ heat-flow measurements (using a combination of Adara temperature tool and Davis-Villinger temperature probe [DVTP]) integrated with core thermal conductivity data to characterize the heat flow regime in the eastern Eyre Terrace.

The relatively thin Cenozoic sequence at this location offered an opportunity to recover the uppermost part of the Mesozoic section, shown to be of Cenomanian age in the nearby Jerboa-1 exploration well. Although Jerboa-1 yielded a record of this interval in the form of ditch-cutting fragments, a fully cored section through this interval was sought to clarify facies relationships and the biostratigraphy of this nearshore marine interval.

Summary of Objectives for Site 1126

The principal drilling objectives at Site 1126 were to

1. Collect a detailed record of Paleogene–lower Neogene temperate to subtropical midlatitude sediments deposited as lowstand sediment lobes in an upper slope environment;
2. Contribute an upper slope component to the shelf-to-basin paleoceanographic transect;
3. Evaluate sea-level control on Neogene facies within an upper slope setting; in particular, to evaluate stratigraphic response to eustatic oscillations by comparison with equivalent time intervals in shelf and deep oceanic settings;
4. Determine diagenetic history and processes within Neogene upper slope facies; and
5. Collect a record of marine flooding of the evolving rift basin between Australia and Antarctica since the Cenomanian.

OPERATIONS

Port Call Activities and Transit to Site 1126 (GAB-04B)

Leg 182 officially began at 1000 hr on 8 October 1998 with the first line ashore in Wellington, New Zealand, ending Leg 181. All subsequent times in this volume are local time (e.g., Universal Time Coordinated + 8 hr for the Leg 182 operational area), unless otherwise noted. Leg 181 had been extended 12 hr, shortening the time available to complete port call activities for Leg 182 despite the vessel's eventual early arrival. After completion of most of the port call activities, the ship's departure was scheduled for 0800 hr on 13 October. However, we were delayed further by a storm with sustained winds of 45 kt, gusting to 60 kt.

The storm moderated overnight to 25-kt winds with 35-kt gusts, and the ship departed at 0809 hr on 14 October. We quickly encountered the first of numerous gale-force storms, and the ship's course was diverted several times to the north to avoid the strength of the storms and to maintain speed. Much of the transit across the Tasman Sea en-

countered nearly continuous high seas and swells (as high as 9 m) with green water and spray over the bow and an opposing current (~1 kt) and winds (25–50 kt). The weather did not moderate for more than a few hours at a time until the ship passed through Bass Strait into the Great Australian Bight. Propulsion motor P-17B failed with armature problems on the transit and was inoperable for the rest of the leg. The 2375-nmi sea voyage required 11.8 days (8.4 kt average) instead of the 8.7 days (at 10.5 kt) that was projected precruise. The longer transit time, combined with the extra day spent in Wellington waiting on the weather, forced the decision to shift the initial site from prospectus site GAB-03B to GAB-04B. GAB-03B was dropped to alternate status.

Hole 1126A

A positioning beacon was launched at 2257 hr on 25 October to initiate Site 1126. The ship was stabilized on position, and an advanced hydraulic piston core/extended core barrel (APC/XCB) bottom-hole assembly (BHA) was run to 796 meters below rig floor (mbrf), and Hole 1126A was spudded at 0530 hr on 26 October. Core 1H recovered 9.69 m, which was not appropriate for establishing a good mudline. The bit was repositioned to take another mudline core, ending Hole 1126A at 0600 hr on 26 October.

Hole 1126B

The ship was not moved, and Hole 1126B was spudded at 0630 hr on 26 October. The bit was positioned at 792 mbrf, and Core 1H recovered 6.56 m, indicating the seafloor was at 783.8 meters below sea level (mbsl). The APC coring advanced to 104.0 mbsf, orienting Cores 3H to 11H (Table T1). Cores 10H to 12H encountered chert horizons, causing only partial strokes of the piston. The APC shoe was damaged during firing of Core 12H, bending the cutting shoe and plugging the nozzles in the core bit. The next APC coring attempt failed despite firing pressures of 3000 psi with the bit at 1 m off bottom; therefore, an XCB bit was dropped to deplug the throat of the drilling bit. This configuration allows water to circulate through the XCB core barrel during drilling and wash away any soft material. Thus, Core 13W (104.0–109.5 mbsf) was considered a wash interval; however, a few pieces of chert were recovered (0.2 m) and curated.

T1. Site 1126 coring summary, p. 85.

The APC coring resumed from 109.5 to 124.5 mbsf with Core 15H encountering chert layers and bending another APC shoe. The XCB bit was dropped again, and the chert interval (124.5–128.8 mbsf) was washed with no recovery. The APC coring advanced to 160.3 mbsf (Core 20H) before penetration was again prevented by chert horizons. The DVTP was deployed after Core 19H, but the ship's heave prevented quality data collection. Coring continued with the XCB to 263.3 mbsf (Core 32X; Table T1) and was terminated when the last four coring runs destroyed both hard and soft XCB cutting shoes. The bit was pulled and cleared the seafloor at 1415 hr on 27 October.

Hole 1126C

The ship was moved 20 m east of Hole 1126B, and Hole 1126C was spudded at 1540 hr on 27 October. The bit was positioned at 794 mbrf, and Core 1H recovered 8.48 m, indicating a water depth of 783.8 m. The APC coring advanced to the approximate depth of the chert hori-

zons found in Hole 1126A. Cores 3H through 9H were oriented and Adara tool heat-flow measurements were made during Cores 4H, 6H, and 8H. As with the DVTP, the heave from long-period swell disturbed all three Adara tool runs. Coring continued with the XCB from 84.5 to 138.4 mbsf through the chert-rich intervals. We switched back to APC coring for Core 16H; however, the core was a partial stroke (6.0 m) and the APC shoe had been dented severely. A final XCB core (17X) was cut from 144.4 to 154.0 mbsf with 46% recovery (Table T1). The bit was pulled and cleared the rotary at 0615 hr on 28 October, ending Hole 1126C.

Hole 1126D

A rotary core barrel (RCB) BHA was run to the seafloor, which was tagged at 795.0 mbrf (783.8 mbsl). The hole was drilled from 0 to 150.0 mbsf at 42.9 m/hr with a center bit in place. The interval from 150.0 to 463.3 mbsf was RCB cored (Cores 1R–33R; Table T1) with 12.9% recovery. Recovery was poorest in soft nannofossil oozes interbedded with chert because of chert blocking the throat of the bit or jamming in the core catcher and preventing softer material from entering the core barrel. The recovery increased to ~22% below 350 mbsf as the induration increased.

After coring was terminated, the hole was prepared for logging, which included a wiper trip to 107 mbsf, circulation of a sepiolite mud pill, and release of the bit. The drill pipe was pulled to 117 mbsf, which placed the end of pipe below the first prominent chert layer to protect the logging tools and wireline in anticipated high-heave conditions. The triple combination (triple combo) logging string was run from 441 mbsf (22 m off bottom) to the end of pipe at 117 mbsf. During logging, the wireline heave compensator (WHC) occasionally reached its maximum stroke of 6 m. The caliper on the triple combo showed that hole conditions were poor with prominent washouts. To protect the tool from damage, the Formation MicroScanner (FMS) was not deployed in these conditions. Therefore, the sonic tool was combined with the geologic high-resolution magnetic tool (GHMT; magnetic susceptibility [MS] only; total field was inoperable), and the tool string was run from 440 mbsf to the mudline. In the final logging run, the generator-injector air gun and the well seismic tool (WST) were deployed for a checkshot survey. The drill pipe cleared the rig floor at 1530 on 30 October, ending operations at Site 1126.

LITHOSTRATIGRAPHY

Introduction

Site 1126 is located at a water depth of 783.8 m on the eastern Eyre Terrace. It provided a record of middle Eocene–Pleistocene sedimentation in a middle to upper slope depositional setting.

Two major sedimentary packages form the succession. A lower package consists of siliciclastic sediments of unknown age (Fig. F3). These sediments were probably deposited in a marginal marine setting, as indicated by occurrences of bioturbation. Comparison of the general lithologic succession at Site 1126 with stratigraphically equivalent deposits recovered from borehole Jerboa-1 (Bein and Taylor, 1981) indi-

F3. Summary of sediments and lithostratigraphy, p. 48.

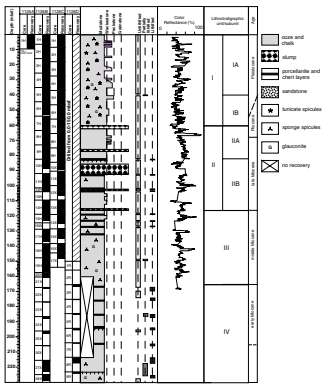

cates that these siliciclastics are probably Cretaceous (Cenomanian) in age.

The upper sedimentary package at Site 1126 consists of middle Eocene–Pleistocene (see "Biostratigraphy," p. 12) marine pelagic carbonates. These sediments consist of calcareous ooze, silicified calcareous chalk, silicified limestone, and slumped calcareous ooze.

Based on major sediment types, compositional changes, and sediment deformation structures, five lithostratigraphic units are differentiated. Because the core recovery at Site 1126 was good within the uppermost 160 m, the level of confidence for the placement of these boundaries in this part of the succession is high. Below 160 mbsf, however, core recovery was so poor that it was not feasible to differentiate separate units; therefore, sediments between 160 mbsf and the top of the sandstones (Fig. F3) were placed into one unit. Further division of this Unit IV into at least three subunits is indicated by variations in the downhole logs (see "Downhole Measurements," p. 35).

Lithostratigraphic Units

Unit I

Intervals: Core 182-1126A-1H; Core 182-1126B-1H through Section 7H-5, 20 cm; Core 182-1126C-1H through Section 7H-3, 19 cm
Depth: 0–9.50 mbsf (Hole 1126A); 0–60.21 mbsf (Hole 1126B); 0–59.16 mbsf (Hole 1126C)
Age: Pleistocene

Unit I consists of ooze with varying amounts of calcareous nannofossils and planktonic foraminifers. Unit I is divided into two subunits on the basis of textural changes, different patterns of sediment alternation, and the presence of a slightly indurated layer in Cores 182-1126B-5H and 182-1126C-5H.

Subunit IA

Intervals: Core 182-1126A-1H; Core 182-1126B-1H through Section 5H-4, 60 cm; Core 182-1126C-1H through Section 5H-2, 120 cm
Depth: 0–9.50 mbsf (Hole 1126A); 0–39.05 mbsf (Hole 1126B); 0–39.70 mbsf (Hole 1126C)
Age: Pleistocene

The calcareous ooze of Subunit IA is characterized by a textural alternation between wackestone and packstone. Mud-supported intervals are light gray in color, whereas grain-supported parts are slightly darker and more greenish.

Matrix is dominated by calcareous nannofossils, accessory tunicate spicules, and sponge spicules. Components in the >63-µm fraction consist of abundant planktonic foraminifers, frequent benthic foraminifers, bioclasts, echinoid spines, blackened grains, and rare ostracodes. Glauconite occurs infilling planktonic foraminifers and as isolated grains. There are no major compositional differences in coarse fraction composition between mud- and grain-supported intervals. Macrofossils are rare, represented by large pteropods and scaphopods as well as minor gastropods.

The major part of the subunit consists of matrix-supported sediment with seven major grain-supported intervals, each as thick as 1.50 m (Fig. F3). Textural changes between matrix- and mud-supported intervals are gradational throughout the entire subunit. Comparison of the natural gamma-ray curve (see "Physical Properties," p. 33) with the succession seen in the cores shows that the darker, coarser layers correlate with high gamma-ray values.

These sediments are moderately to strongly bioturbated throughout. Bioturbation is manifest as lighter to darker gray color mottling. Burrows of the latter color are best expressed at the transition from darker matrix-supported to lighter grain-supported intervals (e.g., interval 182-1126C-1H-4, 85–110 cm). These burrows, having diameters as large as 4 cm, are interpreted as *Thallasinoides* traces.

Subunit IB

Intervals: Sections 182-1126B-5H-4, 60 cm, through 7H-5, 20 cm; Sections 182-1126C-5H-2, 120 cm, through 7H-3, 19 cm
Depth: 39.05–60.21 mbsf (Hole 1126B); 39.70–59.16 mbsf (Hole 1126C)
Age: late Pliocene–Pleistocene

The contact between Subunits IA and IB is at the sharp contact between a lower white gray nannoplankton ooze to chalk and an upper light gray nannoplankton ooze. This boundary is recognized in both drill holes. The fact that the deposits underlying this boundary are slightly more lithified may indicate that this layer represents an early diagenetically consolidated horizon. Texture of the deposits is dominantly matrix supported (wackestone texture), with only minor grain-supported (packstone) intervals.

As in Subunit IA, the major components of the matrix are calcareous nannoplankton, together with tunicate and sponge spicules. Isolated dolomite rhombs are present in some of the smear slides (see "Site 1126 Smear Slides," p. 80). Components of the >63-µm fraction are abundant planktonic foraminifers, frequent echinoid spines, sponge spicules, blackened grains, and minor benthic foraminifers. Glauconite occurs as infill of planktonic foraminifers, but also as isolated grains. As visually estimated, glauconite may represent as much as 20% of the coarse-grained fraction. Macrofossils are rare throughout the subunit: a solitary azooxanthellate coral is present in interval 182-1126B-5H-5, 134–147 cm (Fig. F4). Other macrofossils are large echinoid spines and plates, small gastropods, pteropods, and serpulids.

Contacts between the whitish gray matrix-supported sediments and the light gray grain-supported intervals are gradational. Changes in color and texture, however, occur over shorter intervals than in Subunit IA.

The sediments of Subunit IB are moderately to strongly bioturbated. Burrowing occurs as diffuse color mottling, but burrows of the youngest tiers are better expressed in transitional areas between lithologies. Sediment in these burrows is coarser grained than the surrounding sediment. Such infilling sediments have a packstone texture, and many of the burrows are rich in glauconitic grains.

F4. Solitary azooxanthellate coral, Hole 1126B, p. 50.

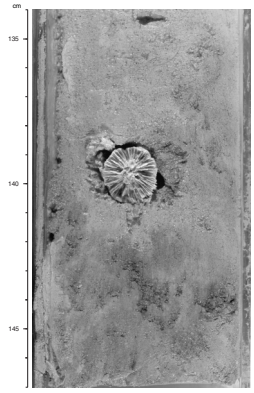

Unit II

Intervals: Sections 182-1126B-7H-5, 20 cm, through 14H-5, 125 cm; Sections 182-1126C-7H-3, 19 cm, through 13X-5, 82 cm

Depth: 60.21–116.75 mbsf (Hole 1126B); 59.16–116.32 mbsf (Hole 1126C)
Age: late Miocene–Pliocene

Unit II consists of ooze with varying amounts of calcareous nannofossils and planktonic foraminifers. The top and the base of the unit are defined by sediment deformation structures interpreted as slumps (Fig. F5). The position of these bodies (Fig. F3) provides a minimum estimate of thickness, as only the slumped parts with inclined bedding can be unequivocally recognized in the cores. The interpretation of the inclined layers as slumps is corroborated by the poor overall correlation of the deposits of Unit II between Holes 1126B and 1126C, suggesting significant lateral inhomogeneity (see "Composite Depths," p. 26). Division of Unit II into two subunits relies on the first downhole occurrence of a silicified layer.

F5. Inclined, deformed beds, Hole 1126B, p. 51.

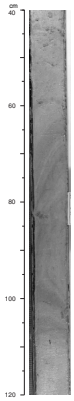

Subunit IIA

Intervals: Sections 182-1126B-7H-5, 20 cm, through 9H-CC; Sections 182-1126C-7H-3, 19 cm, through 9H-5, 85 cm
Depth: 60.21–82.01 mbsf (Hole 1126B); 59.16–81.85 mbsf (Hole 1126C)
Age: late Miocene–Pliocene

The calcareous ooze of Subunit IIA has a wackestone to packstone texture. As in the overlying deposits, matrix-supported intervals are white gray in color, whereas grain-supported deposits are light gray.

The matrix of the sediment consists of calcareous nannofossils together with traces of quartz and clay. A high proportion of siliciclastic components in the matrix (quartz, mica, pyroxene, and clay minerals) occurs in Section 182-1126C-7H-3, 20 cm. The >63-µm sediment fraction in Subunit IIA consists of planktonic foraminifers, 5%–10% glauconite, and minor benthic foraminifers. The only macrofossils recorded in this subunit are mollusk debris in the upper 20 cm of Section 182-1126B-7H-6. As in the overlying lithostratigraphic units, white-gray matrix-supported layers alternate with light gray grain-supported intervals.

Bioturbation is moderate to strong throughout. It occurs as color mottling with some mottles surrounded by green to dark gray/black reduction halos. Burrows of the uppermost tier are represented by minor *Chondrites* and indeterminate large subvertical round burrows.

Two slumped layers are present. They are best represented in Hole 1126B. The upper layer is in Core 182-1126B-7H; the lower one is in Core 182-1126B-9H (Fig. F5). Texture and composition of the slumped sediments are similar to overlying and underlying sediments, pointing to local provenance of the slumped deposits.

A distinct type of sediment occurs in Section 182-1126B-7H-5, 102 cm, through 8H-1, 66 cm. These deposits have a wackestone to packstone texture and contain lithified chalky lumps as large as 1.5 cm in size. Such lumps are subrounded to very irregular nannofossil chalk. The lumps float in the nannofossil ooze matrix, suggesting a mass-flow origin for these deposits.

Subunit IIB

Intervals: Sections 182-1126B-10H-1 through 14H-5, 125 cm; Sections 182-1126C-9H-5, 85 cm, through 13X-5, 82 cm

Depth: 82.01–116.75 mbsf (Hole 1126B); 81.85–116.32 mbsf (Hole 1126C)
Age: late Miocene

The upper boundary of this subunit is characterized by the first downhole occurrence of silicified layers and the presence of a firmground. The first in situ porcellanite/chert is in interval 182-1126B-10H, 93–104 cm. Silicified rock fragments, however, are also present as downhole contamination in the topmost 10 cm of the core, suggesting the presence of uphole porcellanite/chert. As such, the upper limit of Subunit IIB in Hole 1126B was placed at the bottom of the core catcher of Core 182-1126B-9H. In Hole 1126C, the first silicified layer occurs in interval 182-1126C-9H, 0–11 cm. A firmground is present 1.69 m above this layer in Section 182-1126C-9H-5, 85 cm. The position of this firmground defines the upper limit of Subunit IIB in Hole 1126C.

The deposits of Subunit IIB are calcareous oozes with interbedded silicified layers. Silicified intervals are irregular to nodular porcellanites. The matrix of the oozes is dominated by calcareous nannofossils with minor sponge spicules. The >63-µm fraction contains abundant planktonic foraminifers, benthic foraminifers, sponge spicules, pyrite grains, and glauconite. As in the overlying deposits, lighter and darker intervals alternate throughout this subunit. No macrofossils were recorded in the cores.

The deposits of Subunit IIB are moderately to strongly bioturbated throughout. Burrows appear as color mottling and as distinct traces. *Zoophycos* and *Chondrites* burrows are mostly present in the lower part of the cycles, whereas *Thallasinoides* traces are in the uppermost part. Other traces are *Planolites* and *Terrebelina,* specifically at the top of a slump body in interval 182-1126C-10X-1, 90–94 cm. Some of the burrows in Subunit IIB are pyritized (e.g., Section 182-1126B-10H-5, 60 cm).

One distinctive postdepositional feature of the sediment is a series of planar color laminations as thick as 1.5 cm. Laminae have a greenish to dark gray or black color and were probably formed by reduction of ferruginous particles in the sediment. Analyses of smear slides and of the fraction >63 µm show that no sediment compositional changes occur in these layers.

Unit III

Intervals: Sections 182-1126B-14H-5, 125 cm, through 21X-CC; Sections 182-1126C-13X-5, 82 cm, through 17X-CC; Cores 182-1126D-1R through 2R
Depth: 116.75–165.50 mbsf (Hole 1126B); 116.32–154.00 (Hole 1126C); 150.00–175.10 (Hole 1126D)
Age: middle Miocene

Deposits of Unit III consist of poorly differentiated matrix-supported calcareous oozes with interbedded silicified layers. The matrix of the oozes is dominated by calcareous nannofossils. It also contains abundant sponge spicules and organic debris. The >63-µm fraction consists of abundant sponge spicules and common bioclastic debris, as well as small planktonic and benthic foraminifers. Glauconite occurs as infill of the planktonic foraminifers and as isolated grains. No macrofossils were recorded in the deposits of Unit III.

As in the overlying units, the succession consists of an alternation of lighter and darker intervals. Textural differences between both sediment types in Unit III, however, are minor. Both have a mudstone to wackestone texture with darker intervals containing slightly more sponge spicules and bioclasts. Changes between both lithologies are gradational.

The sediments are moderately to strongly bioturbated throughout. Burrowing appears as color mottling but in some cases also occurs as well-defined traces, such as *Chondrites* burrows in Section 182-1126C-17X-1 or as burrows with backfills (probably *Zoophycos*) in interval 182-1126B-19H-4, 60–75 cm. As in the deposits of the overlying unit, postdepositional features are represented by green and black laminae as thick as 1.5 cm.

Unit IV

Intervals: Core 182-1126B-22X through Section 32X-CC; Core 182-1126D-3R through Section 27R-1, 33 cm
Depth: 165.50–263.30 (Hole 1126B); 175.10–396.61 (Hole 1126D)
Age: middle Eocene–early Miocene

Four lithologies were recovered in this interval: (1) poorly differentiated nannofossil chalk, (2) poorly differentiated spiculitic nannofossil ooze, (3) silicified calcareous pelagic limestone, and (4) porcellanite and chert.

The nannofossil chalk, nannofossil ooze, and the spiculitic nannofossil ooze are whitish to light gray in color. Throughout the unit, they are matrix supported with calcareous nannofossils dominating. Components >63 µm are rare and consist of sponge spicules, with minor small planktonic foraminifers, and bioclasts.

The chalks and oozes are pervasively bioturbated throughout. Burrows appear as mottles and as well-defined traces. This is especially the case in Cores 182-1126C-24R, 25R, and 26R where frequent *Zoophycos* and *Chondrites* traces are present. As in the deposits of the overlying units, postdepositional green and black laminae occur in these sediments.

Silicified pelagic limestone is light gray to green in color. Thin-section analysis shows that the abundance of planktonic foraminifers and of sponge spicules varies between the samples (See **"Site 1126 Smear Slides,"** p. 80).

The porcellanite and chert have a greenish gray color. In some cases they form large nodules as large as 5 cm in diameter, but in other cases silicification may also occur as stratiform features affecting entire layers. Porcellanite and chert pieces contain large (as much as 1.5 cm), round vugs filled in with ooze and chalk. These vugs probably represent burrows that were not affected by silicification. Some of the calcareous nannofossil assemblages used to date the sediments of Unit IV come from these vugs (see **"Biostratigraphy,"** p. 12).

One layer of a minor lithology is present at the top of Unit IV (Sample 182-1126D-3R-CC, 12–15 cm). It contains bioclastic packstones with frequent planktonic and benthic foraminifers, frequent ostracodes, and echinoderm debris. Nonbiogenic components are angular quartz, glauconite, and mica.

Unit V

Interval: Sections 182-1126D-27R-CC through 33R-CC
Depth: 396.61–455.91 mbsf (bottom of the hole)
Age: Cretaceous (Cenomanian)

The upper boundary of this unit is defined by the contact between the overlying chalk and underlying siliciclastics in Core 27R. The lower boundary was not drilled at this site.

Subunit VA

Interval: Section 182-1126D-27R-CC, 0–25 cm
Depth: 396.61–405.89 mbsf
Age: middle? Eocene or older

Subunit VA is a medium brown sandstone, locally cross-laminated, with a lower thin yellowish brown sandstone to claystone. An irregular cavity in the sandstone is centimeter sized and has a thin, laminated iron oxide lining. The cavity is filled with a yellow to brown calcareous sandstone. Terrigenous sand grains have a conspicuous limonitic coating. Carbonate is fine grained. Grains are possibly bioclasts such as minor gastropods. Small open vugs in the calcareous sandstone are lined with blocky calcite crystals.

Subunit VB

Interval: Core 182-1126D-28R through Section 33R-CC
Depth: 405.90–455.91 mbsf
Age: Cretaceous

Sediments consist of alternating black to green siltstone, sandstone, and microconglomerate. Samples analyzed by X-ray diffraction indicate spheroidal limonite, hornblende, feldspar, garnets, and cordierite, as well as accessory muscovite and tourmaline. Grains are angular to subangular.

Fining-upward cycles occur in different cores (e.g., Sections 28R-1 and 33R-1). Cycles have planar, low-angle planar, and low-angle trough cross-bedding in the lower part (sandstones to microconglomerates). Upper parts consist of silty sandstone, mudstone, and claystone with subplanar laminations. Bioturbation is absent to moderate throughout and comprises indeterminate burrows, especially in the fine-grained intervals.

Thin-section analysis (see **"Site 1126 Thin Sections,"** p. 82, for position of the samples) indicates that the coarse fraction of the sandstone is dominated by lithic grains with an oolitic coating of iron-rich clays. Quartz is common in the fine sand to silt-sized fraction, and medium-sized lobate pelloidal glaucony grains are abundant in some laminae. Some quartz grains show vesicles suggesting volcanic origin. Only very few biogenic grains are present (e.g., a small fragment of silicified wood in Sample 182-1126D-28R-3, 12–14 cm).

Discussion

The occurrence of bioturbation in the deposits of Unit VB may indicate that they formed in a marine setting. However, no other positive evidence for a marine origin of these sediments could be found. The oldest marine deposits drilled in the borehole Jerboa-1 are Albian in age

(Bein and Taylor, 1981). Thus, it seems reasonable to propose a post-Albian age for the siliciclastics at Site 1126. An interpretation of the siliciclastic depositional system is not straightforward. The sedimentary structures and textural changes allow for two interpretations. The deposits could be either part of a storm-dominated tempestite depositional system or could belong to a deeper water turbidite depositional system.

The nature of the unconformity between the Mesozoic and the Cenozoic sequences could not be observed at Site 1126 because of the low core recovery in the corresponding interval. The sequence boundary could correspond to the alteration affecting the siliciclastics in Subunit VA. Coated cavities in the sandstone would thus represent some kind of exposure surface with an irregular infill of younger, Eocene? calcareous sandstone. These sediments can possibly be attributed to seismic Sequence 7 (see **"Seismic Stratigraphy,"** p. 39). Overlying sediments of Units IV and III, which roughly correspond to the depositional phase B of the western Great Australian Bight (Feary and James, 1998, reprinted as **Chap. 2**), record a marine pelagic setting. The sedimentary succession at Site 1126 does not show any major changes throughout these units, with the exception of minor fluctuations of sponge spicule abundance and the presence of chert layers (Fig. **F3**). The late early Miocene–early middle Miocene warming of the surface waters observed in the onshore sedimentary succession (Feary and James, 1998, reprinted as **Chap. 2**) could not be identified in the sedimentary succession at Site 1126.

An interruption of the monotonous pelagic sedimentation is reflected by the slumps of Unit II. It is unresolved whether Unit II consists of one major slump or a sequence of different slumps. We favor the interpretation of several episodes of slumping because of the presence of relatively thick undisturbed sedimentary intervals between individual soft-sediment deformed units.

Relatively monotonous pelagic sedimentation at Site 1126 began again during the Pliocene (Unit I). The succession consists of an alternation between layers rich in planktonic foraminifers and layers dominated by calcareous nannofossils. The layers with more planktonic foraminifers have a higher glauconite content, which correlates with peaks in the natural gamma-ray record. The benthic foraminiferal assemblages in these layers (see **"Biostratigraphy,"** p. 12) do not show any evidence of reworking. Thus, the alternation may reflect (1) changes in paleoceanography (i.e., productivity) or (2) changes in the bottom current regime leading to phases of mud winnowing. Additional postcruise investigations are required to address this question.

The results of downhole logging (see **"Downhole Measurements,"** p. 35) permitted pinpointing of the depths of the seismic reflections (Feary and James, 1998, reprinted as **Chap. 2**) (see **"Seismic Stratigraphy,"** p. 39) and comparison of these data with lithostratigraphic information. There is a relatively good coincidence between the depth of the reflection at the base of Sequence 3 and the position of the boundary between Units IV and III. The reflection at the top of Sequence 6A could not be recognized as a major sedimentary break, although a firmground occurs at a similar depth in Core 182-1126D-9R (Fig. **F3**).

The boundaries between Unit III and Subunit IIB, Subunits IIB and IIA, and Subunit IIA and Unit I show only a poor correlation with sequence-bounding reflections. This discrepancy may arise in part from the fact that the slump deposits are laterally discontinuous and that the seismic facies of these units are in part chaotic (see **"Seismic Stratigra-**

phy," p. 39). Finally, there is a reasonably good correlation between the position of the seismic reflection at the base of Sequence 2 and the boundary between Subunits IA and IB.

BIOSTRATIGRAPHY

Introduction

Core recovery was good throughout Hole 1126C (~90% recovery) and most of Hole 1126B (86% to 160 mbsf), although the continuity of the stratigraphic record was marred by poor core recovery below 160 mbsf in both Holes 1126B (18% recovery below 160 mbsf) and 1126D (13% recovery; the cored interval is mostly below 160 mbsf). Calcareous nannofossils and planktonic foraminifers are generally common to abundant with moderate to good preservation throughout Holes 1126A, 1126B, and 1126C, although preservation deteriorated and abundance declined in conjunction with poor core recovery in Hole 1126D. Benthic foraminifers are few to common with mostly good to moderate preservation in Holes 1126A and 1126B, although their numbers also declined and preservation became poorer downsection, especially in Hole 1126D. Benthic foraminifers, overall, are far less abundant than planktonic foraminifers in all holes.

Sediments recovered from Site 1126 range in age from Quaternary to middle Eocene, with most calcareous nannofossil zones represented except in four intervals, where missing nannofossil zones suggest disconformities. The suspected disconformities lie in the uppermost Pliocene (missing Zones NN18–NN17 at ~57 mbsf), lower Pliocene (missing Zones NN15–NN13 at ~67 mbsf), the upper Miocene (missing Zone NN11 at ~82 mbsf), and the middle Miocene (missing Zones NN9–NN6 at ~118 mbsf). Planktonic foraminifer zones are also missing from the disconformities at ~82 and ~118 mbsf. The foraminifers, however, do not verify the suspected disconformities at ~57 and ~67 mbsf, in part because the low diversity of the temperate planktonic foraminifer assemblages hampered biostratigraphic resolution. Placement of the Miocene/Pliocene boundary is inconsistent between the two data sets. The calcareous nannofossil data suggest that the Miocene/Pliocene boundary is at ~67 mbsf, whereas the planktonic foraminifer data suggest that the boundary lies within the disconformity at ~82 mbsf.

Four main assemblages of benthic foraminifers are identified at Site 1126. The Quaternary to upper Eocene assemblages indicate upper to middle bathyal paleodepths. The middle to upper Eocene assemblage suggests lower to middle bathyal paleodepths and well-oxygenated conditions at the seafloor. A similar assemblage was reported from the early Eocene at Site 747 on the Kerguelen Plateau (Mackensen and Berggren, 1992).

Sedimentation rates are comparatively fast in the Quaternary (31 m/m.y.) and slow in the remainder of the Neogene and Paleogene sections, where rates alternate between 3–8 m/m.y. in the upper Pliocene, the lower Pliocene–upper middle Miocene, the lower Miocene–upper Oligocene, and the lower Oligocene–upper Eocene, and 11–16 m/m.y. in the intervening sections. One interval of nondeposition is indicated in the middle Eocene.

Calcareous Nannofossils

A middle Eocene–upper Pleistocene succession of calcareous nannofossil assemblages showing four possible hiatuses is identified at Site 1126. Several of these hiatuses correspond closely with a sequence stratigraphic boundary (see "Seismic Stratigraphy," p. 39). In spite of generally poor core recovery in the lower Miocene, Oligocene, and Eocene, most zones are represented (Fig. F6).

F6. Calcareous nannofossil and planktonic foraminifer zones with benthic foraminifer assemblages, p. 52.

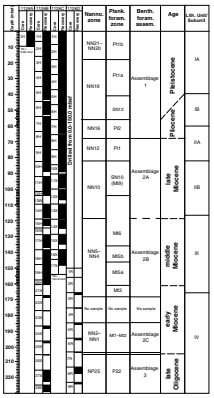

Pleistocene

Assemblages of the combined Zones NN21–NN20, including *Braarudosphaera bigelowii, Emiliania*? *huxleyi, Gephyrocapsa caribbeanica, Gephyrocapsa oceanica,* small *Gephyrocapsa* spp. (including *G. aperta*), and *Helicosphaera hyalina* are identified in Samples 182-1126B-1H-CC (6.51 mbsf) and 2H-CC (15.63 mbsf). Common *Pseudoemiliania lacunosa* and abundant small *Gephyrocapsa* spp. in Sample 182-1126C-2H-CC (17.99 mbsf) indicate Zone NN19. This zone is recognizable down to Sample 182-1126C-6H-CC (56.02 mbsf). *Reticulofenestra asanoi* appears in the middle of Zone NN19 in Sample 182-1126C-4H-CC (37.23 mbsf). Both *Calcidiscus macintyrei* and *Helicosphaera sellii* have their highest occurrences in the lower part of the zone in Sample 182-1126B-6H-CC. Minor reworking from a Paleogene source was found in the lower part of Zone NN19, as shown by the occurrence of *Dictyococcites bisectus* in Sample 182-1126B-6H-CC. *Braarudosphaera bigelowii* and *Pontosphaera japonica* are recorded in Zone NN19 (e.g., in Sample 182-1126B-3H-CC).

Pliocene

Only one Pliocene calcareous nannofossil zone, Zone NN16 of late Pliocene age, is recognized in Holes 1126B and 1126C. The assemblage assignable to this zone is recorded from Samples 182-1126B-7H-CC (63.9 mbsf), 182-1126C-7H-CC (64.96 mbsf), and 182-1126B-8H-3, 32–34 cm (66.82 mbsf). Being heavily calcified, the discoasters in these samples are poorly preserved, although the remainder of the nannofossils are generally moderately to well preserved. The assemblage contains *Discoaster brouweri, D. surculus, Calcidiscus leptoporus, C. macintyrei, Coccolithus pelagicus, C. radiatus, Reticulofenestra minuta, Reticulofenestra minutula,* and *Syracosphaera* spp. Whether the two short Zones NN18 and NN17 of the later Pliocene are represented above the core catcher in either or both Cores 182-1126B-7H and 182-1126C-7H was not determined in our shipboard study.

Miocene

Miocene nannofossil assemblages identified in Holes 1126B and 1126C represent a discontinuous succession of zones (Fig. F6). A distinct lithologic boundary in Section 182-1126B-8H-3 (between 66.51 and 66.82 mbsf) separates upper Pliocene from upper Miocene assemblages. The younger assemblage of Zone NN16 identified from Sample 182-1126B-8H-3, 1–3 cm (66.51 mbsf), is immediately followed downhole by an older assemblage in Sample 182-1126B-8H-3, 32–34 cm (66.82 mbsf). The latter includes *Amaurolithus ninae, A. primus, C. leptoporus, C. pelagicus, Dictyococcites antarcticus, Discoaster pentaradiatus, D. variabilis, Helicosphaera carteri, Reticulofenestra pseudoumbilicus, Reticulofenestra minuta, R. minutula, Sphenolithus neoabies, Syracosphaera* spp.,

and *Triquetrorhabdus rugosus*, indicating lower Zone NN12 (Subzone CN10a) of latest Miocene age. A similar assemblage, also indicating lower Zone NN12, is recorded from Sample 182-1126C-8H-CC (75.76 mbsf). The missing Zones NN13 and NN15 collectively spanned >1 m.y.

Another disconformity is tentatively identified to coincide with a firmground in Section 182-1126C-9H-5 at 85 cm (see **"Lithostratigraphy,"** p. 4). Calcareous nannofossils from above and below this firmground suggest a hiatus; the long late Miocene Zone NN11 is apparently missing. Below the firmground the assemblage in Sample 182-1126C-9H-5, 120–125 cm (82.20 mbsf), contains *Minylitha convallis* and *Discoaster neohamatus*, which, in the absence of *Discoaster quinqueramus*, suggests Zone NN10 of early late Miocene age. This zone is also detected in the assemblage from Sample 182-1126B-9H-CC (82.02 mbsf), which also contains reworked components (*Cyclicargolithus floridanus, Helicosphaera euphratis*, and *Discoaster deflandrei* "group") from the Paleogene. Assemblages from below the firmground down to Sample 182-1126C-12X-CC (106.96 mbsf) show more pronounced evidence of reworking compared with overlying assemblages, as demonstrated by the occurrence of the Eocene *Neococcolithes dubius* in Sample 182-1126C-9H-CC and the Paleogene *D. bisectus* in Sample 182-1126C-10X-CC.

A disconformity close to the lower boundary of lithostratigraphic Subunit IIB (~116 mbsf) (see **"Lithostratigraphy,"** p. 4) likely is indicated by Zones NN9–NN6 being condensed or missing. The assemblages in Samples 182-1126C-13X-CC through 17X-CC (118.94–148.81 mbsf) are readily assignable to the combined Zones NN5–NN4 on the basis of the consistent presence of the key species *Sphenolithus heteromorphus*. In contrast to the assemblages from the interval above, the assemblages of the combined Zones NN5–NN4 do not contain any significant reworked component. In addition to *S. heteromorphus*, the latter assemblages include *C. leptoporus, Coccolithus miopelagicus, Coronocyclus nitescens, C. floridanus, D. deflandrei, Discoaster trinidadensis, H. carteri, H. euphratis, Helicosphaera obliqua, R. pseudoumbilicus*, and *Sphenolithus abies*. The hemipelagic taxa *B. bigelowii, Micrantholithus pinguis*, and *Pontosphaera multipora* are sporadic in their occurrence, whereas *Calcidiscus premacintyrei* occurs consistently down to Sample 182-1126B-19H-CC (157.08 mbsf). *Helicosphaera ampliaperta*, the key species separating Zone NN4 from Zone NN5, is not known to occur in lower Miocene sediments either on the southern margin of Australia (S. Shafik, unpubl. data) or from the Southern Ocean south of Australia. Proxies to the last occurrence (LO) of *H. ampliaperta*, such as the first occurrence (FO) of *Discoaster signus* and the end of acme of *D. deflandrei*, cannot be applied. *Discoaster signus* is absent, and the abundance of *D. deflandrei* cannot be satisfactorily determined because of the persistent diluting effect of silicoflagellate debris.

Core recovery in the remainder of the lower Miocene was very poor (see **"Operations,"** p. 2). Zone NN2 of early Miocene age is tentatively identified in Sample 182-1126D-5R-CC (185.52 mbsf) because of the presence of a few specimens of *Orthorhabus*? *serratus* among an assemblage that includes rare *Triquetrorhabdus auritus* and *Triquetrorhabdulus carinatus*, few *C. nitescens* and *Cyclicargolithus abisectus*, and abundant *B. bigelowii* and *C. floridanus*. Assemblages in Samples 182-1126B-24X-CC and 25X-CC (188.0–197.28 mbsf) are poorly preserved, although the taxa *B. bigelowii, C. abisectus, C. floridanus, D. deflandrei, H. euphratis, H. obliqua, Sphenolithus conicus*, and *T. carinatus* are identified. Neither *Discoaster druggii* nor *O. serratus* are found, and the abundance of *C. abisec-*

tus suggests a level above the acme of the species. This evidence is taken to indicate the upper part of Zone NN1 (Subzone CN1b) of early Miocene age. In Hole 1126D the poorly preserved assemblages in Samples 182-1126D-6R-CC and 7-CC (195.30–204.61 mbsf) are datable as early Miocene Zone NN1. The Oligocene/Miocene boundary is well constrained at Site 1126 between Samples 182-1126D-7R-CC and 182-1126B-26X-CC (204.61–205.85 mbsf).

Oligocene

Assemblages readily assignable to Zone NP25 of late Oligocene age are recorded from Samples 182-1126B-26X-CC through 29X-CC. The moderately preserved assemblage near the top of the zone (Sample 182-1126B-26X-CC) contains a few specimens of *Sphenolithus delphix* but also includes abundant *D. bisectus* and common *T. carinatus*, a transitional form between *H. obliqua* and *Helicosphaera recta*, together with typical *H. recta*. A diverse assemblage in Sample 182-1126B-27-CC includes the key species *Sphenolithus ciperoensis*, together with *B. bigelowii, Chiasmolithus altus, C. abisectus, C. floridanus, D. bisectus, H. euphratis, H. obliqua, H. recta, Micrantholithus flos, Micrantholithus* sp. cf. *M. procerus, Reticulofenestra lockeri, S. conicus, Sphenolithus dissimilis*, and *Zygrhablithus bijugatus*.

Hole 1126B bottomed in Zone NP24 of late Oligocene age. This age is based on a few specimens of *Sphenolithus distentus* in association with *S. ciperoensis* in Sample 182-1126B-32X-CC. *Sphenolithus distentus* is absent from the samples examined from Hole 1126D, and only atypical forms of this species are observed in Samples 182-1126D-15R-CC and 17R-CC, in association with *Sphenolithus predistentus*. The assemblage in Sample 182-1126D-15R-CC (281.19 mbsf) is assigned tentatively to the combined zones NP24 and NP23 because of the common presence of *C. abisectus*. The assemblage in Sample 182-1126D-17R-CC is regarded as upper Zone NP23 (Zone CP18), in the absence of *C. abisectus* and the presence of *Sphenolithus* sp. aff. *S. distentus*. Other species found in Sample 182-1126D-17-CC include *B. bigelowii, Chiasmolithus altus, D. bisectus, R. lockeri,* and *Z. bijugatus*. These, in addition to *C. miopelagicus, M. flos,* and *M. pinguis,* occur in Sample 182-1126D-15R-CC. The assemblage recovered from Sample 182-1126D-18R-CC (309.9 mbsf) is readily assignable to the lower part of Zone NP23 (Zone CP17), including *Chiasmolithus altus, D. bisectus, Discoaster nodifer, R. lockeri, S. predistentus,* and *Z. bijugatus,* and lacking both *Sphenolithus* sp. aff. *S. distentus* and *Reticulofenestra umbilicus*. Zones NP22 and NP21 were recognized in Samples 182-1126D-19R-CC (319.41 mbsf) and 20R-CC (329.89 mbsf), respectively. *Coccolithus formosus, Isthmolithus recurvus,* and *R. umbilicus* are recorded in 182-1126D-20R-CC, and *R. umbilicus,* without the other two species, was identified in 19R-CC.

Abundant *Chiasmolithus altus* occurs throughout the Oligocene sequence, indicating a cool-water regime, although the presence of *S. ciperoensis* in the upper part suggests a warm-water influence. The cool-water aspect is supported by macrofaunas and lithologic textures found in sediments of the same age (the Abrakurrie Limestone) on shore (James and Bone, 1991). Shafik (1990) documented nannofossil assemblages from the Great Australian Bight indicative of a cool-water regime, but with an intermittent warm-water influence during the middle and late Oligocene attributed to a surface current intermittently bringing warm water from the Indian Ocean. The consistent occurrence of *B.*

bigelowii and *Z. bijugatus* throughout the Oligocene sequence suggests shallow-water deposition.

Eocene

The Eocene/Oligocene boundary lies between Samples 182-1126D-20R-CC and 21R-CC. A sample from the latter (at 338.87 mbsf) recovered a moderately preserved assemblage readily assignable to the upper part of combined Zones NP19–NP20 of late Eocene age based on the presence of *Chiasmolithus oamaruensis, C. formosus, D. bisectus, D. nodifer, Discoaster saipanensis, Helicosphaera compacta, Reticulofenestra hampdenensis, R. umbilicus,* and *Z. bijugatus*. Samples 182-1126D-22R-CC and 23R-CC (351.45–370.11 mbsf) contain assemblages, also moderately preserved, which are assigned to Zone NP18. These include the key taxa *C. oamaruensis, Cribrocentrum reticulatum, D. bisectus, D. nodifer,* and *D. saipanensis,* as well as the holococcolith *Lanternithus minutus*.

Middle Eocene nannofossil assemblages (Zones NP17 and NP16) were recovered from Sample 182-1126D-24R-CC through 27-CC (370.1–396.63 mbsf). Assemblages assignable to Zone NP16 occur in Samples 182-1126D-25R-CC through 27-CC (380.38–396.63 mbsf). These are characterized by common *Chiasmolithus grandis, Chiasmolithus solitus, C. reticulatum, D. nodifer,* and *D. saipanensis*. Chiasmoliths are markedly more abundant than discoasters, indicating a cool-water regime, although subtle evidence for warm-water influence in the lower cores is detected: *S. predistentus* in Sample 182-1126D-26R-CC (390.38 mbsf), and *Helicosphaera dinesenii* and *H. reticulata* in Sample 182-1126D-27R-CC (396.63 mbsf). Samples from Cores 182-1126D-28R (409.75 mbsf) down to 32R (total depth at 444.35 mbsf) lack any calcareous microfossils.

Shafik (1990, and references therein) suggested the existence of warm-water masses during the mid-middle Eocene in the region, attributed to a proto-Leeuwin Current. The current's influence along the Australian southern margin was strong in the western Great Australian Bight and diminished in an easterly direction. Middle Eocene assemblages from the eastern part of the Great Australian Bight (immediately to the west of Kangaroo Island), coeval with those in Samples 182-1126D-26R-CC and 27-CC, contain *S. predistentus, H. dinesenii,* and *H. reticulata*. In contrast, middle Eocene assemblages from the western Otway Basin to the east lack these warm-water species (Shafik, 1983), suggesting no significant effect of the proto-Leeuwin Current (Shafik, 1990). Shallow-water deposition during most of the Eocene at Site 1126 is suggested by the occurrence of *L. minutus* and *Z. bijugatus*.

Planktonic Foraminifers

The quality of the foraminifers at Site 1126 was excellent overall. The preservation was ranked from very good to moderate throughout the Quaternary to Oligocene sections, and poor only in the Eocene section of Hole 1126D. Abundance was ranked from abundant to common throughout Holes 1126B, 1126C, and 1126D, and the single core from Hole 1126A. Eleven core-catcher samples recovered only pieces of chert and porcellanite when drilling difficulties washed away the soft and probably fossiliferous sediments. The basal sandstone of Hole 1126D (396.61–455.91 mbsf) was barren of foraminifers except for a few contaminated specimens in Sample 182-1126D-28R-CC, 15–17 cm (409.75 mbsf).

The Cenozoic subtropical and temperate zonations of Berggren et al. (1995a, 1995b) were partly applicable to the fossil succession at Site 1126 in the Pleistocene, Pliocene, and Miocene. We found that the zonal definitions of Jenkins (1993, 1985) best described two assemblages from the early Pleistocene–late Pliocene and late Miocene (Fig. F6). The Oligocene and Eocene successions were correlated to the standard "P" zones of Blow (1969) and Berggren and Miller (1988), on the basis of the species ranges of Toumarkine and Luterbacher (1985) and datum levels developed for the region as compiled in Chaproniere et al. (1995) and McGowran et al. (1997).

The foraminifer-bearing sections recovered most biostratigraphic zones within the Quaternary through the middle Eocene. Several zonal boundaries occur near seismic boundaries, and many indicate hiatuses (see "Seismic Stratigraphy," p. 39). The slumping in the interval between Cores 7H and 13X in Holes 1126B and 1126C (see "Lithostratigraphy," p. 4) mixed lower Pliocene and upper Miocene sediments to various degrees. In this interval Zone Pl1 rests on Zone Mt9 at ~82 mbsf, with an apparent loss of ~3 m.y. Zone Mt9 rests on Zone Mt6, indicating a loss of ~4 m.y. at ~118 mbsf. Several zones were not positively identified from the middle and lower Miocene at Holes 1126B and 1126C, indicating either disconformities or insufficient sampling.

Quaternary

The planktonic foraminifer assemblage is dominated by *Globorotalia inflata* and *Globigerinoides ruber* (principally the white form), with lesser amounts of *Globigerina bulloides, Globigerina quinqueloba, Globigerina falconensis, Orbulina universa,* dextral *Neogloboquadrina pachyderma,* and *Globigerinita glutinata*. There are traces of warmer water taxa, such as *Globigerinoides sacculifer, Neogloboquadrina dutertrei,* and *Pulleniatina obliquiloculata*.

The subtropical zonation of Berggren et al. (1995b) was applied in part to the Quaternary succession. *Globorotalia truncatulinoides* persisted throughout the interval, and *Globorotalia tosaensis* made its last appearance at 15.63 mbsf (182-1126B-2H-CC, 17–22 cm) and 27.28 mbsf (182-1126C-3H-CC, 13–15 cm), dividing the Quaternary zone into Pt1a and Pt1b (Fig. F6). *Globorotalia hirsuta* makes its first appearance in Subzone Pt1b (Berggren et al., 1995a) in Sample 182-1126B-1H-CC, 11–16 cm (6.51 mbsf). The base of the zone as defined by Berggren et al. (1995b) could not be applied because *Globigerinoides fistulosus* and *Globigerinoides extremus* were not observed. We placed the base of Pt1 at the first appearance of *G. truncatulinoides,* following the definition of Jenkins (1993) and Chaproniere et al. (1995).

A distinctly cool temperate assemblage underlies the interval assigned to Pt1 and includes dextral *N. pachyderma, Globigerina bulloides, G. falconensis, G. ruber, Globorotalia inflata, Globorotalia crassaformis, Globorotalia crassula,* and *G. tosaensis*. The assemblage fits the definition of Zone SN13, the *Globorotalia inflata* Zone of Jenkins (1985, 1993), because it contains abundant *Globorotalia inflata* without *G. truncatulinoides*. On the basis of correlation to the calcareous nannofossil zones, we suspect that this zone includes part of the early Pleistocene and may extend into the late Pliocene, although this remains unconfirmed.

Upper Miocene–Lower Pliocene

The differentiation of upper Miocene from lower Pliocene sections is complicated at Site 1126 by the slumps and debris flows throughout lithostratigraphic Unit II between Core 182-1126B-7H and Section 182-1126B-14H-5 and between Core 182-1126C-7H and Section 182-1126C-13X-5 (Fig. F6). The sedimentary disturbance mixed together various proportions of Miocene and lower Pliocene taxa. In general, samples from Cores 182-1126B-7H to 9H and Cores 182-1126C-7H to 9H are dominated by lower Pliocene taxa with minor occurrences of Miocene taxa, whereas samples from Cores 182-1126B-10H to 14H and 182-1126C-10H to 13H are dominated by upper Miocene taxa with some middle Miocene elements.

The lower Pliocene assemblage from Cores 182-1126B-7H to 9H and 182-1126C-7H to 8H is warm temperate to subtropical and includes such warm-water elements as *Globorotalia tumida, Globorotalia plesiotumida, Globorotalia exilis,* and *Globorotalia menardii* with *Sphaeroidinella seminulina* s.l., *Globigerinoides quadrilobatus,* and *Globigerinoides trilobus*. Important lower Pliocene zone markers and/or datum levels fall in this interval, such as the last appearance of *Zeaglobigerina nepenthes* in Samples 182-1126B-9H-CC, 15–18 cm, and 182-1126C-8H-CC, 43–46 cm, indicating the top of Pl1, and the last appearance of *Globorotalia margaritae* in Samples 182-1126B-7H-CC, 12–15 cm, and 182-1126C-6H-CC, 26–29 cm, indicating the top of Pl2. Although Zones Pl1 and Pl2 were referred to this interval, the disjunct range of many species reflects disturbance caused by slumping in lithostratigraphic Unit II (see "Lithostratigraphy," p. 4); hence, the zonal assignments are tentative.

Other species that make their last appearances in the temperate late Miocene are *Globoconella conoidea* and *Globoconella miozea,* which last occur in Sample 182-1126B-9H-CC and Section 182-1126C-9H-5, and several menardine taxa, including *G. menardii* (Samples 182-1126B-8H-CC to 10H-CC and 182-1126C-10X-CC) and *Globorotalia* cf. *praemenardii* (Sections 182-1126B-11H, 12H, and 182-1126C-9H-5). This interval is placed in Zone Mt9 or SN10.

The position of the Miocene/Pliocene boundary was tentatively placed between Cores 182-1126B-8H and 9H and 182-1126C-8H and 9H, and occurs within a disconformity. The range of the upper Miocene species *Globoquadrina dehiscens* is truncated at the disconformity, and distinctly Pliocene taxa overlie the contact (Samples 182-1126C-8H-CC, 43–46 cm, and 182-1126B-8H-CC, 13–16 cm). The Pliocene taxa include *Globoconella sphericomiozea, G. tumida, G. crassaformis,* and *Globorotalia pliozea,* all of which make their first appearances near the base of the Pliocene in Zone Pl1. The Miocene taxa include *Globoconella miozea, G. dehiscens,* and *Globoconella conoidea,* which occur together in lower Zone Mt9. A hiatus of at least 1.3 m.y. is indicated between the last appearance of *G. dehiscens* (last appearance datum is 5.8 m.y.) and the first appearance of *G. crassaformis* (first appearance datum is 4.5 m.y.). This hiatus is probably more than 2.6 m.y. (between the top of Mt9 at 7.12 Ma and the first appearance of *G. crassaformis,* which is 4.5 Ma). The contact of Pl1 on Mt9 suggests that the Miocene/Pliocene boundary lies within the disconformity at ~82 mbsf. Calcareous nannofossils, however, indicate that the Miocene/Pliocene boundary lies at the contact between Zones NN16 and NN12 at ~68 mbsf (see "Calcareous Nannofossils," p. 13). Postcruise study is needed to resolve the discrepancy.

Middle Miocene

The first undisturbed sediments below the slumped interval (116.75 mbsf at Hole 1126B and 116.32 mbsf at Hole 1126C) are early middle Miocene in age in Zone Mt6, indicating a hiatus of ~4 m.y. in the later middle Miocene (Fig. F6). The middle Miocene assemblage includes *Globigerinoides sicanus, Orbulina suturalis, Praeorbulina glomerosa,* and *Fohsella peripheroronda,* in addition to significant percentages of several long-ranging Neogene species such as *G. quadrilobatus, G. triloba, G. dehiscens,* and *G. quinqueloba*. Temperate Zone Mt6 was delineated from Samples 182-1126B-14H-CC, 12–15 cm; 15H-CC, 0–4 cm; and 182-1126C-12X-CC to 15X-CC. Zone Mt5 was recognized in Samples 182-1126B-17H-CC; 18H-CC; 19H-CC, 23–26 cm; 20H-CC, 6–9 cm; 182-1126C-16H-CC, 10–12 cm; and 182-1126C-17X-CC, 25–27 cm.

Lower Miocene

The lower Miocene assemblage is characterized by *Catapsydrax dissimilis, Catapsydrax unicavus, Globoconella incognita, Jenkinsella semivera, Jenkinsella bella, Zeaglobigerina brazieri, Zeaglobigerina woodi,* and *Zeaglobigerina connecta*. Zone Mt4, which spans only 300,000 yr, was absent from the site, probably because of inadequate sampling. Zone Mt3 was delineated from Samples 182-1126B-21X-CC, 18–20 cm (160.48 mbsf); 22X-CC, 17–20 cm (168.35 mbsf); and 182-1126D-3R-CC, 4–6 cm (166.69 mbsf). Zone Mt2 was recognized in Samples 182-1126B-24X-CC, 23–26 cm (188 mbsf); and 25X-CC, 15–18 cm (197.28 mbsf).

Oligocene

Sample 182-1126B-26X-CC, 15–18 cm (205.85 mbsf), contains, among other Oligocene/Miocene species, typical specimens of *Globigerinoides primordius* that indicate the latest Oligocene. This further suggests that the Miocene/Oligocene boundary lies between 197.28 and 205.85 mbsf.

Overall, the Oligocene section at Site 1126 is poorly represented because of poor core recovery. At Hole 1126D Oligocene sediment was recovered in the core catchers of Cores 182-1126D-8R, 12R, 16R, and 20R at 217.69, 252.68, 290.98, and 329.89 mbsf, respectively. The intervening cores contain only chert coated by thin rinds of sediment suitable only for nannofossil analysis. Core recovery was also poor at Hole 1126B, averaging 18% below 160 mbsf. However, a core-catcher sample from every core was successfully prepared for foraminifers. The Oligocene foraminifers included *C. dissimilis, Chiloguembelina cubensis, Dentoglobigerina galavisi, Globigerina ciperoensis, Globigerina euapertura, Globigerina officinalis, Globigerina ouachitaensis, Globigerina praebulloides, Globigerinita juvenilis, Paragloborotalia opima nana, Globoquadrina venezuelana, G. suteri, Globorotaloides testarugosus,* and *Zeaglobigerina labiacrassata*. Zone P22, equivalent to SP15 of Jenkins (1993) and containing most of these species except *C. cubensis* and *Z. labiacrassata,* occurs from Cores 182-1126B-27X to 31X and in Samples 182-1126D-8R-CC, 21–23 cm; and 12R-CC, 18–20 cm. In Sample 182-1126B-32X-CC, 26–28 cm, *P. opima nana* and *Paragloborotalia opima opima* indicate Zone P21 (Subzone P21b) according to Berggren et al. (1995b). Sample 182-1126D-16R-CC, 38–39 cm, contains abundant small specimens, particularly those of *C. cubensis* and tenuitellid forms. In the absence of *Pseudohastigerina,* the association of these forms with *Z. labiacrassata* in-

dicates an early Oligocene age equivalent to Zone P19 (Berggren et al., 1995b; McGowran et al., 1997) (Fig. F6).

Eocene

Upper and middle Eocene sediments were recovered from Hole 1126D, although core recovery was low (~13%). The upper Eocene assemblage, which occurs in samples from 334.38 ± 4.49 mbsf to 360.78 ± 9.33 mbsf, consisted of *C. cubensis, Globigerina cryptomphala, Globigerinatheka index, Globoconella nana, Globorotaloides suteri, Globorotaloides testarugosa, Pseudohastigerina micra, Subbotina angiporoides, Subbotina eocaena, Subbotina lineaperta,* and *Turborotalia increbescens*. Lacking typical middle Eocene taxa such as *Acarinina,* the association was correlated to Zone P16 in Samples 182-1126D-21R-CC, 18–19 cm (338.87 mbsf), and 22R-CC, 15–17 cm (351.45 mbsf). The middle Eocene association is comprised of *Acarinina aculeata, Acarinina bullbrooki, Acarinina collactea, Acarinina primitiva, Acarinina spinuloinflata, C. cubensis, G. index, Globigerinatheka subconglobata luterbacheri, P. micra, S. angiporoides, Subbotina linaperta,* and *Turborotalia cerroazulensis*. On the basis of the successive last appearances of *A. collactea, Acarinina primitiva,* and *A. bullbrooki* (Table T1), Samples 182-1126D-24R-CC, 30–33 cm (370.11 mbsf), and 25R-CC, 15–17 cm (380.38 mbsf), were assigned to P15; Sample 182-1126D-26R-CC, 23–25 cm (390.38 mbsf), was assigned to Zone P14; and Sample 182-1126D-27R-CC, 0–2 cm (396.63 mbsf), was assigned to Zone P12.

Benthic Foraminifers

Benthic foraminifers were studied in all core-catcher samples from Holes 1126B and 1126D, except in Cores 182-1126B-13H and 16W, 182-1126D-13R through 15R, and 182-1126D-17R through 19R, which recovered only hard chert fragments. Additional samples from Hole 1126C were also analyzed (Samples 182-1126C-9H-5, 45–50 cm, and 9H-5, 120–125 cm). Abundant chert layers were found during drilling between ~160 and 400 mbsf, leading to poor core recovery. Abundant sponge spicules and radiolarians in many samples from that interval indicate an extended episode of high biosiliceous sedimentation.

Benthic foraminifers are moderately abundant in core-catcher samples from Holes 1126B and 1126D, although they are rare in comparison with planktonic foraminifers. Benthic foraminifer abundance drops significantly in the carbonate rocks near the base of Hole 1126D in Cores 22R–27R. The lowermost cores from Hole 1126D (Cores 28R–33R) are barren, below the major lithologic change from light carbonate rocks into dark micaceous sandstones, siltstones, and mudstones. The absence of foraminifers and nannofossils from any of the core-catcher samples examined from this interval suggests that it probably represents an episode of nonmarine deposition.

Between 100 and 300 specimens were picked from the >63-µm fraction, except in samples where benthic foraminifer abundance was very low. Preservation is good to moderate, except in samples from Cores 182-1126B-12H through 18H that contain a significant proportion of abraded and corroded specimens, and in samples from Cores 182-1126B-24X through 25X and Cores 182-1126D-20R through 24R that contain mainly small, thin tests of benthic foraminifers, showing signs of partial dissolution. Relative abundances of species were determined in all samples (see "Benthic Foraminifers," p. 11, in the "Explanatory

Notes" chapter). The benthic foraminiferal assemblages studied include mainly calcareous taxa and only few species and specimens of agglutinated taxa. The benthic foraminifers generally represent well-known "deep-water" taxa, which have a well-documented cosmopolitan distribution (van Morkhoven et al., 1986; Miller and Katz, 1987; Thomas, 1990; Katz and Miller, 1991; Mackensen and Berggren, 1992; Mackensen, 1992). The following benthic foraminiferal assemblages are recognized in the Cenozoic succession of Holes 1126B, 1126C, and 1126D.

Assemblage 1 (Holocene–Late Early Pliocene)

Cores 182-1126B-1H through 7H

This is a well-diversified assemblage, characterized by the few or common occurrence of *Planulina wuellerstorfi, Uvigerina hispidicostata, Stilostomella lepidula, Bulimina aculeata, Cibicidoides* spp., and *Loxostomoides* spp. Also present are *Plectofrondicularia vaughni, Uvigerina proboscidea, Bigenerina nodosaria, Sigmoilopsis schlumbergeri, Laticarinina pauperata, Triloculina* spp., *Pleurostomella* spp., *Lenticulina* spp., and *Pullenia* spp. Middle bathyal paleodepths are indicated for this interval by the presence of *P. vaughni, L. pauperata,* and *P. wuellerstorfi,* generally found in water depths exceeding 500 m, and by the lack of deeper water indicators. Fluctuations in the relative abundance of some taxa such as *Cibicidoides* spp. and *Uvigerina* spp., observed in some of the samples, may reflect cyclic changes in surface-water productivity or circulation. However, the low time resolution of the present study does not permit the frequency of these changes to be resolved and clearly shows the need for high-resolution studies to elucidate benthic foraminiferal distribution patterns in relation to paleoceanography.

Assemblages 2A and 2B (Late Miocene–Early Miocene)

Cores 182-1126B-8H through 22X

Assemblages 2A and 2B are characterized by the few to common occurrence of *P. wuellerstorfi, U. proboscidea,* and *Rectuvigerina striata* (Assemblage 2A). From Core 182-1126B-14H downward, fluctuating abundances of *Patellina corrugata* are observed (Assemblage 2B). Also present within the assemblage are *Spirillina minima, Stilostomella modesta, Stilostomella* spp., *Cibicidoides mundulus, Sphaeroidina bulloides, Lagena sulcata, Uvigerina* spp., *Lenticulina* spp., *Cibicidoides* spp., *Siphonina tenuicarinata, B. aculeata, Globocassidulina subglobosa, Vulvulina spinosa, Hanzawaia mantaensis, S. schlumbergeri, Karreriella bradyi,* and *L. pauperata*. Sample 182-1126B-12H-CC contains some large, abraded, and corroded tests, which are indicative of reworking. The presence of *P. corrugata* and *Spirillina minima* in Cores 182-1126B-14H to 22X within a typically middle bathyal assemblage (as shown by the presence of *G. subglobosa, S. schlumbergeri, L. pauperata,* and *P. wuellerstorfi*) suggests that sediments from shallower depths were redeposited into deeper water. Below Core 182-1126B-18H *R. striata* becomes common or abundant in all samples. The changes observed in the relative composition of Assemblage 2B may be associated with global hydrographic or climatic changes in the early–middle Miocene (McGowran et al., 1997).

Assemblage 2C (Early Miocene)

Cores 182-1126B-24X through 25X

Assemblage 2C is a very impoverished assemblage dominated by small, thin, poorly preserved tests of *Bolivina* spp. Also present as minor constituents of the assemblage are *L. sulcata, Oridorsalis umbonatus, Astrononion pusillum, C. mundulus, Cibicidoides* spp., *S. tenuicarinata, L. pauperata, Stilostomella* spp., and various nodosariids. The assemblage includes species indicative of upper to middle bathyal paleodepths. However, the presence of *P. corrugata* and *Spirillina minima* and the dominance of small bolivinid tests within the assemblage indicate that the sediment may have been partly derived from the shallow shelf.

Assemblage 3 (Late Oligocene–Early Oligocene)

Cores 182-1126B-27X through 32X and Cores 182-1126D-8R through 16R-CC

This is a well-diversified, generally well-preserved assemblage that is characterized by the relatively common abundance of *O. umbonatus, Cibicidoides praemundulus, R. striata, V. spinosa, S. tenuicarinata, Stilostomella subspinosa, S. modesta, S. bulloides, Cibicidoides* spp., *Pullenia* spp., *G. subglobosa, V. spinosa, and Hanzawaia ammophila*. Also present in the assemblage are *K. bradyi, U. proboscidea, L. pauperata, Cibicidoides mexicanus, Cibicidoides micrus, Lenticulina* spp., *Bulimina* spp., *Bolivina* spp., *Uvigerina* spp., *Tritaxia* spp., *Anomalinoides semicribratus, L. sulcata,* and various nodosariids. The presence of *S. bulloides, S. tenuicarinata, R. striata, L. pauperata, V. spinosa,* and *U. proboscidea* in the assemblage indicate upper to middle bathyal paleodepths. This paleobathymetric interpretation is also supported by the absence of either shallower (neritic) or deeper water (lower bathyal to abyssal) indicators within Assemblage 3. Stratigraphically significant species within Assemblage 3 are *Cibicidoides mexicanus,* with a stratigraphic range from the upper Eocene (P16) to lower Miocene (N5), *C. micrus* with a LO in the upper Oligocene (P21b), *S. bulloides* with a FO in the upper lower Oligocene (P19), and *L. pauperata* with a stratigraphic range from the lower Oligocene (P18 or P19) to the Pleistocene (N23).

Assemblage 4A (Early Oligocene–Early Late Eocene)

Cores 182-1126D-20R through 24R

Assemblage 4A is dominated by numerous small tests of *S. subspinosa, Stilostomella subspinescens,* and *Stilostomella* spp. Many of the tests are poorly preserved and partially dissolved. Also present as minor elements of the assemblage are *O. umbonatus, C. praemundulus, Cibicidoides* spp., *Lenticulina* spp., *Pullenia,* spp., *G. subglobosa, V. spinosa, H. ammophila,* and various nodosariids. The absence of *Nuttallides truempyi* from the assemblage suggests that the site remained above this species' upper depth limit (lower to middle bathyal) during the early late Oligocene to early Oligocene. This assemblage shows close similarity to the assemblage (PC1) dominated by *Stilostomella* spp. and *Lenticulina* spp. recorded by Mackensen and Berggren (1992) from lower–middle Eocene sediments at Site 748 on the Kerguelen Plateau. These authors noted that the *Stilostomella-Lenticulina* assemblage disappeared in the late Eocene at Site 748, to be replaced by an assemblage characterized by newly evolved Oligocene species.

Assemblage 4B (Early Late–Late Middle Eocene)

Cores 182-1126D-25R through 27R

Assemblage 4B is characterized by the presence of *N. truempyi, O. umbonatus, H. ammophila, Cibicidoides mexicanus, C. praemundulus,* and *Cibicidoides* spp. In addition, *G. subglobosa, Lenticulina* spp., and *Pullenia* spp. also occur within this assemblage. The presence of *N. truempyi* suggests a well-oxygenated environment at middle to lower bathyal paleodepths. In a study of Paleocene and Eocene assemblages from the southern Atlantic Ocean, Tjalsma and Lohmann (1983) concluded that the bathymetric range of *N. truempyi* had been restricted to abyssal depths during most of the Paleocene, but became extended to lower and middle bathyal depths in the latest Paleocene. The change in composition between Assemblage 4B and Assemblage 4A suggests that the site was at deeper bathyal depths in the middle–early late Eocene than in the early late Eocene–earliest Oligocene. Assemblage 4B is very similar to the lower Eocene assemblage (PC IV) from Site 747 on the Kerguelen Plateau described by Mackensen and Berggren (1992). The *N. truempyi*-dominated assemblage was only observed at Site 747 in the early Eocene, whereas an assemblage dominated by *Stilostomella* and *Lenticulina* spp. was recorded at Site 748 in the lower and middle Eocene. Mackensen and Berggren (1992) suggested that, in contrast to Site 747 during the early Eocene, Site 748 was situated above the upper paleodepth limit of *N. truempyi* during the early and middle Eocene.

Sedimentation Rates

Sediment accumulation rates were calculated from preliminary biostratigraphic data from Site 1126; the results are presented in Fig. **F7.** The biostratigraphic datum levels used to calculate sedimentation rates are listed in Table **T2.**

The sedimentation rate is ~31 m/m.y. in the Pleistocene section and slows to 24 m/m.y. in the lower Pliocene. Rates alternate between 11–15 m/m.y. and 7–8 m/m.y., with the faster rates in the upper Miocene, lower Miocene, and upper Oligocene, and slower rates in the intervening sections. The sedimentation rate curve clearly delineates three hiatuses suggested by disjunct biozones (see **"Calcareous Nannofossils,"** p. 13, and **"Planktonic Foraminifers,"** p. 16), however, the youngest hiatus is not discernible on Figure **F7** (missing Zones NN18–NN17 at ~56 mbsf). The second hiatus occurred between 2 and 3.8 Ma, between the LOs of *D. brouweri* and *R. pseudoumbilicus* at ~67 mbsf, where Zones NN15–NN13 are missing. The third hiatus occurred between 4.5 and 7.8 Ma, between the FO of *G. crassaformis* and the LO of *M. convallis* at ~118 mbsf, where Zone NN11 is missing. Reworked Paleogene nannofossils (such as the Eocene *N. dubius*) were found near this disconformity. The oldest hiatus occurred between 10.80 and 13.60 Ma between the LOs of *C. miopelagicus* and *S. heteromorphus,* with the upper middle Miocene missing (Zones NN9–NN6). There is no obvious paleontologic evidence of hiatuses in the Oligocene and Eocene sections, as all nannofossil zones and most foraminifer zones are present. The continuity of the record, however, is in question because of poor core recovery.

F7. Sedimentation rate curve from datum levels, **p. 54.**

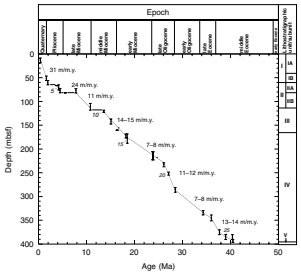

T2. Datum levels used in the graph of sedimentation rate, **p. 88.**

PALEOMAGNETISM

At Site 1126 archive halves of all APC, XCB, and RCB cores were measured in the 2G 760-R magnetometer, except for those core sections obviously disturbed by drilling or with inadequate recovery for meaningful measurements. The cores were routinely measured as natural remanent magnetization (NRM) and after 20-mT demagnetization. A few were measured with additional intermediate steps up to 30-mT demagnetization. One core was measured as a whole core and the results were compared with archive-half measurements performed later. Strongly lithified fragments whose orientation in the core could be determined were measured as discrete samples. Rock magnetic analysis was performed on samples from soft sediments, on lithified pelagic limestones, and on sandstones. These analyses were performed using the methods described in "Paleomagnetism," p. 12, in the "Explanatory Notes" chapter.

Long-Core Measurements

The results of long-core measurements of the nannofossil ooze cores from Holes 1126A and 1126B were disappointing. The NRM was dominated by a vertically downward coring contamination that was largely removed by 20-mT demagnetization, whereupon the signal was almost uniformly reduced to the noise level of the instrument. In addition, there were anomalous peaks in intensity near the top of most cores that were so large that we interpret them as some form of contamination introduced either by coring or by treatment on board. Only a single core (Core 182-1126B-19H) gave a sequence of reversals that could be correlated with the geomagnetic polarity time scale (Fig. F8). A comparison between whole-core and archive-half core measurements showed that the two measurements of inclination are not significantly different, but there are systematic differences in declination that remain to be interpreted. Although not as convincing as the Core 182-1126B-19H results, possible reverse-to-normal reversals were observed in Cores 182-1126B-5H (41.0 mbsf), 182-1126C-5H (44.2 mbsf), 182-1126B-9H (81.2 mbsf), and 182-1126B-17H (131.4 mbsf). Intervals of uniform normal polarity were observed in Cores 182-1126B-3H and 5H, and intervals of reversed polarity were observed in Core 182-1126B-17H. A common feature of many of the cores was that the upper halves of cores had major spikes in intensity and unrealistically rapid fluctuations in inclination that were not present in the lower halves. Poor recovery between Cores 182-1126B-19H and 27X precluded further long-core observations, but measurements were successful on nannofossil chalk recovered in Cores 182-1126B-27X, 28X, and 29X, where reversals were again observed.

In Hole 1126D the sandstone in Cores 28R to 33R gave a strong and stable NRM that had a predominantly steep upward or normal inclination, with an average value of 67.3° and a standard deviation of 14° (175 determinations). This corresponds to a paleolatitude of ~50°S.

F8. Inclination measurements from Core 182-1126B-19H, p. 55.

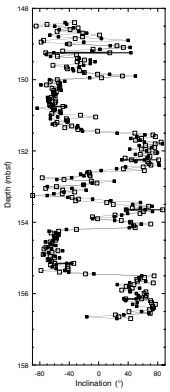

Discrete Samples

Discrete samples were analyzed to aid interpretation of the NRM. In most cases, Zijderveld plots failed to define characteristic magnetizations primarily in the nannofossil oozes, although in Cores 182-1126B-18H to 19H, and particularly in 19H, the remanence was stronger, per-

mitting further cleaning before the signal became too weak for measurement. However, only the nannofossil chalks and the sandstones gave good Zijderveld plots with maximum angular deviation angles of <5°. Results for Sample 182-1126D-33R-2, 87–89 cm, are shown in Figure **F9.** A soft component that is oriented steeply downward was demagnetized by 5 mT. There was then a univectorial decay close to the origin, indicating the isolation of a characteristic direction of magnetization.

Rock magnetism analysis consisted of measurements of weak-field susceptibility at two frequencies, progressive isothermal remanent magnetization (IRM) acquisition, alternating field demagnetization of anhysteretic remanent magnetization (ARM) and IRM, and low-temperature observations of warming curves of IRMs induced at liquid nitrogen temperature. The rock magnetism characterizations of the samples are presented in the form of modified Cisowski plots (Cisowski, 1981). In these plots the acquisition of IRM and the demagnetization of NRM, ARM, and IRM are shown in absolute values. Examples of these are presented in Figure **F10** for weakly and more strongly magnetized nannofossil ooze, nannofossil chalk, and sandstone.

Sample 182-1126B-1H-7, 6–8 cm (Fig. **F10A**), is representative of the weakly magnetized nannofossil ooze. The IRMs and ARM are well above the 10^{-4} A/m (or 10^{-1} mA/m) noise level of the instrument even after demagnetization, whereas the NRM is within the noise level and shows no systematic behavior. The magnetic material in this sample has an extremely hard component and cannot be simply magnetite. Indeed, from the IRM acquisition curve it is evident that our use of a 100-mT field for ARM would not excite the hardest particles. Sample 182-1126B-19H-3, 59–61 cm (Fig. **F10B**), which provided the good record of reversals, is quite different, having an NRM that demagnetizes systematically and is above the noise level even after 40-mT demagnetization. The acquisition of IRM is consistent with magnetite as the dominant carrier. The high ARM:IRM ratio suggests that it is in a single-domain state, consistent with a biological source. Sample 182-1126D-11R-1, 14–16 cm (Fig. **F10C**), comes from the nannofossil chalk and is magnetically similar to the more strongly magnetized nannofossil oozes with an NRM that systematically demagnetizes above the noise level of the instrument and a high ARM:IRM ratio. Sample 182-1126D-33R-1, 58–60 cm (Fig. **F10D**), from the sandstone has a saturation IRM two orders of magnitude greater than the carbonates and the NRM is two orders above the noise level of the instrument. The ratio of NRM to IRM is appropriate for a depositional remanence.

Susceptibility was measured at the two available frequencies on the Bartington MS2 (0.465 kHz and 4.65 KHz) to estimate superparamagnetic content (Mullins and Tite, 1973). The lower negative susceptibility at the higher frequency demonstrates that there is indeed a superparamagnetic component. However, the negative susceptibility of the nannofossil oozes and chalk, reflecting the diamagnetism of the dominant carbonates, precludes determination of the amount of superparamagnetic material present. In contrast, in the sandstone, which has positive susceptibility, the difference is ~10%. This is comparable with values for dusts or unweathered surface soils but is higher than most values for sandstones. Thus, it appears that this sandstone has an unusual amount of very fine magnetite that could reflect eolian input.

The low-temperature observations consisted of warming curves of IRMs induced at liquid nitrogen temperature to identify the changes in remanence at the Verwey transition of magnetite and the Morin transi-

F9. AF demagnetization behavior of Sample 182-1126D-33X, 87–89 cm, **p. 56.**

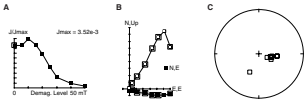

F10. Plots of demagnetization of NRM, ARM, and IRMs and of the acquisition of IRM, **p. 57.**

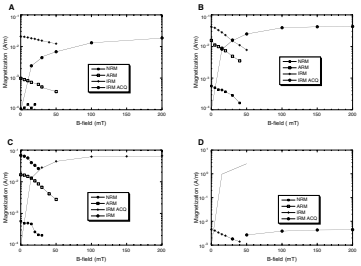

tion of hematite (e.g., Nagata et al., 1964). There were indications of the presence of magnetite in the form of knees in the curves at the Verwey transition of magnetite in samples from the nannofossil ooze that gave the good paleomagnetic signal and in the sandstone, whereas in the nannofossil chalk, a distinct dip was seen at the transition, implying low-temperature memory of magnetization across the transition (Nagata et al., 1964). In the sandstone sample, there was no sign of the hematite transition.

To summarize, the magnetic properties of the various samples differ in a manner that is consistent with the variation in their NRM. In the nannofossil oozes the NRM is for the most part below the sensitivity of the new 2-G instrument and the IRM and ARM are smaller than in the samples for which we could measure NRM.

Magnetostratigraphy

With only a single core displaying indisputable reversals in the nannofossil ooze cores, potential for magnetostratigraphy is limited. However, the nannofossil record demonstrates that Core 182-1126B-19H lies between 13 and 18 Ma and probably between 16 and 18 Ma. In addition, a very rough estimate of the overall sedimentation rate is 10 mm/10^3 yr. Hence, we seek a sequence of reversals following the pattern we have observed with an approximate time interval corresponding to 7 m of section, equivalent to 700,000 yr. C5Cr-C5Cn-C5Br provides a possible candidate pattern; accordingly, we provisionally interpret this sequence of reversals as representing the sequence from the end of C5Cr to the beginning of C5Br.

In the nannofossil chalk the stronger magnetization permitted the detection of reversals, but the discontinuous nature of the record made interpretations tentative. However, it appears that C7n is recorded in the interval with the top at 217.8 mbsf.

Only normal magnetizations were observed in the sandstone, which would be consistent with magnetization in the Cretaceous normal superchron but could also reflect rapid sedimentation in a normal chron. The observed inclination gives a paleolatitude of ~50°S for the site at the time of magnetization. This is higher than the present latitude of the site and is consistent with the northerly motion of this part of the ocean floor as it moved away from the Antarctic-Australian spreading center to its present latitude.

COMPOSITE DEPTHS

Introduction

Construction of the composite section from Holes 1126B and 1126C indicates that a nearly complete record of the upper Miocene–Pleistocene sedimentary section was recovered at Site 1126. Comparison of overlap between cores from adjacent holes was used to establish the degree of section continuity. Using the Splicer software, sedimentary features and physical properties present in adjacent holes were aligned so that they occur at approximately the same depth. This alignment was performed downward from the mudline, and an offset value was added to the mbsf depth of each core to create a meters composite depth (mcd) for each core. Table T3 (also in ASCII format) relates the mbsf depths to mcd depths for each core and section at Holes 1126A, 1126B,

T3. Site 1126 core and section depths in mcd and mbsf, p. 89.

and 1126C and provides offset values for the conversion of mbsf to mcd.

Data Input

The primary lithologic parameters used to create the composite section were color reflectance data (400 nm) measured on split cores, natural gamma radiation (NGR) emissions data collected by the multisensor track (MST) on whole-round cores, and gamma-ray attenuation (GRA) wet bulk density data also acquired by the MST (Fig. F11). For specifics regarding data collection procedures and parameters, see "Physical Properties," p. 33. Magnetic susceptibility data, normally quite useful for correlation, were used sparingly because of very low values (range of –3 to 1) resulting in a very low signal to noise ratio. The MS signal was dominated by an unidentified nonrandom noise that produced a pronounced positive excursion at the top of each section and then diminished downsection. The *P*-wave velocity data collected by the MST were of poor quality as a result of numerous voids in the cores and they were not used for correlation purposes. The GRA bulk density estimates were useful for correlation but were found to vary in response to core disturbance. Natural gamma radiation data were useful for correlations but were acquired at lower resolution than other data (16 cm vs. 4 cm for GRA data). After assessing all the data it appeared that color reflectance data, collected at 4-cm intervals, provided the best tool for identifying correlative features between cores.

Biostratigraphic data aided in correlations by providing additional datums that were compared between holes (Table T4) (see "Biostratigraphy," p. 12). Planktonic foraminifers were particularly useful in constraining correlative intervals of the recovered section and corroborating ties based on physical properties. Because most biostratigraphic samples were taken from core catchers, the stratigraphic error is generally on the order of 10 m (the distance between core catchers in consecutive cores).

Composite Section Construction

Correlations between cores were hindered by significant differential core distortion, particularly at the very top of each core where a much-expanded record was sometimes indicated. This core distortion allows similar data characteristics to be identified between holes, but it results in an unsatisfactory statistical comparison. Insufficient overlap was also a problem for statistical comparison of the records. Correlations were further hindered by poor core recovery below 100 mbsf, resulting from the presence of multiple thick chert layers interbedded with easily deformable hemipelagic ooze (see "Lithostratigraphy," p. 4).

The Pleistocene and upper Pliocene records are easily correlated between holes. The Pliocene/Pleistocene boundary occurs at ~40 mcd, based upon biostratigraphic data (Fig. F12). The Pleistocene record is characterized by high-amplitude (40 percentage units) oscillations in color reflectance over depth intervals of ~2–4 m. The upper Pliocene section is characterized by lower amplitude (10–20 percentage units) and thinner oscillations over depth intervals of ~0.5 m. Data peaks have very similar characteristics between cores, facilitating easy correlation down to ~60 mcd. An exception to this occurs in Cores 182-1126B-4H and 182-1126C-4H, which exhibit significant distortion and disruption of the record by slumping. Below 60 mcd large data gaps and the

F11. Composite depth section produced using Splicer software, p. 58.

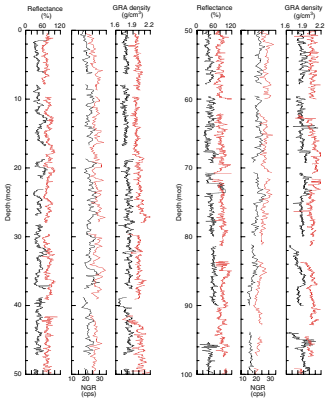

T4. Biostratigraphic data used for splice correlation, p. 93.

F12. Spliced section of smoothed color reflectance data produced using Splicer software, p. 60.

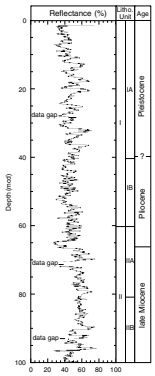

presence of numerous slumps made correlations difficult and highly tentative.

Color reflectance resolves the finer lithologic structure corresponding to cyclic sedimentation patterns on a scale of tens of centimeters or greater. Throughout much of the Pleistocene and Pliocene section the low reflectance corresponds to glauconitic wackestones at the base of a cycle, which grade upsection into nannofossil/foraminiferal oozes with higher reflectance. Depositional sequences are bounded by abrupt burrowed contacts. The record of NGR reveals features with very similar characteristics to the color reflectance data over scales of 1 m or more. Overall, there is an inverse correlation between color reflectance data and NGR data (Fig. F12), indicating higher radioactive emissions in the darker, more clayey wackestone layers (see "Physical Properties," p. 33). The similarity in patterns between the records was useful for correlation purposes.

The composite section indicates good agreement between the lithostratigraphic records in Holes 1126B and 1126C, with several exceptions. From the mudline to ~30 mcd (mid-Pleistocene sediments) the records are nearly identical (Fig. F11). Between 30 and 40 mcd the large-scale structure is similar, but the interval in Hole 1126C appears compressed with respect to Hole 1126B based on color reflectance and NGR data, resulting in offsets in the records. Correlations using NGR provide the highest degree of confidence in this particular interval. There is also some extreme sediment disturbance (fluidization of sediments) in the top section of Core 182-1126C-4H that destroyed the record from 26.9 to 28.4 mcd (25.5–27.0 mbsf in Hole 1126C). Coherence between the data records is attained again at 40 mcd and is maintained to 59 mcd. From 59 to ~62 mcd the record in both holes is greatly disturbed by slumping. Intermittent slump deposits continue downward to ~118 mcd in Holes 1126B and 1126C (~116 mbsf in both holes), making correlations between records tenuous and intermittent. Below 110 mcd core recovery is significantly lower and correlations continue to be difficult and intermittent. Because a single offset value is assigned to each core, individual features within a core cannot be stretched or compressed using the Splicer software. As a result, not all features in adjacent cores are aligned during composite section construction. Further processing of the data files is necessary to achieve an improved alignment.

Construction of the composite and spliced sections indicates that recovery of the Pleistocene section was nearly complete except for a minor gap at ~28 mcd (Table T5, also in ASCII format; Figs. F11, F12). There may in fact be several centimeters of overlap at 28 mcd; however, there is not enough overlap to provide any confidence in a tie at this level. The Pliocene section is nearly complete except for minor gaps in the record at ~71 and 81 mcd. Biostratigraphic data indicate that the gap at 81 mcd must be on the order of centimeters. Recovery in the upper Miocene section and downward was not as complete, with a minor gap occurring at 93 mcd and a major gap occurring at 138–144 mcd. The actual splice is therefore incomplete below 28 mcd. Splicing was not continued below 100 mcd because of core distortion and poor recovery. The mcd scale expansion relative to the mbsf scale is ~10% from 0 to 100 mcd. Below 100 mcd the offsets become more variable as a result of the core distortion and poor recovery.

The Splicer software allows the user to tune the core data to an age series. An initial attempt to tune the color reflectance data to a composite seawater $\delta^{18}O$ curve (Raymo et al., 1989; Shackleton et al., 1990;

T5. Splice tie points, p. 94.

Shackleton et al., 1995) produced positive results (Fig. F13). This method assumes that facies successions within the cores are a function of eustasy and the $\delta^{18}O$ curve is an adequate proxy for eustasy. An initial age model was produced using the biostratigraphic datums (Table T4). Tuning was then accomplished by establishing ties between the core data and the time series data using the biostratigraphic datums as constraints. The Splicer software provides a statistical evaluation of the proposed tie. Upon correlation the age of the tie is applied to the age model for the core data. The tuned record reveals a good correspondence between color reflectance oscillations and glacial-interglacial stages at least back to 1 Ma (Fig. F13). The correlation suggests that the high-reflectance, nannofossil/foraminiferal oozes are deposited during sea-level highstands. Beyond 1 Ma the lower amplitude and higher frequency of the $\delta^{18}O$ record make correlations difficult. This preliminary investigation suggests that Site 1126 may yield a nearly complete $\delta^{18}O$ record for at least the Pleistocene.

F13. Spliced and tuned color reflectance record for Site 1126 compared to Site 656 composite seawater $\delta^{18}O$ curve, p. 61.

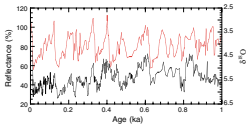

ORGANIC GEOCHEMISTRY

At Site 1126, in addition to routine monitoring of hydrocarbon gases for safety, analyses were conducted for inorganic carbon, total carbon, nitrogen, and sulfur. The analytical procedures are described in "Organic Geochemistry," p. 16, in the "Explanatory Notes" chapter.

Volatile Hydrocarbons

At Site 1126, concentrations of volatile hydrocarbons were routinely determined from every core using the standard ODP headspace sampling procedure (Table T6). Only low concentrations of methane and ethane are present. From the surface to a depth of 236 mbsf, the concentration of methane varies between 4.6 and 13.6 ppm. Below 253.7 mbsf, methane concentrations are between 2 and 5 ppm and most samples have <3 ppm. Ethane at concentrations from 1.1 to 2.7 ppm was present in five samples between 186.5 and 236 mbsf, but was not detected at greater depths. One gas pocket observed in the core at 97.3 mbsf and sampled by the vacutainer method directly through the core liner had 32 ppm methane and 1 ppm ethane.

T6. Hydrocarbon gas compositions, p. 95.

Inorganic and Organic Carbon, Sulfur, and Nitrogen

Inorganic carbon concentrations were converted to calcium carbonate percentages (see "Organic Geochemistry," p. 16, in the "Explanatory Notes" chapter). In the upper 116 mbsf the carbonate content is uniformly high at 80 to 91.2 wt% (Table T7; Fig. F14). From 116 to 254.2 mbsf the carbonate values are highly variable, ranging from 30.6 to 93.2 wt%. As a result of poor core recovery, no samples are available in the interval from 254.2 to 348.6 mbsf. Between 348.6 and 389.6 mbsf the carbonate content is again at high levels and falls within a narrow range of 79.5 to 90.0 wt%. Low carbonate values (0.4–0.6 wt%) occur at the base of Hole 1126D from 406.4 to 454.5 mbsf, except for one sample at 409.3 mbsf with a carbonate content of 69.3 wt%.

Organic carbon (C_{org}) is low throughout the section except for the deepest sample from Hole 1126D, which has 1.3 wt% organic carbon (Table T7; Fig. F14). All other organic carbon values fall within the range of 0 to 0.8 wt% at Site 1126. In the upper 100 mbsf of sediment at

T7. C, N, and S data, p. 96.

F14. $CaCO_3$ and C_{org} contents of samples, p. 62.

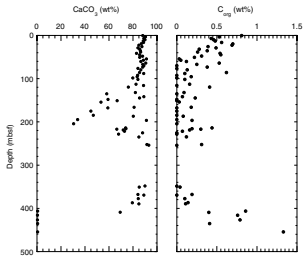

Hole 1126B, C_{org} decreases from 0.8 wt% in near-surface sediments to <0.2 wt% in deeper samples. C_{org} values for most samples in Holes 1126B and 1126D below 100 mbsf are <0.2 wt%. As a result of low organic carbon contents, no samples were analyzed for Rock-Eval parameters.

Only seven samples have measurable concentrations of nitrogen (0.04–0.10 wt%) (Table T7). Sulfur content varies from 0 to 1.62 wt% (Table T7). From the surface to 54.5 mbsf sulfur ranges from 0.1 to 0.3 wt%. Below 57.5 mbsf in 1126B sulfur is mostly below detection level with a few samples having 0.1 to 0.2 wt% sulfur. In Hole 1126D sulfur is below detection level until the base of the hole where values from 0.1 to 1.6 wt% were measured.

INORGANIC GEOCHEMISTRY

Interstitial Waters

Whole-round cores for interstitial water analysis from Holes 1126A and 1126B were taken at a rate of two samples per section in the upper five cores, one per core down to Core 182-1126B-8H, and every other core thereafter, recovery permitting. No samples were taken from Hole 1126C. Samples from Hole 1126D were taken at a rate of one sample every other core, recovery permitting. Samples were analyzed according to the procedures outlined in "Inorganic Geochemistry," p. 18, in the "Explanatory Notes" chapter. These data are presented in Table T8 and Figures F15, F16, F17, F18, and F19.

T8. Interstitial water geochemistry, p. 98.

Salinity and Chlorinity

Salinity and chlorinity show no change in the upper 10 mbsf of Holes 1126A and 1126B. Below this interval salinity increases to a value of 100 by ~100 mbsf (Fig. F15). Chlorinity is linearly related to salinity over the entire core. Increases in salinity can be caused by a variety of factors, the origin of which can be constrained by changes in the ratio of cations to chloride (see "Discussion," p. 32).

F15. Summary of unnormalized anion trends, p. 63.

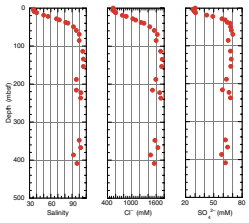

Calcium, Magnesium, Potassium, Lithium, Silica, and Strontium

Concentrations of Ca^{2+}, Mg^{2+}, K^+, Li^+, $H_4SiO_4^0$, and Sr^{2+} all increase with increasing depth and are correlated with changes in salinity (Fig. F16). The concentration of Ca^{2+} increases from 11.1 mM at a depth of 2.95 mbsf in Core 182-1126A-1H to a maximum of 49.7 mM in Core 182-1126B-17H. Although the increase in Ca^{2+} is not unexpected considering the increase in Cl^-, the concentration of Ca^{2+} increases in excess of expected changes in Cl^- (Fig. F17), giving a normalized change of between 7 and 8 mM Ca^{2+} over the length of the core. Increases in the concentration of Ca^{2+} relative to Cl^- could arise as a result of the dissolution of low-Mg calcite (LMC) or the influence of a $CaCl_2$ brine (see "Discussion," p. 32). The concentration of Mg^{2+} decreases slightly from 55.9 mM in Core 182-1126A-1H to 53.9 mM in Core 182-1126B-1H (Fig. F16). From this point the concentration increases to 130.9 mM at a depth of 134.7 mbsf in Core 182-1126B-17H. Despite the increase in the concentration of Mg^{2+}, the normalized concentration of Mg^{2+} decreases by ~24 mM by the bottom of the cored interval (Fig. F17). Ex-

F16. Summary of unnormalized cation trends, p. 64.

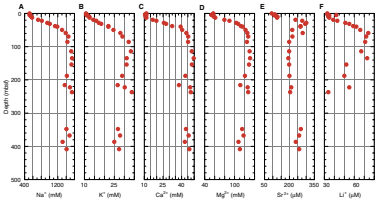

F17. Summary of normalized trends, p. 65.

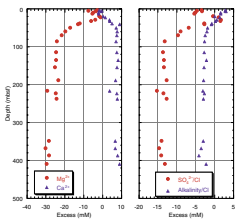

planations for the decrease in Mg^{2+} of pore fluids usually involve the formation of dolomite or interactions with clay minerals within the section (Gieskes, 1981). At Site 1126 dolomite is absent below 100 mbsf; therefore, the most plausible explanation is that the relatively low concentration of Mg^{2+} reflects either the alteration of clay minerals within the sedimentary section or inheritance from the original brine. Although K^+ shows relatively little change relative to Cl^- throughout the core, there is a slight decrease of between 1 and 2 mM in the concentration of K^+ normalized to Cl^- between ~20 and 80 mbsf. The relative decreases in K^+/Cl^- are probably caused by clay mineral diagenesis. For example, the conversion of kaolinite ($Al_2Si_2O_5(OH)_4$) to montmorillonite ($[Na_{0.2}\ K_{0.1}Mg_{0.1}Mg_{0.8}]Mg_{0.66}\ Al_{3.34}Si_{0.8}O_2(OH)_4$) will remove varying amounts of Mg^{2+}, K^+, and Na^+ from pore fluids (Loughnan, 1969).

Concentrations of Na^+ were determined using two different methods (see **"Inorganic Geochemistry,"** p. 18, in the "Explanatory Notes" chapter). Although the concentration of Na^+ measured using the ion chromatograph was within 5% (the error quoted for the ion chromatography method) of that calculated by difference in charge balance, the Na^+ calculated by difference gave much more consistent trends. In both cases the Na^+/Cl^- ratio throughout the core is similar to that of surface seawater (Fig. **F18**).

The concentration of Sr^{2+} relative to Cl^- increases significantly between 20 and 60 mbsf before falling below seawater values throughout the remainder of the core (Table **T8**). The increase in the Sr^{2+}/Cl^- ratio in the upper 40 mbsf arises from the recrystallization of biogenic aragonite and high-Mg calcite (HMC) (Swart and Guzikowski, 1988). The concentration of Sr^{2+} is limited by the solubility of celestite in the pore waters, which is approximately at saturation in the interval of maximum Sr^{2+} concentration. The Sr^{2+}/Ca^{2+} ratio decreases substantially in the lower portion of the core (Fig. **F19**).

The Li^+/Cl^- and $H_4SiO_4^0/Cl^-$ ratios show a steady decrease throughout the core. In contrast to previous ODP sites (e.g., Site 1003, Leg 166), the dissolved Li^+ concentration profile is dissimilar to that of Sr^{2+}, with the Li^+/Cl^- ratio decreasing from seawater ratios to 20 at the base of the core. Dissolved Li^+ concentrations have been suggested to be influenced by the early diagenesis of opal-A, the recrystallization of biogenic carbonate, and reactions involving clay minerals (Gieskes, 1983).

F18. Summary trends in the Na^+/Cl^- ratio with increasing depth, **p. 66.**

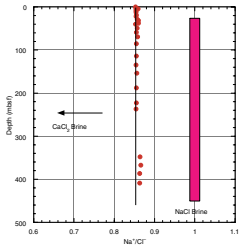

F19. Downhole variation in the Sr^{2+}/Ca^{2+} ratio of pore waters, **p. 67.**

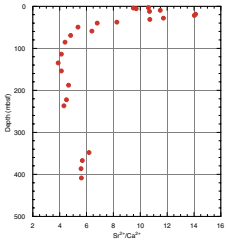

Sulfate, Alkalinity, and pH

The concentration of SO_4^{2-} normalized to Cl^- shows a small decrease from a seawater value of 54 to 47.3 in Core 182-1126B-2H at a depth of 12.40 mbsf. Below this depth the ratio increases again to approximately seawater values before decreasing substantially to ~40 below 70 mbsf (Fig. **F17**). The decrease in the lower portion of the core is not associated with any increase in alkalinity or noticeable smell of hydrogen sulfide (H_2S). One possible explanation is that the brines had become depleted in SO_4^{2-} before their emplacement in the sediments. The alkalinity/Cl^- ratio reaches a maximum at 5.95 mbsf in Core 182-1126A-1H. The maximum reduction in the SO_4^{2-}/Cl^- ratio in the upper portion of the core occurs 6 m above the alkalinity maximum. A slight odor of H_2S was noted in this interval. A pH minimum occurs at a depth of 58.9 mbsf in Section 182-1126B-7H-4. Trends in pH, determined from initial millivolt readings taken during alkalinity titrations and using the punch-in electrode, were similar.

Discussion

The geochemistry of pore fluids at Site 1126 is dominated by the dramatic increase in salinity, which is manifested as shallow as 9.4 mbsf. The salinity reaches a value of ~106 by a depth of 134.7 mbsf in Section 182-1126B-17H-4. Although there is some variation, this value is maintained throughout the remainder of the core, and it is probable that the small decreases seen in the lower portion of the core result from contamination by seawater introduced during drilling.

The occurrence of high-salinity pore waters in continental slope sediments is not unusual and has been documented at numerous other locations (Sotelo and Gieskes, 1978; Couture et al., 1978; Suess, von Huene, et al., 1988; Kastner et al., 1990). In sediments drilled off the Peruvian coast during Leg 112, high salinity values were measured at several sites and were inferred to result from multiple origins, including (1) dense brines arising from Holocene evaporitic systems on the adjacent land masses, (2) dissolution of evaporitic minerals at depth, and (3) fossil brines (Suess, von Huene, et al., 1988). As in the case of the sites drilled during Leg 112, the formation of gas hydrates at Site 1126 can be ruled out as the source of brines because not only is the temperature-pressure regime at Site 1126 not conducive for hydrate formation, but concentrations of methane at Site 1126 are too low for gas hydrate formation. Although the precise origin of the brines at Site 1126 cannot be ascertained at this stage, some constraint can be placed by an examination of the ratios of the major cations relative to Cl^-. In particular, if the brine formed from the dissolution of NaCl (halite), then the pore water would tend to have a Na^+/Cl^- ratio near unity. In the case of the data from Site 1126, the Na^+/Cl^- ratio, determined using the Na^+ calculated by difference, is essentially the same as seawater throughout the core. If the value for Na^+ measured using ion chromatography is used (see **"Inorganic Geochemistry,"** p. 18, in the "Explanatory Notes" chapter), then the Na^+/Cl^- ratio is slightly elevated with respect to seawater, although still below the value expected from the dissolution of halite (Fig. **F18**). Dissolution of other types of evaporitic facies can also be ruled out because in spite of the increase in the Ca^{2+}/Cl^- ratio, which might reflect the dissolution of gypsum or anhydrite, there is a decrease in the SO_4^{2-}/Cl^- ratio, which suggests consumption rather than addition of SO_4^{2-}. Consequently, the most plausible explanation for the increased salinity is the presence of a partially evaporated fossil brine. This brine could have been forced into the sediments during a previous sea-level lowstand when a significant portion of the adjacent continental shelf would have been exposed and possibly acted as an evaporitic lagoon.

X-Ray Mineralogy

The sediments at Site 1126 are composed of aragonite, HMC, and LMC, with smaller amounts of quartz, dolomite, and clay minerals in the upper 60 mbsf (Table **T9,** also in **ASCII format;** Fig. **F20**). This interval corresponds to lithostratigraphic Unit I (see **"Lithostratigraphy,"** p. 4). The origin of dolomite within this unit is unknown; the dolomite could either be authigenic, related to the small amount of oxidation of organic material observed in the pore-water profiles, or detrital in origin. In lower portions of the hole, aragonite and HMC disappear, prob-

T9. XRD data, **p. 99.**

F20. Variations in mineral concentrations, **p. 68.**

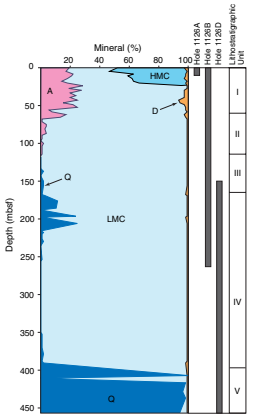

ably as a result of diagenesis, and dolomite is also absent. Unit IV (see "Lithostratigraphy," p. 4) is composed mainly of LMC and quartz.

PHYSICAL PROPERTIES

Introduction

Measurements of physical properties at Site 1126 followed the procedures outlined in "Physical Properties," p. 19, in the "Explanatory Notes" chapter. These included nondestructive measurements of *P*-wave velocity (every 4 cm; Table T10, also in ASCII format), GRA bulk density (every 4 cm; Table T11, also in ASCII format), MS (every 8 cm; Table T12, also in ASCII format), and NGR (every 16 cm; Table T13, also in ASCII format) using the MST. The *P*-wave logger (PWL) was activated only on APC cores. Thermal conductivity (Table T14, also in ASCII format) was measured in unconsolidated sediment at a frequency of one per core with three samples per core analyzed after deployments of the Adara and DVTP tools. A minimum of two discrete *P*-wave velocity measurements per section were made on the working half of the split cores (Table T15, also in ASCII format). Measurement frequency was increased to five per section after the PWL was turned off. Standard index properties (Table T16, also in ASCII format) and undrained shear strength (Table T17, also in ASCII format) (only in unconsolidated sediments) were measured at a frequency of one per section.

The following sections describe the downhole variations in sediment physical properties and their relationships to lithology and downhole logging measurements. Variations in MS are described within "Paleomagnetism," p. 24, and "Composite Depths," p. 26.

Index Properties, *P*-Wave Velocity, Natural Gamma Radiation, and GRA Densiometry

At Site 1126 an offset was seen between the discrete bulk density measurements and the GRA densiometry measurements of the MST (Fig. F21). This offset was corrected using the equation of Boyce (1976) as described in "Index Properties," p. 21, in the "Explanatory Notes" chapter. Low core recovery below 160 mbsf hindered the ability to investigate petrophysical properties within the middle and lower parts of the sedimentary section (Fig. F22). Despite this, physical properties measurements at Site 1126 can be divided into five units on the basis of variations in measured parameters (Fig. F22).

Physical properties Unit (PP Unit) 1 (0–45 mbsf) is characterized by high NGR (5–15 cps) with an overall trend of increasing *P*-wave velocities (1.5 to 1.75 km/s) and bulk density (1.7 to 1.82 g/cm^3) (Fig. F23). Within PP Unit 1 porosity (50%–61%) is generally inversely correlated with bulk density and *P*-wave velocity (Fig. F23). Physical properties Unit 1 has been further divided into three subunits (Fig. F23). Physical properties Subunit 1A (0–6 mbsf) is characterized by increasing trends in bulk density (1.70–1.76 g/cm^3), *P*-wave velocity (1.6–1.65 km/s), and NGR (4–12 cps). Physical properties Subunit 1B (6–11 mbsf) has bulk density and *P*-wave velocity trends opposite to those in Unit 1A, whereas NGR remains nearly constant (~11 cps). Physical properties Subunit 1C (11–45 mbsf) is characterized by increasing bulk density (1.7–1.84 g/cm^3), increasing *P*-wave velocity (1.6–1.74 km/s), and nearly constant NGR values (~10 cps). The base of PP Unit 1 coincides

T10. *P*-wave velocity measurements, p. 101.

T11. GRA-densiometry measurements, p. 102.

T12. Magnetic susceptibility measurements, p. 103.

T13. Natural gamma-ray measurements, p. 104.

T14. Thermal conductivity measurements, p. 105.

T15. Discrete *P*-wave velocity measurements, p. 106.

T16. Index properties measurements, p. 107.

T17. Undrained shear strength measurements, p. 108.

F21. GRA densiometry values vs. discrete bulk density measurements, p. 69.

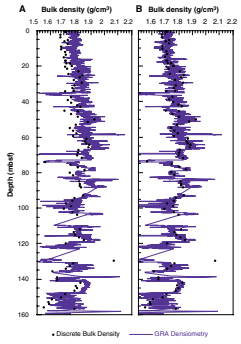

with the upper Pliocene/Pleistocene boundary, the bottom of lithostratigraphic Subunit IA, and the base of seismic Sequence 2 (see "Seismic Stratigraphy," p. 39).

Physical properties Unit 2 (45–81 mbsf) coincides with seismic Sequence 3A and is characterized by high NGR (5–14 cps), increased *P*-wave velocities (1.6–2.0 km/s), and relatively low porosity (42%–55%) (Fig. F22). Physical properties Unit 2 has also been divided into three subunits (Fig. F23). Physical properties Subunit 2A (45–60 mbsf) is characterized by an increasing trend of *P*-wave velocity (1.67–1.84 km/s), a variable trend in bulk density averaging near 1.72 g/cm³, and nearly constant NGR near 9 cps. The top of PP Subunit 2B (60 mbsf) occurs at the same depth as lithostratigraphic Unit II, characterized by the first occurrence of slumping in the sedimentary sequence. The top of PP Subunit 2C (68 mbsf) marks the beginning of a decreasing trend of NGR to the bottom of Unit 2 (14–3 cps). Within this subunit bulk density (1.8 g/cm³) and *P*-wave velocity (1.75 km/s) are nearly constant. The top of PP Subunit 2C also marks the start of a generally increasing trend in porosity that continues throughout Unit 3 (Fig. F22). At the base of PP Unit 2 (81 mbsf) NGR values decrease to an average of 3 cps (Figs. F22, F23). This decrease is coincident with the loss of aragonite, which is often high in uranium and thus a source of NGR. This conclusion is supported by spectral gamma-ray data from downhole logging, which show a trend of decreasing uranium values to 81 mbsf (see "Downhole Measurements," p. 35). Despite the limited overlap between core measurements and downhole logs, trends in NGR correlated well between the two data sets in the upper 80 mbsf of the section. The bottom of PP Unit 2 coincides with the lower Pliocene/upper Miocene boundary.

Physical properties Unit 3 (81–160 mbsf) is characterized by nearly constant *P*-wave velocities (~1.7 km/s) and NGR (3 cps) (Figs. F22, F23). These low NGR values are barely above detection levels and reflect the high carbonate and low terrigenous content of sediments within PP Unit 3. The GRA and discrete bulk density values both show cyclic variations between 1.6 and 1.9 g/cm³ (Fig. F23). The origin of these cyclic variations is not obvious, as they were not seen in other data sets. The bottom of PP Unit 3 corresponds to the base of seismic Sequence 3 and the base of lithostratigraphic Unit III. Distinct shifts in several downhole measurement logs at 180 mbsf indicate that the base of PP Unit 3 may actually be deeper than 160 mbsf, although poor core recovery prevents confirmation of this hypothesis.

Poor recovery in PP Unit 4 (160–404 mbsf) limits the ability to characterize unit-wide changes in geophysical properties (Fig. F22). With the exception of NGR, there is a high variability in all physical properties parameters. This arises as a consequence of lithologic alternations of unindurated (ooze) and indurated sediment (porcellanite and chert). *P*-wave velocities range from 1.65 to 5.4 km/s, bulk density from 1.62 to 2.15 g/cm³, and porosity from 40% to 62% (Fig. F22).

Physical properties parameters change dramatically at the top of PP Unit 5 (404–463 mbsf), which corresponds to an ~35-m.y. hiatus between Cretaceous? sandstones and Tertiary marine carbonate sediments. This boundary is marked by a sharp increase in NGR from 5 to 30 cps caused by greater amounts of radioactive elements within minerals in the sandstones. *P*-wave velocities in PP Unit 5 have a wide range of values (1.8–4.8 km/s) as a result of variable lithification (Fig. F22). Poor recovery limited our ability to collect measurements and discern trends in bulk density and porosity.

F22. *P*-wave velocity, GRA and MAD bulk densities, porosity, magnetic susceptibility and NGR, p. 70.

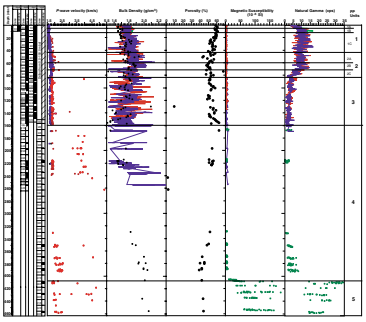

F23. GRA and MAD bulk densities, *P*-wave velocities, and NGR, p. 72.

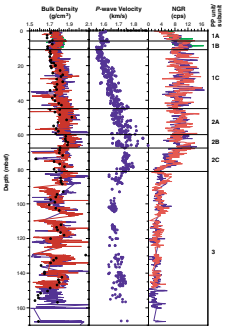

Natural gamma-ray data collected at Site 1126 was the most useful data set for correlation, and it showed a strong inverse correlation to color reflectance data. This relationship was well documented at all sites during Leg 166 and results from a decrease in NGR with increased carbonate content (high reflectance) and an increase in NGR with increased terrigenous minerals (low reflectance) (Eberli, Swart, Malone, et al., 1997).

Overall, trends in *P*-wave velocity, porosity, and bulk density at Site 1126 do not solely reflect compaction, but rather indicate the importance of diagenesis in the upper 150 m of the sedimentary section. This diagenesis is reflected in part by the presence of extensive chert layers and more indurated carbonate sediments.

Shear Strength

Shear strength was measured from 1 to 250 mbsf at Site 1126 (Fig. F24; Table T17). Shear strength increases from an average of 10 kPa near the top of the succession to 80 kPa near the base of PP Unit 3 (160 mbsf) and then generally decreases below 160 mbsf to values averaging 30 kPa (Fig. F24). Shear strength variations exhibit discrete intervals of high values superimposed on an overall increasing trend resulting from compaction. Some of these intervals of increased shear strength occur near PP unit boundaries and are probably a result of diagenetic alteration (Fig. F24).

F24. Shear strength, Holes 1126B and 1126C, p. 73.

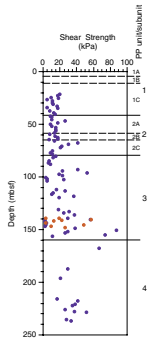

Thermal Conductivity

At Site 1126 thermal conductivity values increase from 1.0 W/(m·K) near the surface to 1.3 W/(m·K) at the base of Subunit 2A. Below this values decrease to an average of 1.1 W/(m·K) for the remainder of the measurements (Fig. F25; Table T14). Thermal conductivity is primarily dependent on variations in sediment bulk density, which is related to other sediment physical properties such as velocity; thus, these data sets are well correlated (Fig. F25).

F25. Thermal conductivity and *P*-wave velocity, p. 74.

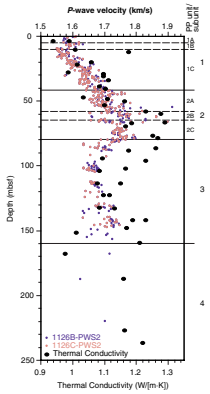

In Situ Temperature Measurements

Four in situ temperature measurements were made at Site 1126, three using the Adara tool and one using the DVTP. All tool runs gave reproducible estimates for mudline temperatures, although none of the measurements made within the sedimentary section proved to be reliable because of the influence of ship heave following emplacement (see "Operations," p. 2).

DOWNHOLE MEASUREMENTS

Logging Operations

After completion of drilling operations at Hole 1126D, the borehole was prepared for logging (see "Operations," p. 2). The lower limit of the BHA was placed below a chert horizon at 117 mbsf in an effort to avoid chert ledges against which the cable could get trapped and severed by pipe heave. All logging runs started at the base of the hole, which became progressively shallower during logging operations because of fill accumulation. The WHC was used throughout logging but

had difficulty coping with the complex cross-heave sea state. Three logging strings were deployed in the following order: (1) triple combo, including the Lamont-Doherty Earth Observatory high-resolution temperature/acceleration/pressure tool (LDEO-TAP); (2) sonic/GHMT combination; and (3) the WST (Table T18; also see "Downhole Measurements," p. 25, in the "Explanatory Notes" chapter).

T18. Tool strings, intervals logged, and logging speeds, Hole 1126D, p. 109.

The main pass with the triple combo and LDEO-TAP was run from 443 mbsf to the mudline. Before the main run a quality control pass was made from 443 to 380 mbsf with the accelerator porosity sonde (APS) switched off to prevent neutron charging of the formation. The WHC did not function in the intervals between 320 and 303 mbsf and between 197 mbsf and the seafloor after reaching the maximum limit of heave correction. The caliper on the hostile environment lithodensity sonde was closed at 150 mbsf and logging speed briefly increased between 175 and 165 mbsf to protect the tools from violent downheave.

The FMS tool was not included on the second tool string because of the risk of damaging the FMS caliper arms in the complex heave conditions. Because only the susceptibility magnetic sonde in the GHMT was functioning, the GHMT could be combined with the sonic tool on the second tool string, dispensing with the need for a dedicated GHMT run. The general-purpose inclinometer tool (GPIT) was also included on the second string to provide data on the effects of heave on tool motion. The sonic/GHMT was run from 430 mbsf to the seafloor. The WST recorded nine check-shot stations (stacks of sever or more shots) spaced ~30 m apart, adjacent to significant boundaries as indicated by the acquired logs and seismic stratigraphy (see "Seismic Stratigraphy," p. 39).

Data Quality

Although caliper measurements identified some borehole rugosity caused by washouts and caving at Hole 1126D, variations in borehole diameter fell within the range necessary for accurate measurement using eccentralized tools (e.g., porosity and density). The largest borehole diameters, approaching 45 cm (18 in), occurred between 140 and 150 mbsf and below 404 mbsf (Fig. F26). During logging, changes in cable tension and tool speed resulting from swell-induced heave degraded data collected in some intervals by causing repeated measurements. During the main triple combo run, neutron loading of the formation by the APS tool caused the gamma-ray log to record an artificial peak during downheave. These spurious measurements were later removed by processing. In general, triple combo data appear to be of reasonable quality, even in the interval in which the WHC was not operating. Reduced data quality for porosity and density occurs above 139 mbsf, where the caliper arm on the triple combo was closed approaching the pipe (Fig. F26).

F26. Geophysical logs vs. depth from triple combo and sonic/GHMT, p. 75.

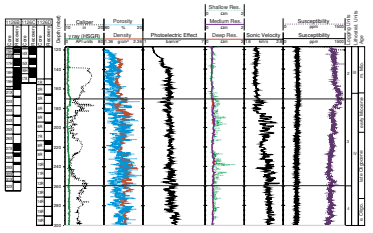

The sonic/GHMT pass produced quality data, even in the interval above 165 mbsf in which the WHC was not operating. Orientation measurements made by the GPIT were corrupted by the close proximity of other metallic tools, although the acceleration data should still provide useful information about how the tool string behaved in the complex heave conditions.

The check-shot survey was affected by borehole and/or the wireline noise, which increased uphole and was dominated by peak frequencies between 75 and 150 Hz. A few stations were abandoned because it was

not possible to get a clear first-arrival signal. Despite this, enough wavelets showed a clear first break suitable for check-shot purposes (see "Seismic Stratigraphy," p. 39). Damage to the cable may have affected data quality at the final station.

Data Presentation

All logs are plotted on a linear scale chosen according to maximum excursions of individual data sets (Figs. F26, F27, F28, F29). Porosity and density logs are plotted on compatible scales using the following relationship between density and porosity in a clean water-filled limestone:

$$p = \phi \times 1.0 + ([1 - \phi] \times 2.71),$$

where p = bulk density, ϕ = porosity, 2.71 = density of calcite (g/cm³), and 1.0 = density of (fresh) water (g/cm³). On this scale, porosity and density curves will coincide for clean, water-filled limestones, whereas mixing with other lithologies will be seen as either negative or positive separations between the curves (Rider, 1996).

Logging Units and Preliminary Interpretations

Low core recovery within the open-hole logged interval at Site 1126 limited the correlation of downhole logs to the sedimentary section. Except for the basal 25 m, photoelectric effect (PEF) values (averaging ~4 barn/e⁻) and the minimal neutron-density separations indicate calcium carbonate-rich sediments throughout the open-hole logged section. Porosity-density cross-overs and shallow resistivity peaks indicate the presence of many chert horizons. The succession was divided into six logging units on the basis of trends in the measured data sets. These units are described below.

Logging Unit 1: 0–41 mbsf (in Pipe)

This unit is characterized by relatively high gamma-ray values averaging 7 American Petroleum Institute (API) units measured through the pipe, with uranium contributing ~75% of the radioactivity (Fig. F27). Four gamma-ray cycles may be discerned in this unit, with maximum excursions ranging between 11 and 3 API units. The high levels of uranium indicate an increased abundance of organic matter and/or aragonite (see "Inorganic Geochemistry," p. 30). High gamma-ray values also appear to correlate with portions of the core with increased amounts of blackened grains. These grains may contain elevated uranium concentrations (see "Lithostratigraphy," p. 4). The base of Unit 1 is defined by an abrupt decrease in gamma-ray values, mainly caused by a decrease in uranium content (Fig. F27). Logging Unit 1 corresponds to PP Unit 1 and lithostratigraphic Subunit IA (see "Lithostratigraphy," p. 4, and "Physical Properties," p. 33). The base of logging Unit 1 correlates to the base of seismic Sequence 2 and to the Pliocene/Pleistocene boundary (see "Seismic Stratigraphy," p. 39).

Logging Unit 2: 41–167 mbsf (Partly in Pipe)

This unit was logged through pipe to 117 mbsf. The open-hole interval shows nearly constant values for all logs, with low gamma radiation

F27. Spectral gamma-ray logs from HNGS vs. depth, p. 77.

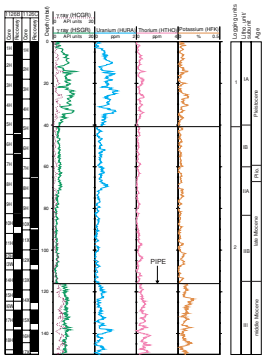

F28. Spectral gamma-ray logs vs. depth, p. 78.

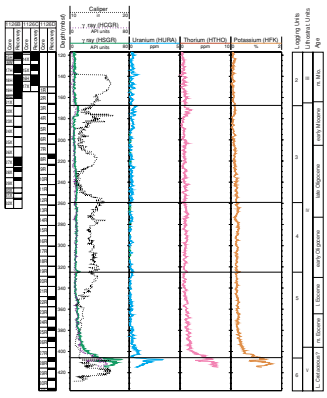

F29. Acoustic impedance vs. depth from density and sonic logs, p. 79.

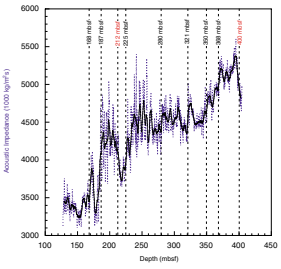

(6 API units), high porosity (70%), low sonic velocities (1.9 km/s), and PEF values of ~3.4 barn/e$^-$, all characteristic of a poorly lithified carbonate (Fig. F26). The base of logging Unit 2 corresponds to the base of seismic Sequence 3 and the base of PP Subunit 2B and is within 5 m of the base of lithostratigraphic Unit III (see "Lithostratigraphy," p. 4, "Seismic Stratigraphy," p. 39, and "Physical Properties," p. 33).

Logging Unit 3: 167–259 mbsf

Logging Unit 3 is characterized by a marked change to higher amplitude variations in porosity, density, and sonic velocity (Figs. F26, F28). There is a significant separation of shallow and deep resistivity curves within this unit, which indicates borehole fluid invasion into the formation (Fig. F26). Sonic velocity generally increases throughout Unit 3 from 2.1 to 2.4 km/s, whereas MS decreases from 380 to 320 ppm (Fig. F26). Low-porosity excursions that cross over the bulk-density curve correlate with peaks in the shallow-resistivity and sonic velocity logs and indicate the occurrence of lithified layers (Fig. F26). These features most likely correspond to chert horizons described from recovered sediments. The sonic log indicates that these harder layers are interbedded with much less indurated sediments, as confirmed by calcareous oozes recovered in the cores (see "Lithostratigraphy," p. 4).

Logging Unit 4: 259–325 mbsf

Logging Unit 4 is characterized by a gradual decrease in MS from 330 to 290 ppm and a linear increase in sonic velocity from 2.3 to 2.5 km/s over the same interval. Less-pronounced peaks in porosity and resistivity indicate the occurrence of probable chert bands near the top of Unit 4 (Fig. F26). At the base of Unit 4 there is a small peak in the otherwise uniform gamma-ray log coinciding with a marked low-porosity peak, a decrease in MS, and a small increase in resistivity, which likely indicates a hardground surface (Fig. F26).

Logging Unit 5: 325–406 mbsf

Within logging Unit 5 porosity decreases steadily from 60% to 55% and density increases from 1.9 to 2.1 g/cm^3 (Fig. F26). Sonic velocities increase to the base of the unit from 2.4 to 2.7 km/s and MS decreases from 300 to 220 ppm. Convergence of porosity and density logs downhole in this unit indicate an increasingly pure limestone toward the base. This finding is supported by the decrease in MS (Fig. F26).

Below 390 m in Unit 5, gamma-ray values increase from ~10 to 35 API units (Fig. F26). This increase is dominated by Th and K, indicating greater amounts of clay in this interval (Fig. F28). This conclusion is supported by the increase in MS from 220 to 1300 ppm at the logging Unit 5/Unit 6 boundary (Fig. F26). Throughout Unit 5 there is a downhole increase in resistivity with a peak at the base of the unit. Sonic velocity is constant at ~2.6 km/s (Fig. F26). A velocity inversion (from ~2.2 to 1.75 km/s) is seen in the sonic log at the base of the unit, although this may be an artifact of an increased borehole diameter (Fig. F26). The base of logging Unit 5 correlates with the base of lithostratigraphic Unit IV, PP Unit 4 (see "Lithostratigraphy," p. 4 and "Physical Properties," p. 33), and the hiatus between Cretaceous siliciclastic deposits and Tertiary carbonates (see "Biostratigraphy," p. 12).

Logging Unit 6: 406–437 mbsf

The top of logging Unit 6 is marked by significant inflections in all logs, especially MS (300 to 1300 ppm) and gamma radiation (30 and 70 API units) (Figs. F26, F28). A high gamma-ray signal results from significant contributions of Th and K (Fig. F28). Within Unit 6 the caliper indicates major washouts and caving. The PEF values in Unit 6 are highly variable with generally lower values being characteristic of siliciclastic sediments (2–3 barn/e$^-$) and higher values indicating the presence of iron minerals (Fig. F26). This conclusion is supported by corresponding peaks in MS approaching 1500 ppm (Fig. F26).

Acoustic Impedance

Acoustic impedance was calculated using downhole velocity and density data in the following equation:

$$I = V_p \times p,$$

where V_p = sonic velocity (m/s) and p = bulk density (kg/m^3) (Fig. F29). After calculating impedance, data were smoothed using a 20-point running average, which gave an ~3-m resolution. This resolution is 2–3 times higher than the resolution of the site-survey seismic data (see "Seismic Stratigraphy," p. 39). Numerous peaks in impedance are observed with the most prominent at 168, 187, 225, and 350 mbsf (Fig. F29). An impedance peak at 168 mbsf correlates well with the base of seismic Sequence 3 (see "Seismic Stratigraphy," p. 39) and the base of logging Unit 2, whereas the peak at 225 mbsf correlates with the top of seismic Sequence 6A.

SEISMIC STRATIGRAPHY

Introduction

Drilling at Site 1126 penetrated Cenozoic seismic Sequences 2, 3, 4, and 6A (sequences defined in Feary and James, 1998, reprinted as Chap. 2) and bottomed in Cretaceous siliciclastic sediments. A direct seismic tie to Jerboa-1 23.4 nmi to the west (Fig. F30) indicates that these Cretaceous sediments are of Cenomanian age. It is possible that a thin interval of Sequence 7 sandstones may also be present below seismic resolution. The high-resolution site-survey seismic data (Fig. F31), together with the regional seismic database, indicate that significant hiatuses should occur at all sequence boundaries and also at intrasequence horizons within Sequences 3 and 6A.

Time–Depth Conversion

A check-shot survey using the single-channel WST was undertaken at this site to establish the time–depth relationship within the Cenozoic succession and to assess the degree to which stacking velocities (derived from high-resolution site-survey seismic data for common depth points adjacent to sites) could be used for preliminary depth estimates. The parameters and procedures undertaken during the check-shot survey at Site 1126 are described in "Downhole Measurements," p. 35. The nine time–depth tie points derived from the check-shot survey are presented

F30. Seismic site-survey tracks for Site 1126 in relation to other Leg 182 sites and the AGSO169 site-survey seismic lines, p. 80.

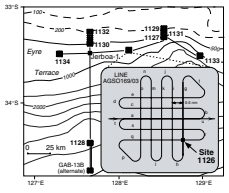

F31. Portion of seismic Line AGSO169/03g showing seismic stratigraphic sequences, p. 81.

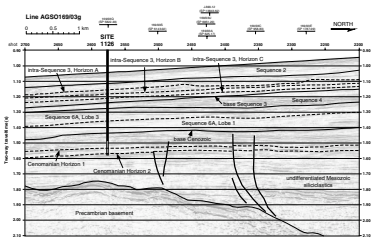

in Figure F32. These points were plotted on a depth to two-way–traveltime graph (Fig. F33A) to (1) show the relationship between depths encountered at Site 1126 and sequence boundaries and horizons located on seismic data and (2) compare the check shot–corrected time–depth relationship to predictions based on stacking velocities. This plot shows that the actual time–depth relationship defined by the check-shot survey falls at the lower limit of the envelope defined by the six stacking velocity curves from the immediate vicinity of Site 1126, with a relatively small difference (≤17 m) between predicted and actual depths to boundaries/horizons (Table T19). The relatively poor match between check-shot data and the velocity log (Fig. F33B) is possibly a response to poor contact between the sonic tool and borehole wall. The integrated sonic trace (Fig. F33) derived from interval transit-time data is in excellent agreement with stacking velocities, although it required check-shot data to anchor the uppermost point.

Seismic Sequence Characteristics

The data collected at Site 1126 allow a description of the characteristics of the seismic sequences intersected at this site (see "Lithostratigraphy," p. 4, and "Biostratigraphy," p. 12). Downhole data were correlated with seismic stratigraphy (Fig. F34) based on the regional moderate-resolution multichannel seismic data collected by the Japan National Oil Corporation (JNOC) in 1990 (Feary and James, 1998, reprinted as Chap. 2) and the high-resolution site-survey seismic data collected by the Australian Geological Survey Organisation (AGSO) in 1996 (Feary, 1997).

Sequence 2

Regional seismic data indicate that the thickness of Sequence 2 varies greatly, from a maximum of >500 m through the spectacular sigmoidal clinoforms beneath the modern shelf edge and uppermost slope (see "Seismic Stratigraphy," p. 26, in the "Site 1127" chapter) thinning to <100 m landward beneath the outer shelf and seaward down the upper and middle slope. Sequence 2 is relatively thin (60 m) at Site 1126, with seismic data indicating that the basal sequence boundary is a marked unconformity/hiatus surface containing erosional channels cut down into the underlying Sequence 3 interval. Reflections within Sequence 2 are evenly stratified and conformable. This sequence correlates with the bioturbated nannofossil and foraminifer ooze of lithostratigraphic Unit I, and biostratigraphic datums indicate a Pleistocene age.

Sequence 3

From a regional perspective, Sequence 3 is thickest (~240 m) beneath the modern shelf and thins downslope to a feather edge beneath the modern middle shelf. Site 1126 intersects Sequence 3 beneath the upper slope where it is 105 m thick. The high-resolution site-survey seismic data show that Sequence 3 includes one definite unconformity/hiatus surface displaying significant erosional downcutting (Fig. F31, Horizon A) and two other prominent horizons that may represent hiatuses (Fig. F31, Horizons B and C). Lithostratigraphic Subunit IIA (of latest Miocene–Pliocene age) correlates with the sub-sequence above Horizon A, the upper Miocene Subunit IIB correlates with the sub-sequence between Horizons A and B, and the middle Miocene Unit III correlates with the sub-sequence underlying Horizon B (Fig. F34). No lithostrati-

F32. Check-shot stations and acquisition geometry for the WST survey, p. 82.

Depth (mbrf)	Depth (mbsl)	Transit time (ms)	True path length (m)	Corrected TWT (ms)	Interval velocity (ms)
913.90	902.7	594.30	912.27	1190.72	2099.17
957.10	945.9	614.85	955.41	1231.88	2184.60
1024.80	1013.6	645.80	1023.02	1293.84	2188.06
1064.80	1053.6	664.06	1062.98	1330.40	2411.23
1108.90	1097.7	682.33	1107.03	1366.97	2367.74
1134.90	1123.7	693.30	1133.00	1388.92	2359.95
1158.90	1147.7	703.46	1156.98	1409.25	2641.48
1188.30	1177.1	714.58	1186.35	1431.50	1793.59
1203.90	1192.7	723.27	1201.94	1448.90	

Corrected TWT is TWT from sea level to WST tool along a vertical path

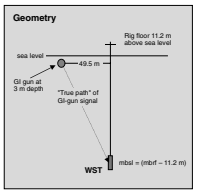

F33. Predicted and corrected depths and interval velocities, p. 83.

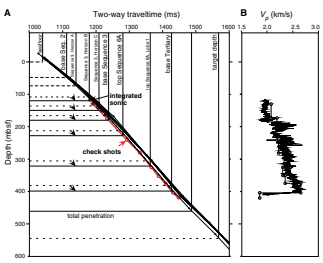

T19. Differences between depths to key horizons and corrected depths, p. 110.

F34. Lithostratigraphic units, seismic sequences, biostratigraphic hiatuses, and ages, p. 84.

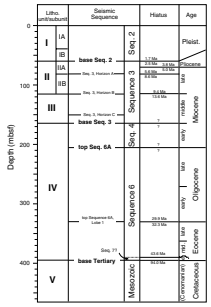

graphic break is recognized that coincides with Horizon C within the middle Miocene.

Lithostratigraphic data indicate that the Pliocene sequence (above Horizon A) consists of bioturbated, white-gray nannofossil ooze wackestones and light gray nannofossil ooze packstones, with two slumped intervals. The erosional unconformity at the top of the upper Miocene sequence (between Horizons A and B) is marked by a firmground. The sub-sequence between Horizons A and B consists of bioturbated calcareous nannofossil ooze interbedded with irregular to nodular chert/porcellanite layers corresponding to Subunit IIB. The middle Miocene Unit III, which forms the remainder of Sequence 3 (below Horizon B) consists of bioturbated calcareous nannofossil ooze with wackestone to mudstone texture, together with interbedded silicified layers.

Sequence 4

Within the Eucla Basin seismic Sequence 4 is a relatively thin, aggradational unit characterized by conformable internal reflections (Feary and James, 1998). This sequence is only 41 m thick at Site 1126, corresponding to the uppermost portion of lithostratigraphic Unit IV. Biostratigraphic data indicate an early Miocene age. Because of limited recovery, it is difficult to fully describe the lithologic characteristics of this sequence. Available data indicate that it consists of a diverse array of rock types dominated by pervasively bioturbated chalks and oozes, together with interbeds of silicified calcareous pelagic limestone and porcellanite/chert. The upper sequence boundary is a bioclastic packstone containing planktonic and benthic foraminifers, ostracodes, and echinoderm debris.

Sequence 6A

Sites 1126 and 1134 offered the only opportunities during this leg to characterize the lithology and age of seismic Sequence 6A, shown on regional seismic data to consist of three deep-water sediment lobes derived from the north (Feary and James, 1998). The 190-m section through Sequence 6A intersected at Site 1126 was first encountered at 206 mbsf. Despite their differences in overall seismic geometry, Sequence 6A consists of a diverse lithologic suite essentially identical to that encountered in Sequence 4, to the extent that these units are grouped into the single lithostratigraphic Unit IV. Biostratigraphic data indicate that this sequence ranges from the middle Eocene through to the late Oligocene. Although expected to occur as a hiatus surface representing the Eocene/Oligocene boundary, no apparent break was detected coinciding with the boundary between the Eocene Lobe 1 (oldest) and Oligocene Lobe 3 (youngest) at ~330 mbsf (Fig. **F31**). However, postcruise work may clarify the detailed biostratigraphy within this poorly recovered section.

Sequence 7

A thin interval of brown quartz sandstones (Core 182-1126D-27R-CC) occurs between the middle Eocene nannofossil-foraminifer chalk of Sequence 6A and the dark greenish black to black sandstones of presumed Cretaceous age (see **"Cretaceous Sequence,"** p. 42). Available data indicate that these brown sandstones are probably of middle Eocene age (P12; see **"Biostratigraphy,"** p. 12), although the sample for

age dating was taken from the very top of the sandstone and may represent contamination from the overlying Sequence 6A chalks. One core fragment contains an irregular coating of calcareous sandstone, inferred to represent a cavity infill, that contains sparse bioclasts among the predominantly quartz grain clastic component. We suggest that either this cavity infill or both cavity infill and brown sandstone be tentatively assigned to Sequence 7 and speculate that irregular thicknesses of Sequence 7 sandstones may have infilled depressions and irregularities in the eroded Cretaceous surface.

Cretaceous Sequence

The base of the Cenozoic section throughout the Eucla Basin is a dramatic angular erosional unconformity corresponding to a hiatus of some 50 m.y. (Fig. **F34**). At Site 1126 this unconformity is present as a boundary between overlying middle Eocene facies and the underlying 60-m succession of black to green siltstone, sandstone, and granule conglomerate lithologies, inferred to be of Cenomanian age on the basis of the direct seismic tie to exploration well Jerboa-1.

REFERENCES

Bein, J., and Taylor, M.L., 1981. The Eyre Sub-basin: recent exploration results. *APEA J.,* 21:91–98.

Berggren, W.A., Hilgen, F.J., Langereis, C.G., Kent, D.V., Obradovich, J.D., Raffi, I., Raymo, M.E., and Shackleton, N.J., 1995a. Late Neogene chronology: new perspectives in high-resolution stratigraphy. *Geol. Soc. Am. Bull.,* 107:1272–1287.

Berggren, W.A., Kent, D.V., Swisher, C.C., III, and Aubry, M.-P., 1995b. A revised Cenozoic geochronology and chronostratigraphy. *In* Berggren, W.A., Kent, D.V., Aubry, M.-P., and Hardenbol, J. (Eds.), *Geochronology, Time Scales and Global Stratigraphic Correlation*. Spec. Publ.—Soc. Econ. Paleontol. Mineral., 54:129–212.

Berggren, W.A., and Miller, K.G., 1988. Paleogene tropical planktonic foraminiferal biostratigraphy and magnetobiochronology. *Micropaleontology,* 34:362–380.

Blow, W.H., 1969. Late middle Eocene to Recent planktonic foraminiferal biostratigraphy. *In* Brönnimann, P., and Renz, H.H. (Eds.), *Proc. First Int. Conf. Planktonic Microfossils, Geneva, 1967:* Leiden (E.J. Brill), 1:199–422.

Boyce, R.E., 1976. Definitions and laboratory techniques of compressional sound velocity parameters and wet-water content, wet-bulk density, and porosity parameters by gravimetric and gamma-ray attenuation techniques. *In* Schlanger, S.O., Jackson, E.D., et al., *Init. Repts. DSDP,* 33: Washington (U.S. Govt. Printing Office), 931–958.

Chaproniere, G.C.H., Shafik, S., Truswell, E.M., MacPhail, M.K., and Partridge, A.D., 1995. Cainozoic. In *Australian Phanerozoic Time Scale.* Aust. Geol. Surv. Org., 10.

Cisowski, S., 1981. Interacting vs. non-interacting single domain behavior in natural and synthetic samples. *Phys. Earth Planet. Inter.,* 26:56–62.

Couture, R., Miller, R.S., and Gieskes, J.M., 1978. Interstitial water and mineralogical studies, Leg 41. *In* Lancelot, Y., Seibold, E., et al., *Init. Repts. DSDP,* 41: Washington (U.S. Govt. Printing Office), 907–914.

Eberli, G.P., Swart, P.K., Malone, M.J., et al., 1997. *Proc. ODP, Init. Repts.,* 166: College Station, TX (Ocean Drilling Program).

Feary, D.A., 1997. ODP pollution prevention and safety panel: Leg 182 safety package—Cenozoic cool-water carbonates of the Great Australian Bight. *Aust. Geol. Surv. Org.,* 28.

Feary, D.A., and James, N.P., 1998. Seismic stratigraphy and geological evolution of the Cenozoic, cool-water, Eucla Platform, Great Australian Bight. *AAPG Bull.,* 82:792–816.

Gieskes, J.M., 1981. Deep-sea drilling interstitial water studies: implications for chemical alteration of the oceanic crust, layers I and II. *In* Warme, J.E., Douglas, R.G., and Winterer, E.L. (Eds.), *The Deep Sea Drilling Project: A Decade of Progress*. Spec. Publ.—Soc. Econ. Paleontol. Mineral., 32:149–167.

————, 1983. The chemistry of interstitial waters of deep-sea sediments: interpretation of deep-sea drilling data. *In* Riley, J.P., and Chester, R. (Eds.), *Chemical Oceanography* (Vol. 8): London (Academic), 221–269.

James, N.P., and Bone, Y., 1991. Origin of a cool-water, Oligo-Miocene deep shelf limestone, Eucla Platform, southern Australia. *Sedimentology,* 38:323–341.

Jenkins, D.G., 1985. Southern mid-latitude Paleocene to Holocene planktic foraminifera. *In* Bolli, H.M., Saunders, J.B., and Perch-Nielsen, K. (Eds.), *Plankton Stratigraphy:* Cambridge (Cambridge Univ. Press), 263–282.

————, 1993. Cenozoic Southern mid- and high-latitude biostratigraphy and chronostratigraphy based on planktonic foraminifera. *In* Kennett, J.P., and Warnke, D.A. (Eds.), *The Antarctic Paleoenvironment: A Perspective on Global Change*. Antarct. Res. Ser., 60:125–144.

Kastner, M., Elderfield, H., Martin, J.B., Suess, E., Kvenvolden, K.A., and Garrison, R.E., 1990. Diagenesis and interstitial-water chemistry at the Peruvian continental margin—major constituents and strontium isotopes. *In* Suess, E., von Huene, R., et

al., *Proc. ODP, Sci. Results,* 112: College Station, TX (Ocean Drilling Program), 413–440.

Katz, M.E., and Miller, K.G., 1991. Early Paleogene benthic foraminiferal assemblages and stable isotopes in the Southern Ocean. *In* Ciesielski, P.F., Kristoffersen, Y., et al., *Proc. ODP, Sci. Results,* 114: College Station, TX (Ocean Drilling Program), 481–512.

Loughnan, F.C., 1969. *Chemical Weathering of Siliciclastic Minerals:* New York (Elsevier).

Mackensen, A., 1992. Neogene benthic foraminifers from the southern Indian Ocean (Kerguelen Plateau): biostratigraphy and paleoecology. *In* Wise, S.W., Jr., Schlich, R., et al., *Proc. ODP, Sci. Results,* 120: College Station, TX (Ocean Drilling Program), 649–673.

Mackensen, A., and Berggren, W.A., 1992. Paleogene benthic foraminifers from the southern Indian Ocean (Kerguelen Plateau): biostratigraphy and paleoecology. *In* Wise, S.W., Jr., Schlich, R., et al., *Proc. ODP, Sci. Results,* 120: College Station, TX (Ocean Drilling Program), 603–630.

McGowran, B., Li, Q., and Moss, G., 1997. The Cenozoic neritic record in southern Australia: the biogeohistorical framework. *In* James, N.P., and Clarke, J., *Cool-Water Carbonates*. Spec. Publ.— Soc. Econ. Petrol. Mineral., 56:185–203.

Miller, K.G., and Katz, M.E., 1987. Oligocene to Miocene benthic foraminiferal and abyssal circulation changes in the North Atlantic. *Micropaleontology,* 33:97–149.

Mullins, C.C., and Tite, M.S., 1973. Magnetic viscosity quadrature susceptibility, and frequency dependence of susceptibility in single domain assemblages of magnetite and maghaemite. *J. Geophys. Res.,* 78:804–809.

Nagata, T., Kobayashi, K., and Fuller, M., 1964. Identification of magnetite and hematite in rocks by observation at low temperature. *J. Geophys. Res.,* 6:2111–2120.

Raymo, M.E., Ruddiman, W.F., Backman, J., Clement, B.M., and Martinson, D.G., 1989. Late Pliocene variation in Northern Hemisphere ice sheets and North Atlantic deep water circulation. *Paleoceanography,* 4:413–446.

Rider, M., 1996. *The Geological Interpretation of Well Logs* (2nd ed.): Caithness (Whittles Publishing).

Shackleton, N.J., Berger, A., and Peltier, W.A., 1990. An alternative astronomical calibration of the lower Pleistocene timescale based on ODP Site 677. *Trans. R. Soc. Edinburgh: Earth Sci.,* 81:251–261.

Shackleton, N.J., Crowhurst, S., Hagelberg, T., Pisias, N.G., and Schneider, D.A., 1995. A new late Neogene time scale: application to Leg 138 sites. *In* Pisias, N.G., Mayer, L.A., Janecek, T.R., Palmer-Julson, A., and van Andel, T.H. (Eds.), *Proc. ODP, Sci. Results,* 138: College Station, TX (Ocean Drilling Program), 73–101.

Shafik, S., 1983. Calcareous nannofossil biostratigraphy: an assessment of foraminiferal and sedimentation events in the Eocene of the Otway Basin, southeastern Australia. *BMR J. Aust. Geol. Geophys.,* 8:1–17.

————, 1990. The Maastrichtian and early Tertiary record of the Great Australian Bight Basin and its onshore equivalents on the Australian southern margin: a nannofossil study. *BMR J. Australian Geol. Geophys.,* 11:473–497.

Sotelo, V., and Gieskes, J.M., 1978. Interstitial water studies, Leg 40: shipboard results. *In* Bolli, H.M., Ryan, W.B.F., et al., *Init. Repts. DSDP,* 40: Washington (U.S. Govt. Printing Office), 549–551.

Suess, E., von Huene, R., et al., 1988. *Proc. ODP, Init. Repts.,* 112: College Station, TX (Ocean Drilling Program).

Swart, P.K., and Guzikowski, M., 1988. Interstitial-water chemistry and diagenesis of periplatform sediments from the Bahamas, ODP Leg 101. *In* Austin, J.A., Jr., Schlager, W., Palmer, A.A., et al., *Proc. ODP, Sci. Results,* 101: College Station, TX (Ocean Drilling Program), 363–380.

Thomas, E., 1990. Late Cretaceous through Neogene deep-sea benthic foraminifers (Maud Rise, Weddell Sea, Antarctica). *In* Barker, P.F., Kennett, J.P., et al., *Proc. ODP, Sci. Results,* 113: College Station, TX (Ocean Drilling Program), 571–594.

Tjalsma, R.C., and Lohmann, G.P., 1983. Paleocene-Eocene bathyal and abyssal benthic foraminifera from the Atlantic Ocean. *Micropaleontol. Spec. Publ.,* 4.

Toumarkine, M., and Luterbacher, H., 1985. Paleocene and Eocene planktic foraminifera. *In* Bolli, H.M., Saunders, J.B., and Perch-Nielsen, K. (Eds.), *Plankton Stratigraphy:* Cambridge (Cambridge Univ. Press), 87–154.

van Morkhoven, F.P.C.M., Berggren, W.A., and Edwards, A.S., 1986. Cenozoic cosmopolitan deep-water benthic foraminifera. *Bull. Cent. Rech. Explor.—Prod. Elf-Aquitaine,* Mem. 11.

Figure F1. Map showing the location of Site 1126 (on the eastern end of the Eyre Terrace) in relation to other Leg 182 sites and the Australian Geological Survey Organisation Survey 169 (AGSO169) site-survey seismic lines.

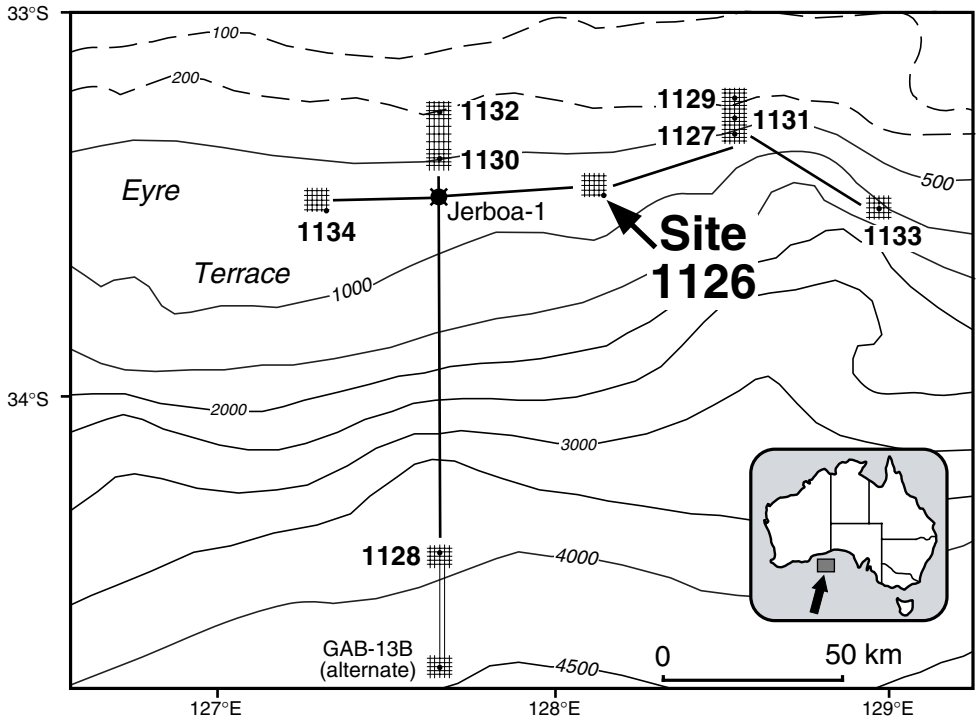

Figure F2. Portion of seismic Line AGSO169/03g showing interpreted seismic stratigraphic sequences planned (shown in white) and actually intersected (shown in black) at Site 1126.

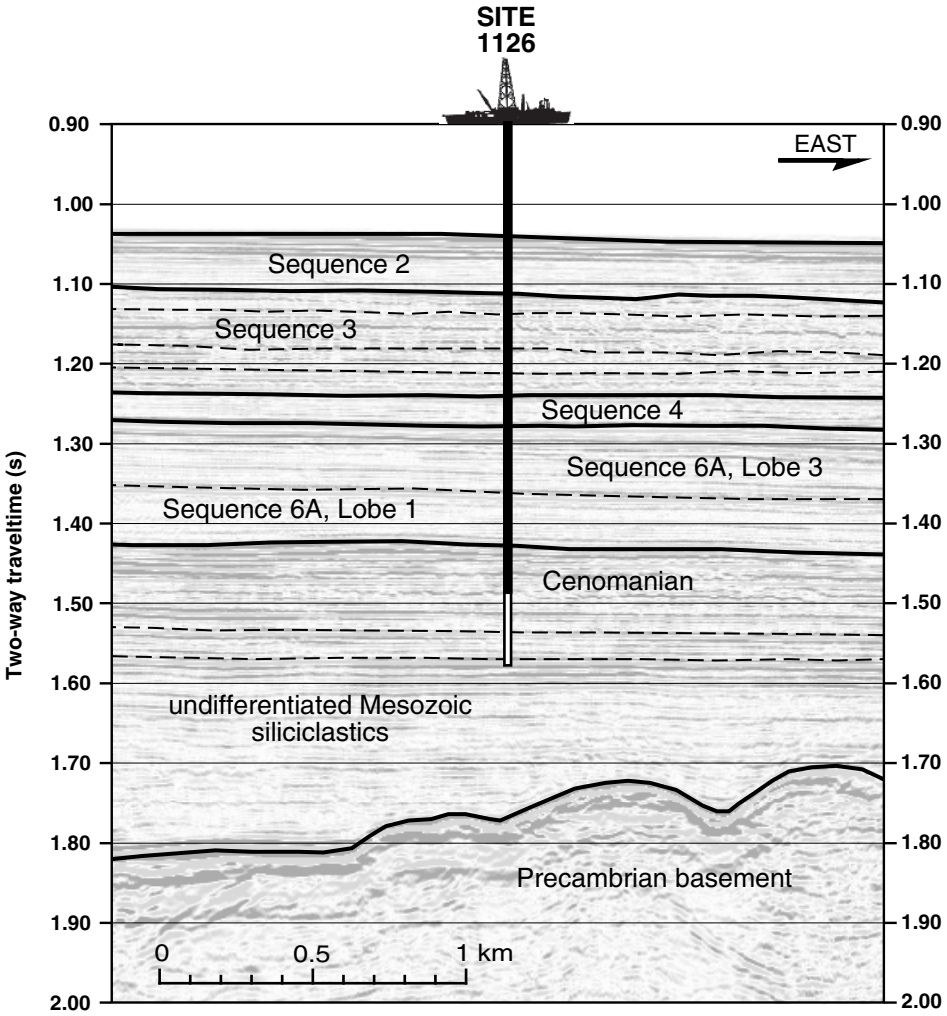

Figure F3. Summary of sediments and lithostratigraphy at Site 1126. Note that a further subdivision of Unit IV was not possible as a result of poor core recovery. Symbols in the lithostratigraphic column indicate the most abundant sedimentary particles. (Continued on next page.)

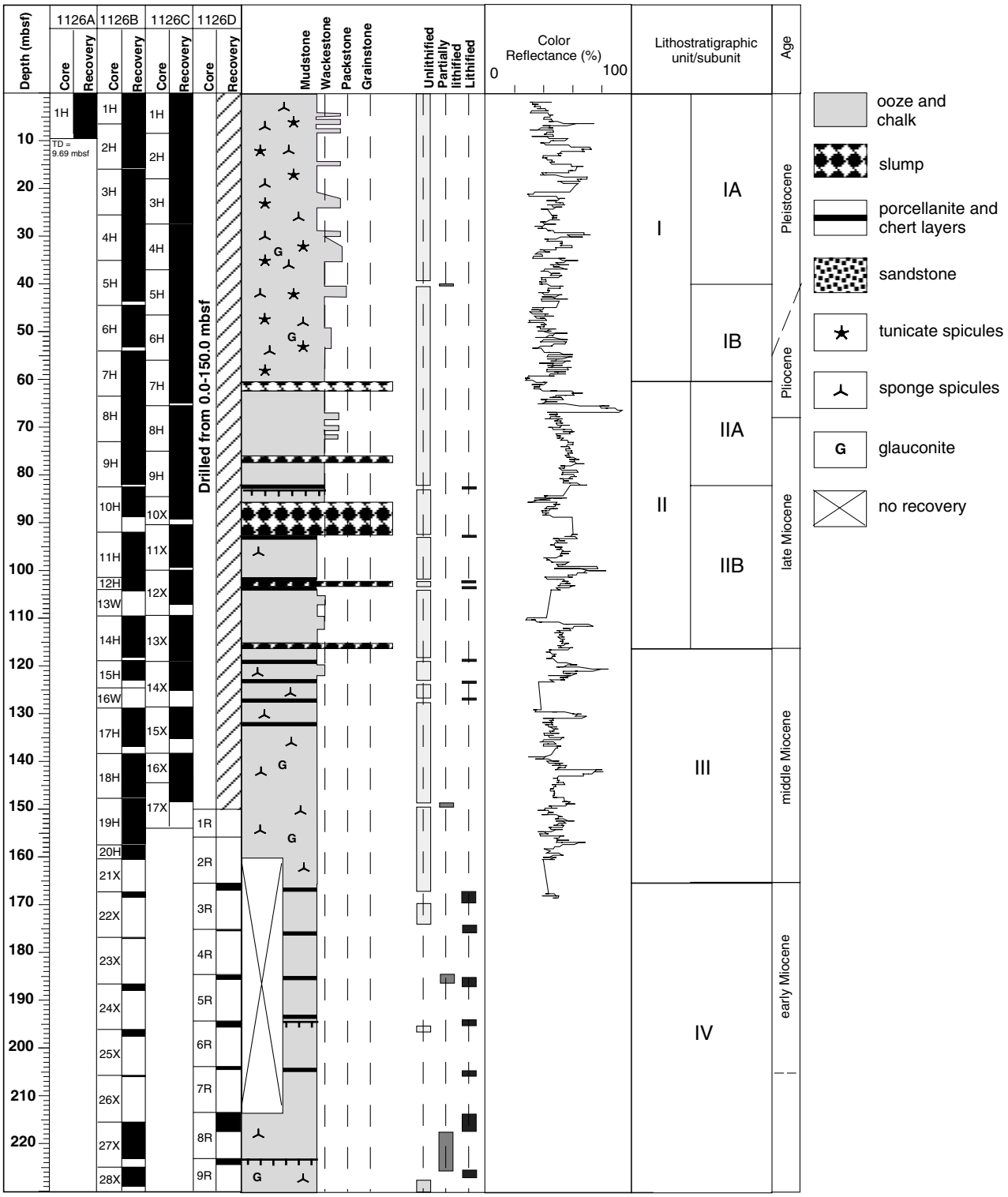

Figure F3 (continued).

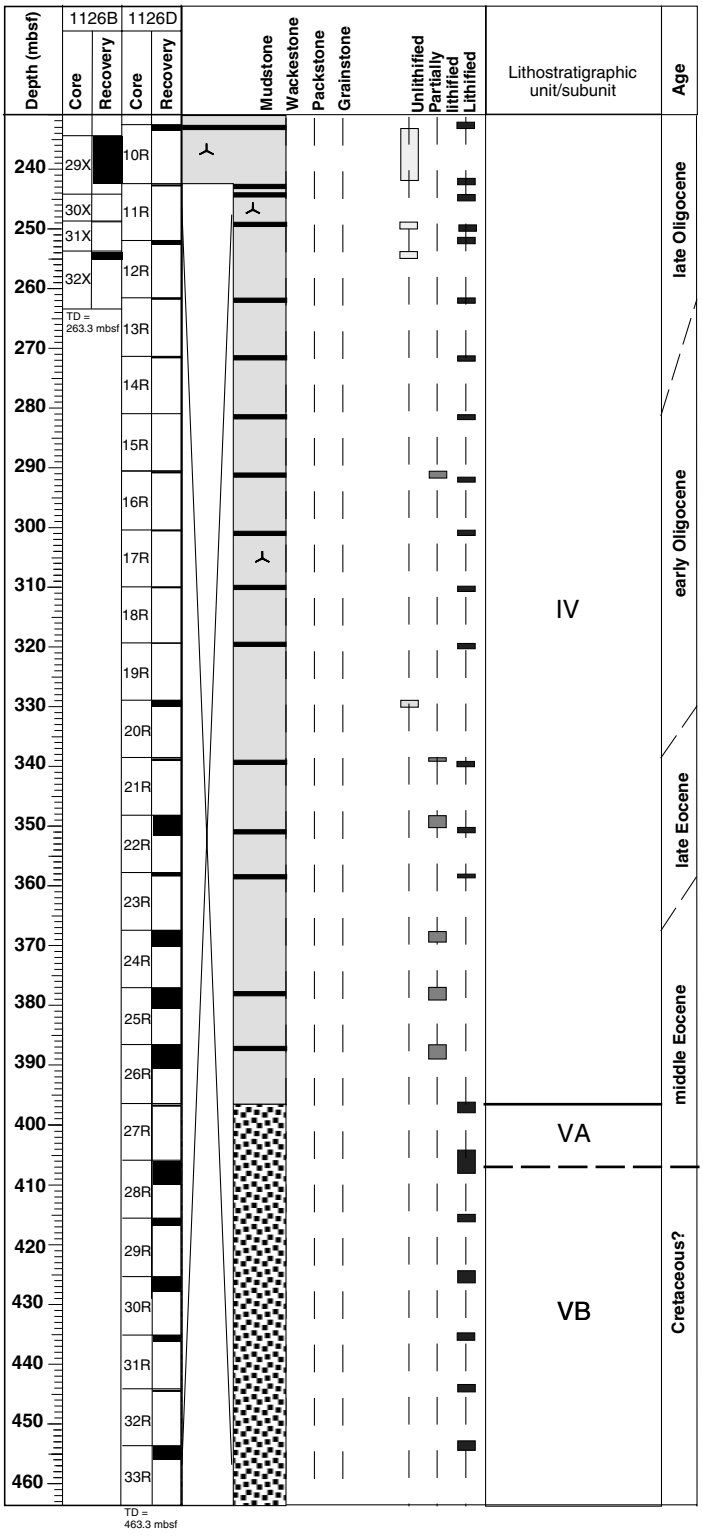

Figure F4. Solitary azooxanthellate coral in Section 182-1126B-5H-5, 140 cm.

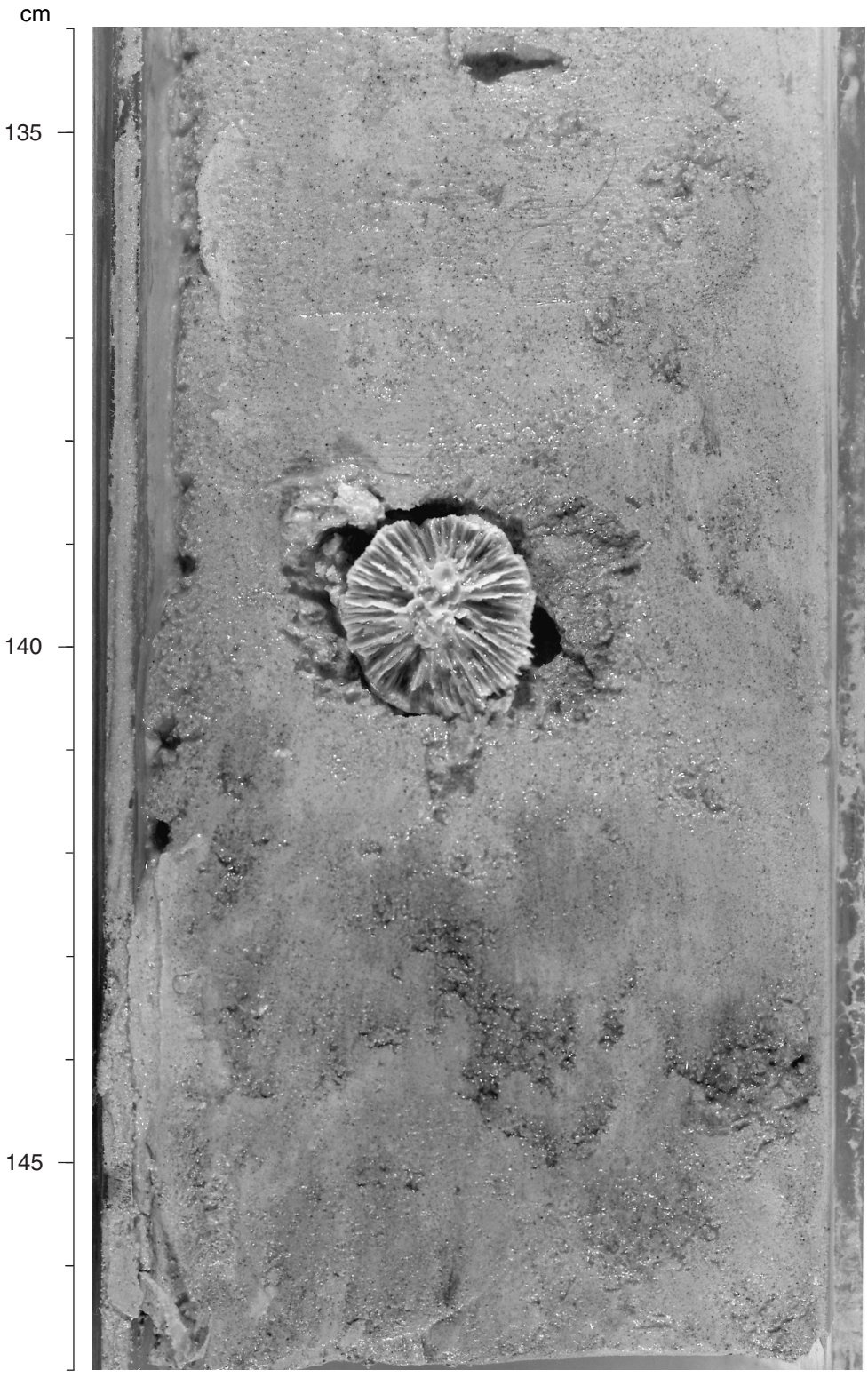

Figure F5. Inclined, deformed beds in Section 182-1126B-9H-3. This soft sediment deformation is interpreted as a slump deposit.

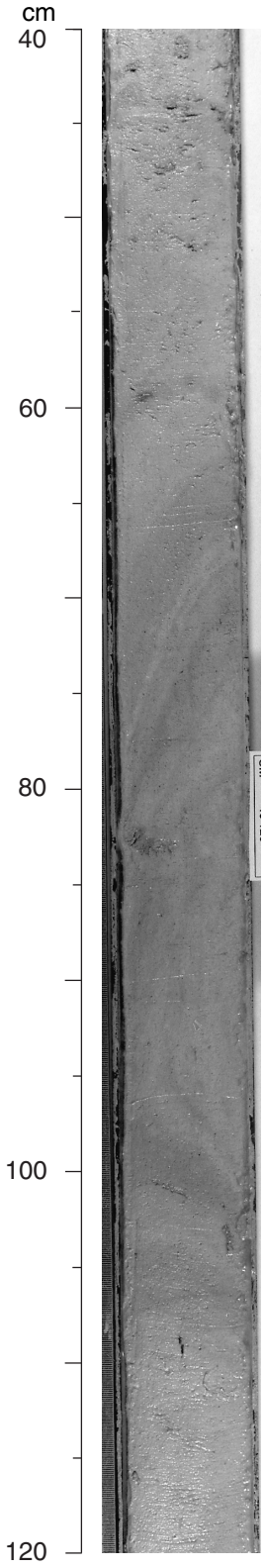

Figure F6. Stratigraphic position of calcareous nannofossil and planktonic foraminifer zones with benthic foraminifer assemblages at Site 1126. Dashed boundaries imply uncertainty. No sample means that the core catcher, if recovered, did not contain enough sediment to prepare for foraminifers. No recovery means that no material was recovered in a core. (Continued on next page.)

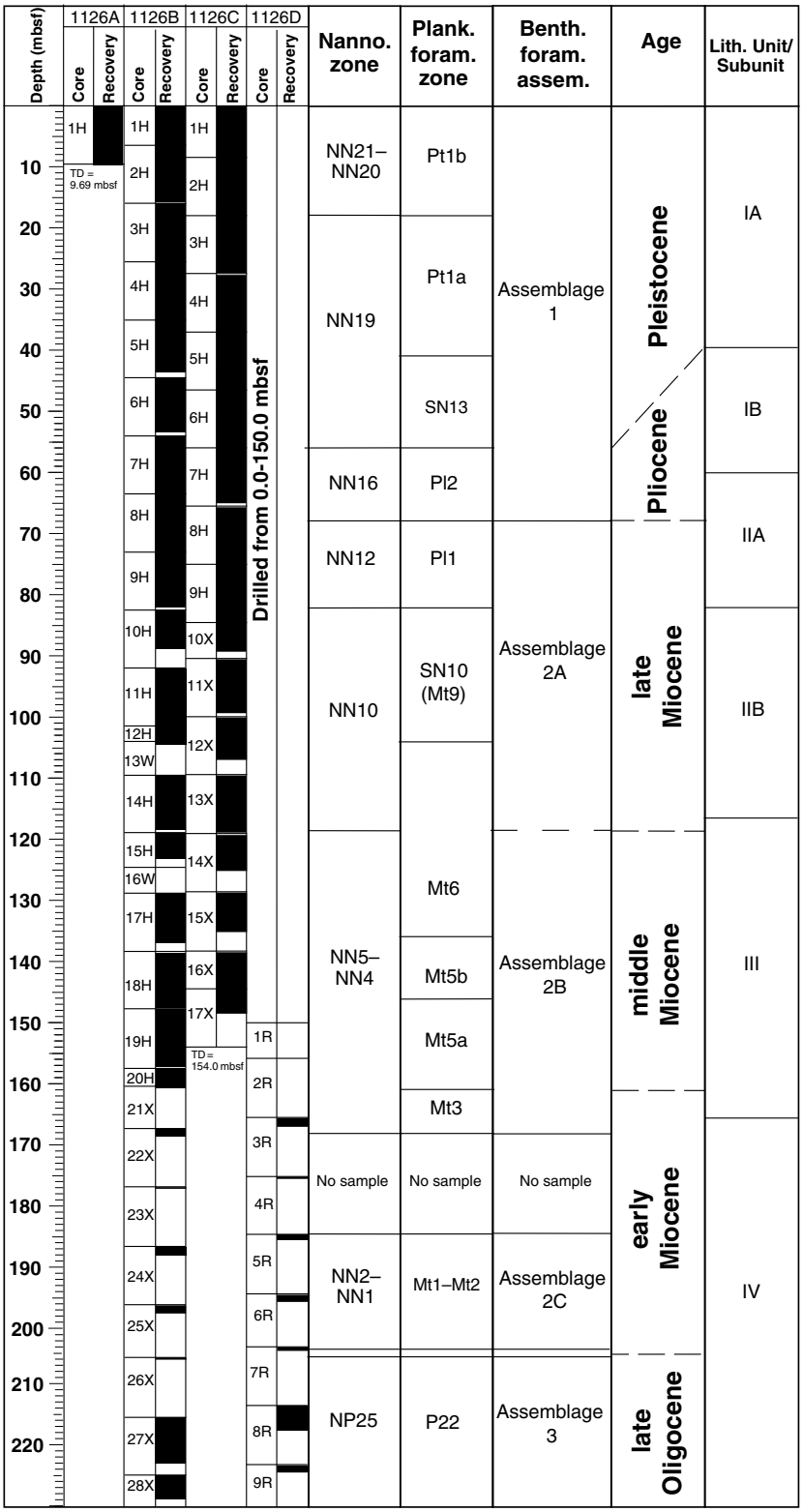

Figure F6 (continued).

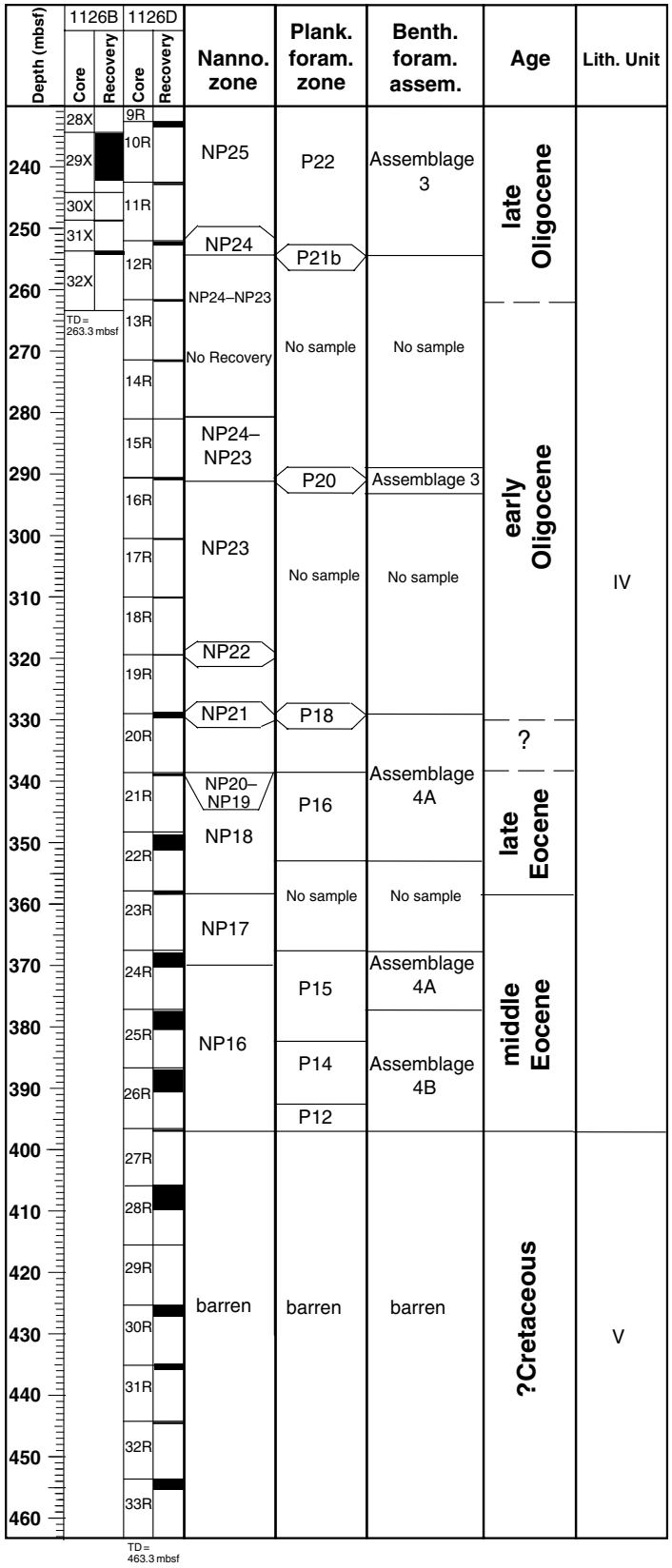

Figure F7. Sedimentation rate curve constructed from the datum levels listed in Table T2, p. 88. Stratigraphic error varies from ±0.16 to ±9.83 m, as indicated by the length of the error bars. Datum levels are coded from 1 to 27 and named in Table T2, p. 88.

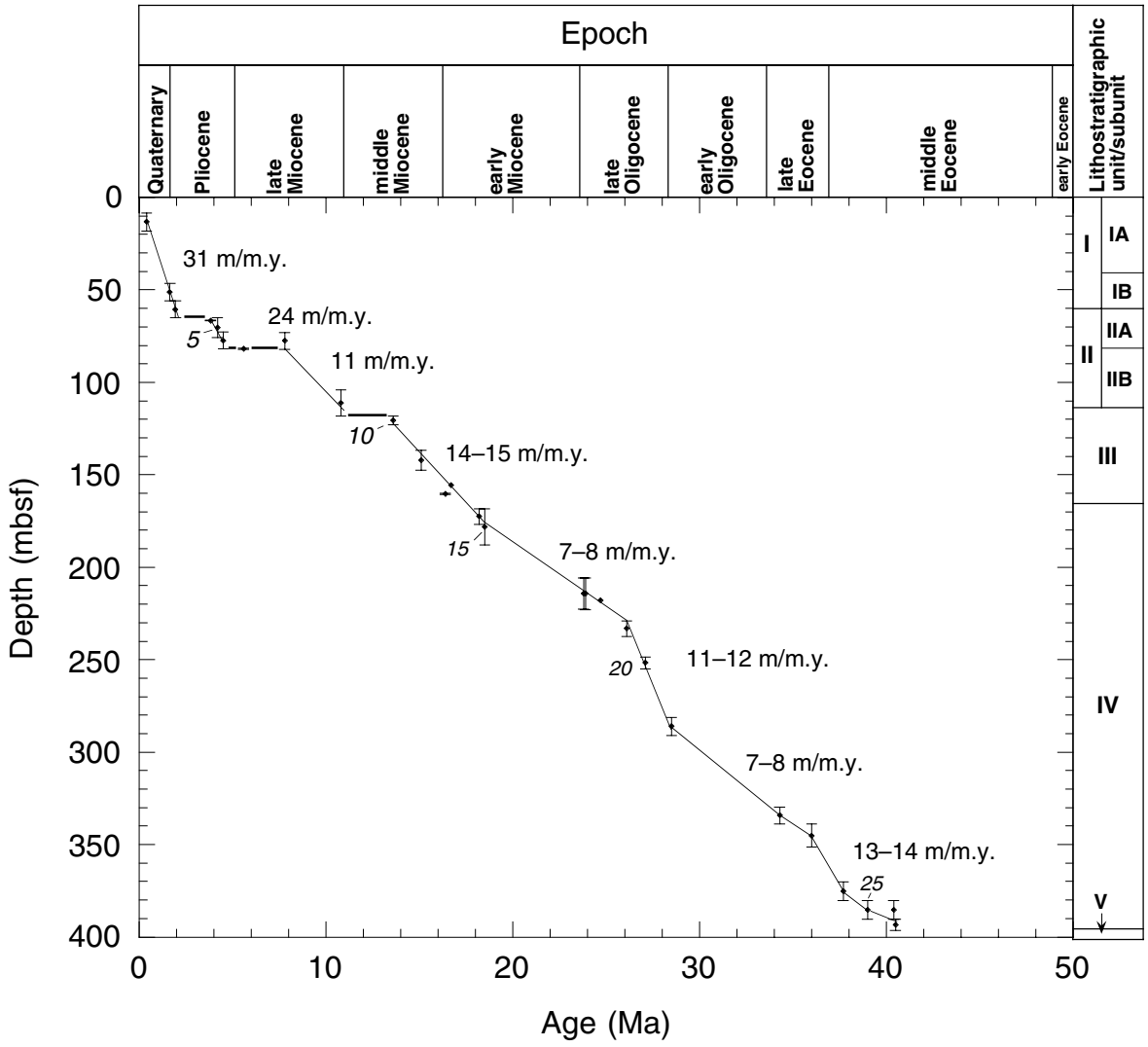

Figure F8. Inclination measurements from Core 182-1126B-19H as a whole core (open symbols) and as an archive-half core (closed symbols), demonstrating a similar record of reversals.

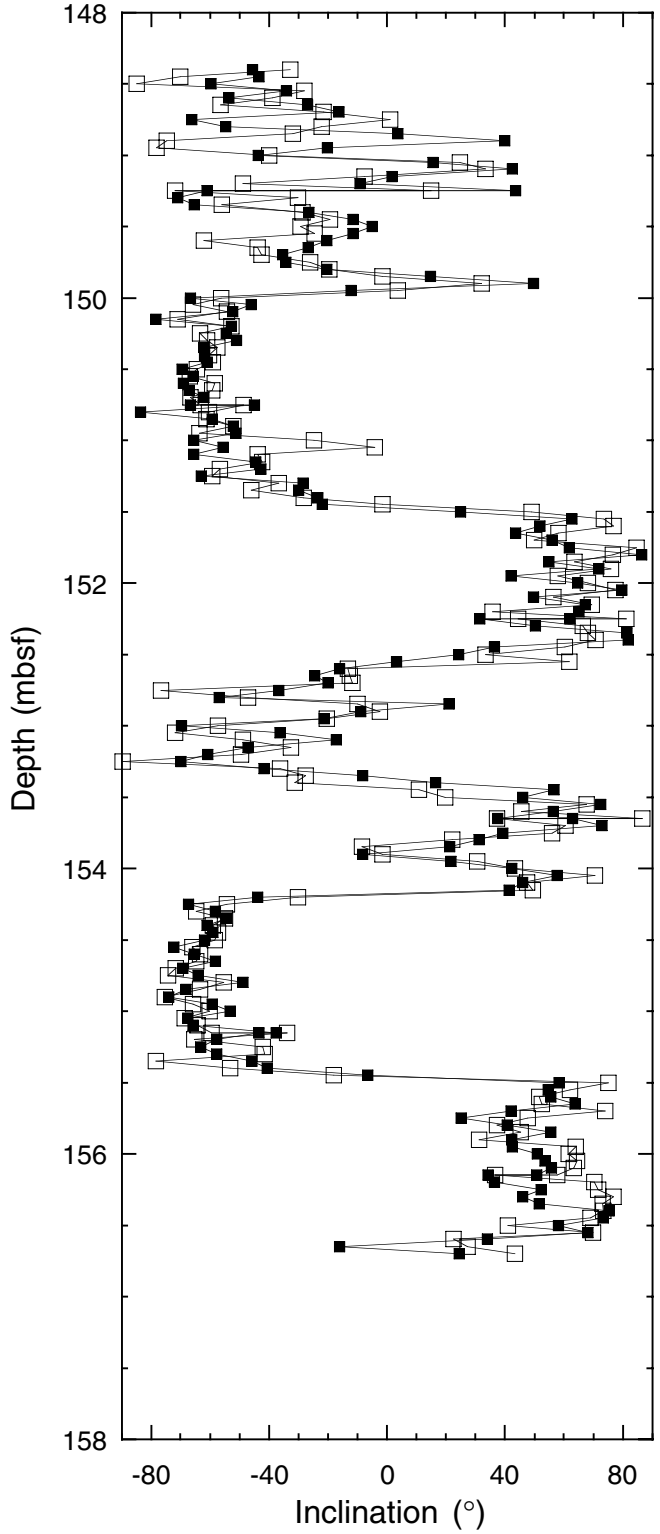

Figure F9. AF demagnetization behavior of Sample 182-1126D-33X, 87–89 cm. **A.** Intensity of magnetization plotted vs. demagnetization. **B.** Component diagram showing demagnetization north and east components with solid symbols and north and up components with open symbols. The first point and those selected for principal component analysis are shown with enlarged symbols. **C.** Equal-area plot of directions of magnetization during demagnetization. Demagnetization first removes a downward, steeply inclined magnetization that brings the direction of magnetization to the main group in C and is expressed as an increase in net magnetization in A and B. Then demagnetization reveals the characteristic magnetization that is determined by principal component analysis to be declination = 100.3° and inclination = –60.1° with a maximum angular deviation angle of 3°.

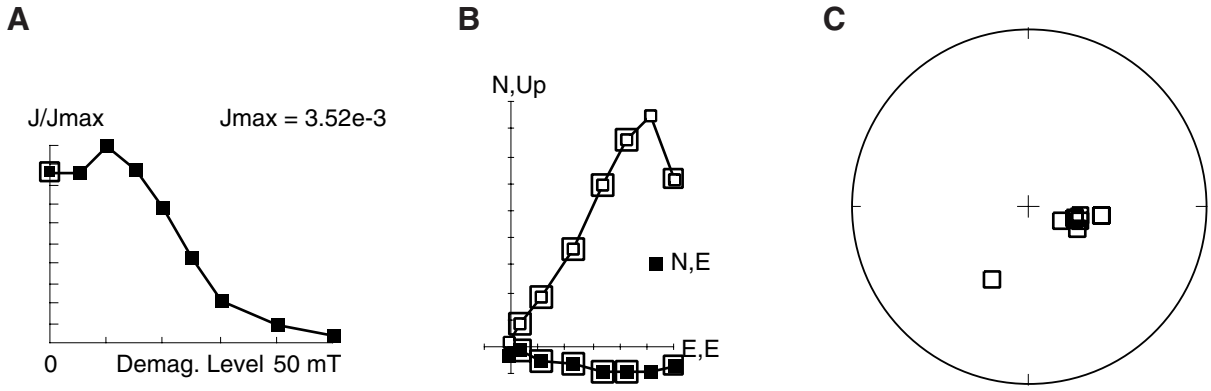

Figure F10. Plots of demagnetization of natural remanent magnetization (NRM), anhysteretic remanent magnetization (ARM), and isothermal remanent magnetization (IRM) and of the acquisition of IRM (IRM ACQ). **A.** Sample 182-1126B-1H-7, 6–8 cm. **B.** Sample 182-1126B-19H-3, 59–61 cm. **C.** Sample 182-1126D-11R-1, 14–16 cm. **D.** Sample 182-1126D-33R-1, 58–60 cm. The plots summarize the magnetic characteristics of the samples. The acquisition of IRM illustrated in B, C, and D is consistent with the presence of fine magnetite, although that in A demands in addition the presence of another phase that is magnetically harder. The demagnetization plots of NRM demonstrate that the sample in A is within the noise limit of the instrument, whereas the others are resolvable. The ratios of IRM:ARM in B and C are indicative of single-domain behavior and suggest a magnetotactic origin of the magnetite.

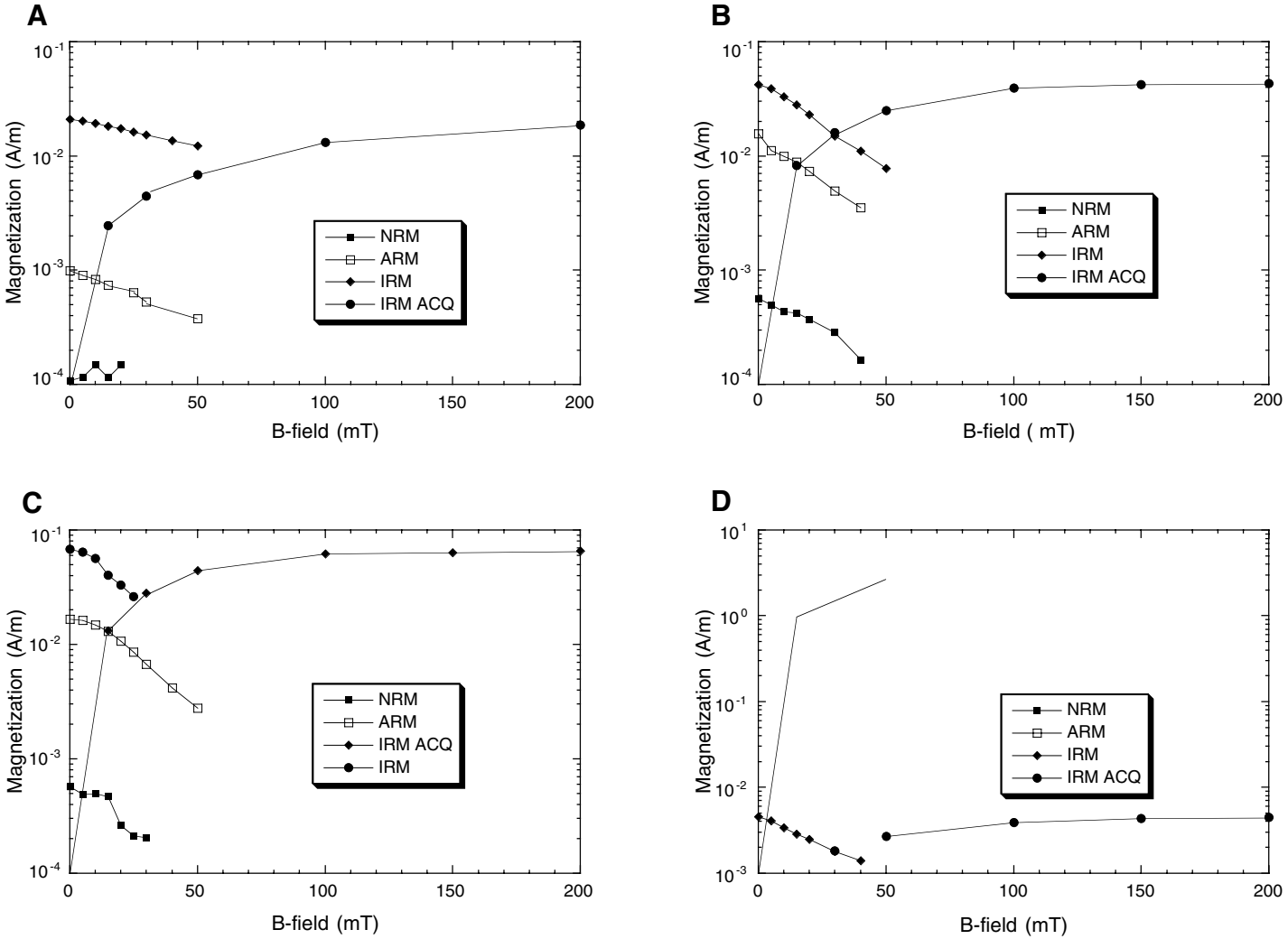

Figure F11. Composite depth section produced using the Splicer software. The black line is data from Hole 1126B, and the red line is data from Hole 1126C. GRA = gamma-ray attenuation; NGR = natural gamma radiation. All depths use the meters composite depth (mcd) scale. For conversions from mcd to mbsf, see Table T3, p. 89. (Continued on next page.)

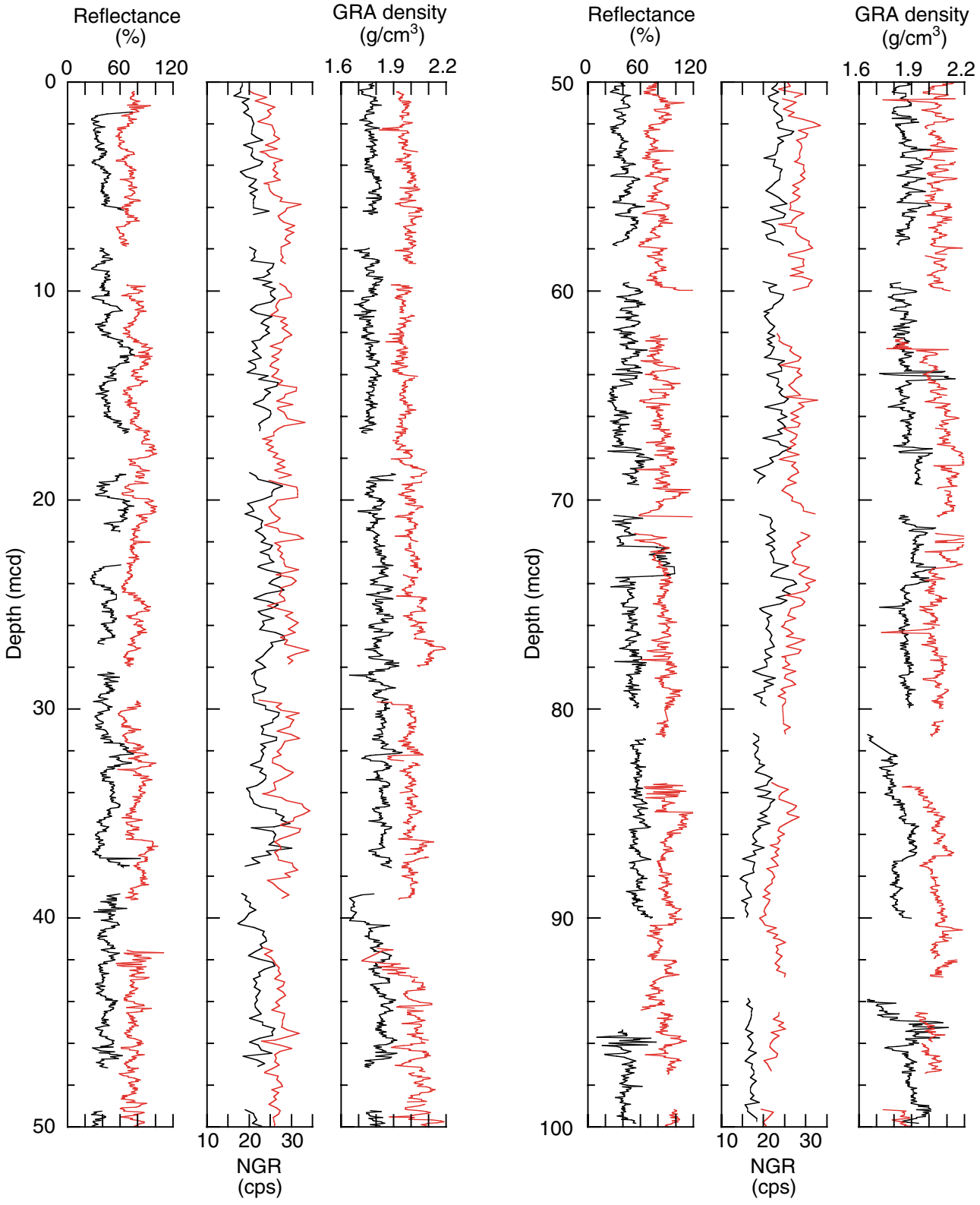

Figure F11 (continued).

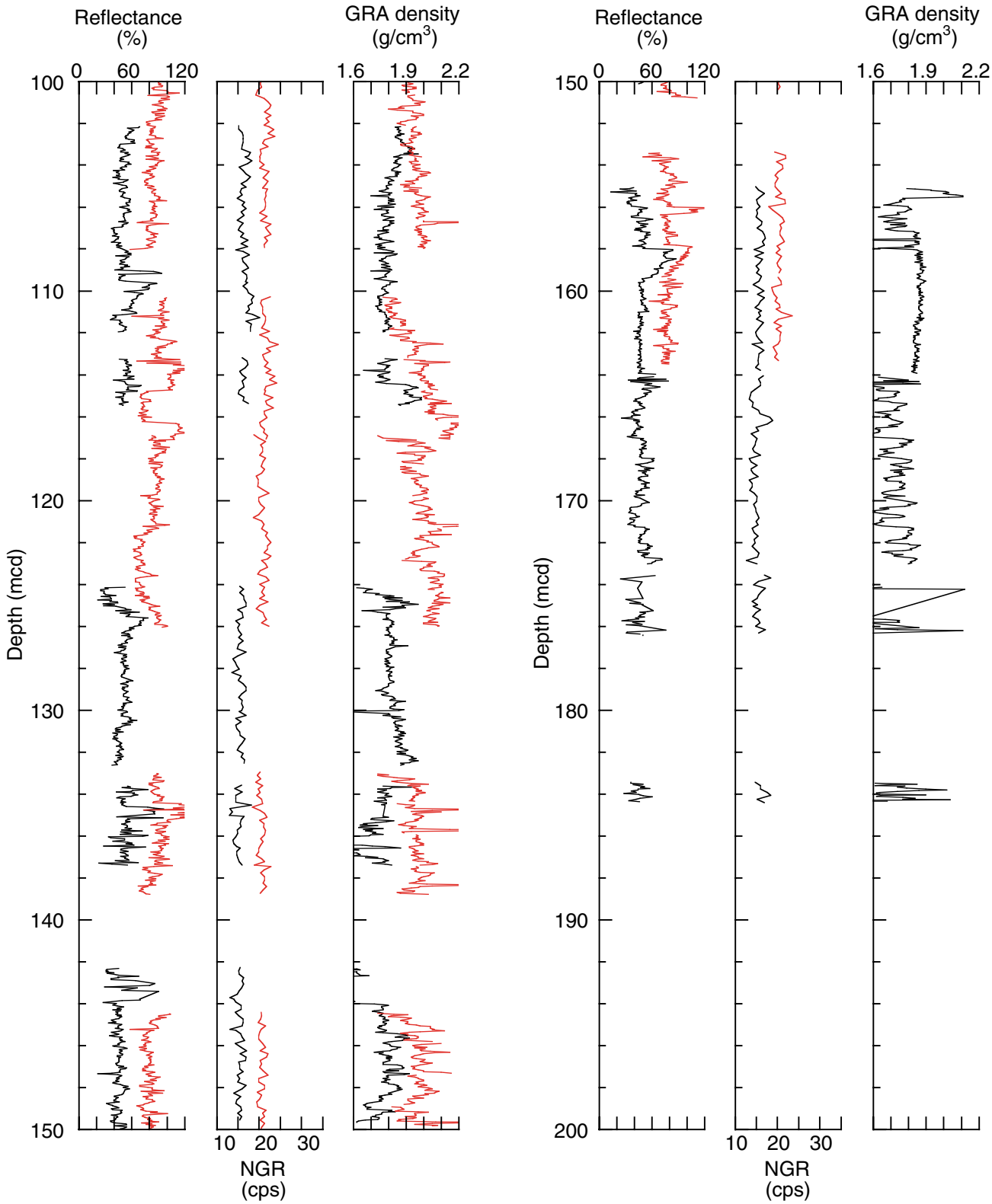

Figure F12. Spliced section of smoothed color reflectance data (400 nm) produced using the Splicer software. These data are a spliced composite of correlated data from Holes 1126B and 1126C. Ages are derived from biostratigraphic data. Lithostratigraphic units are described in "Lithostratigraphy," p. 4.

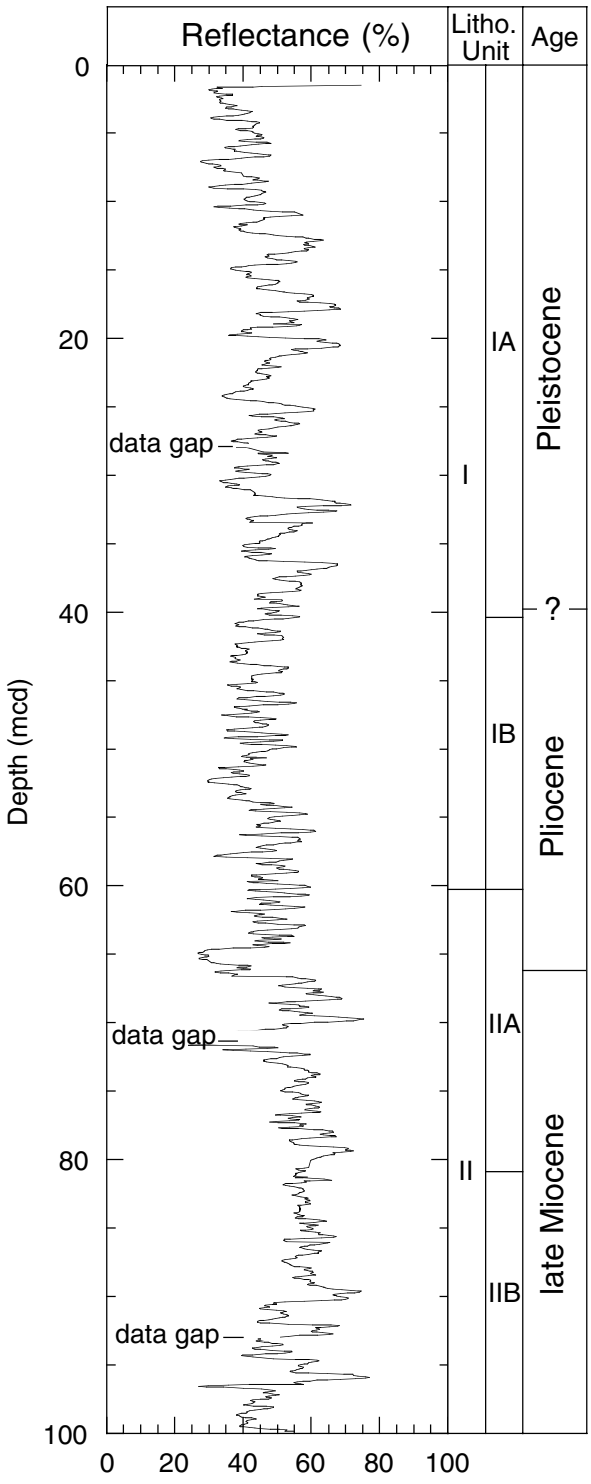

Figure F13. Spliced and tuned color reflectance record from Site 1126 compared to the composite seawater $\delta^{18}O$ curve from Site 656 (Raymo et al., 1989). The tuned record of the color reflectance ratio (400 nm) data is shown in black. The composite seawater $\delta^{18}O$ curve is shown in red.

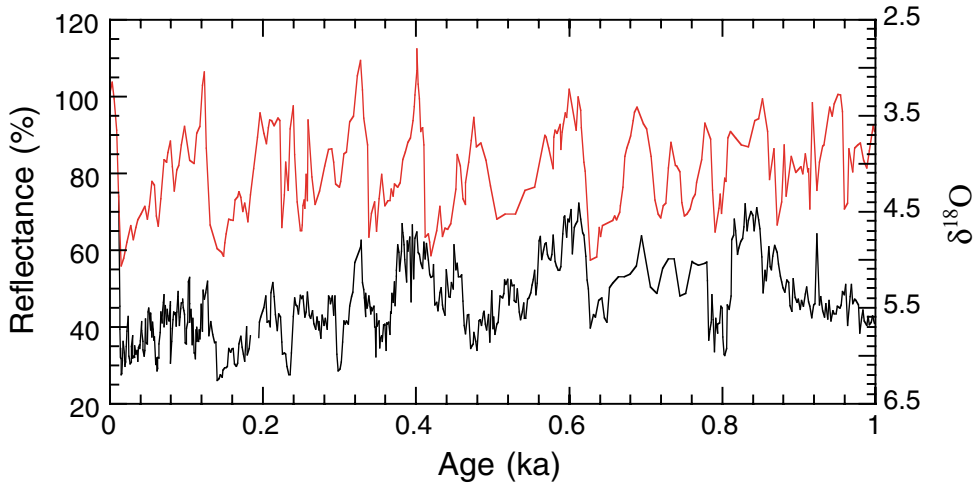

Figure F14. Calcium carbonate ($CaCO_3$) and organic carbon (C_{org}) contents of samples from Site 1126.

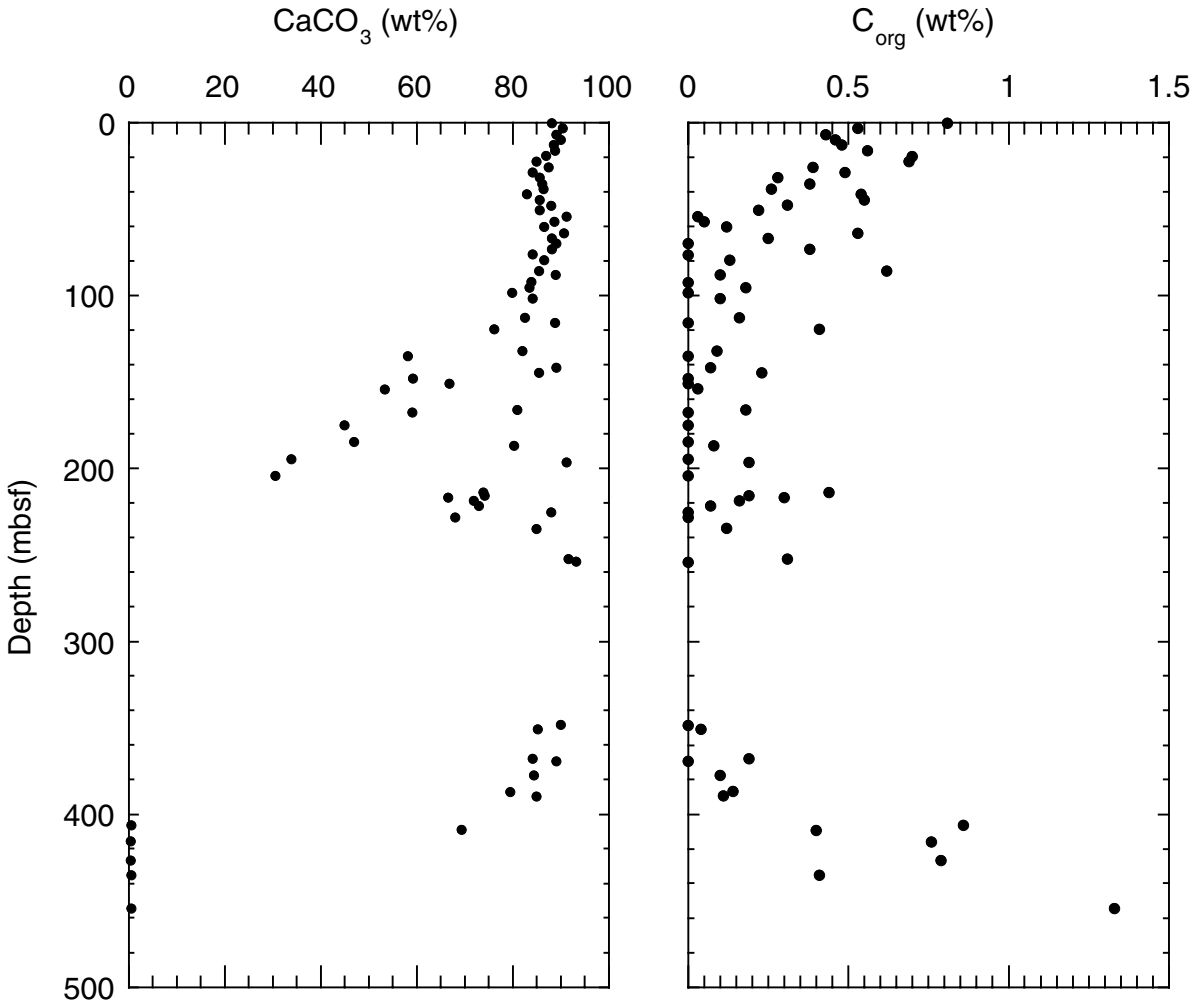

Figure F15. Summary of unnormalized anion trends in salinity, Cl^-, and SO_4^{2-}.

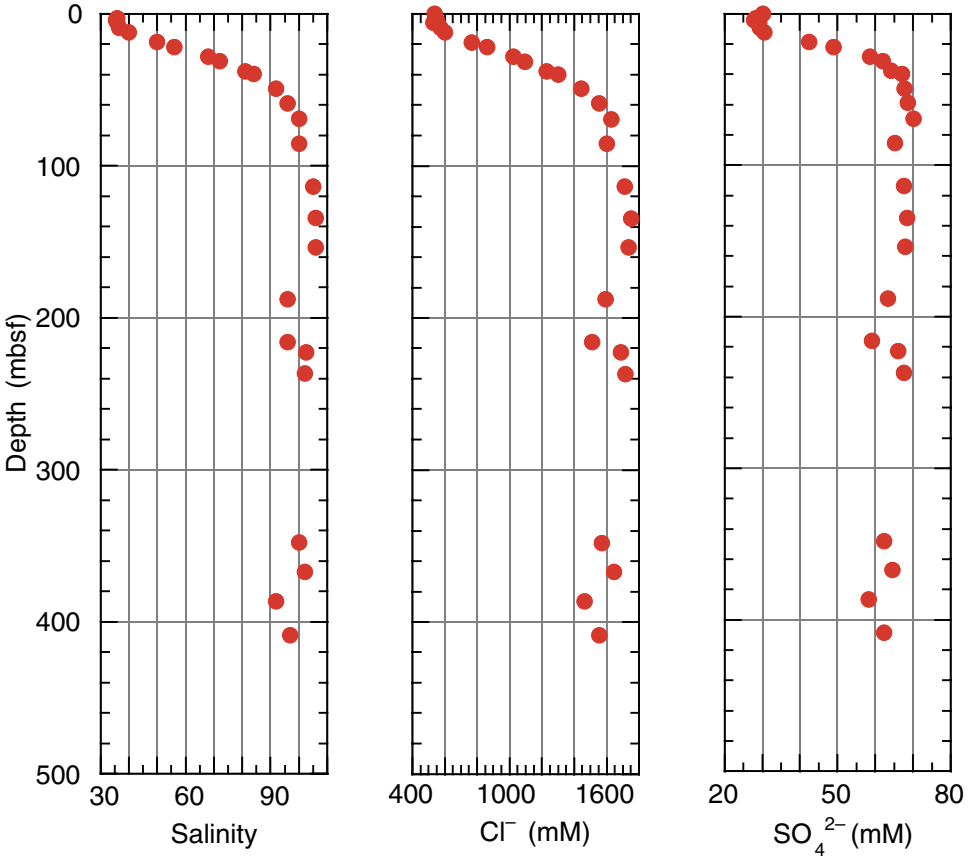

Figure F16. Summary of unnormalized cation trends in (**A**) Na^+, (**B**) K^+, (**C**) Ca^{2+}, (**D**) Mg^{2+}, (**E**) Sr^{2+}, (**F**)Li^+.

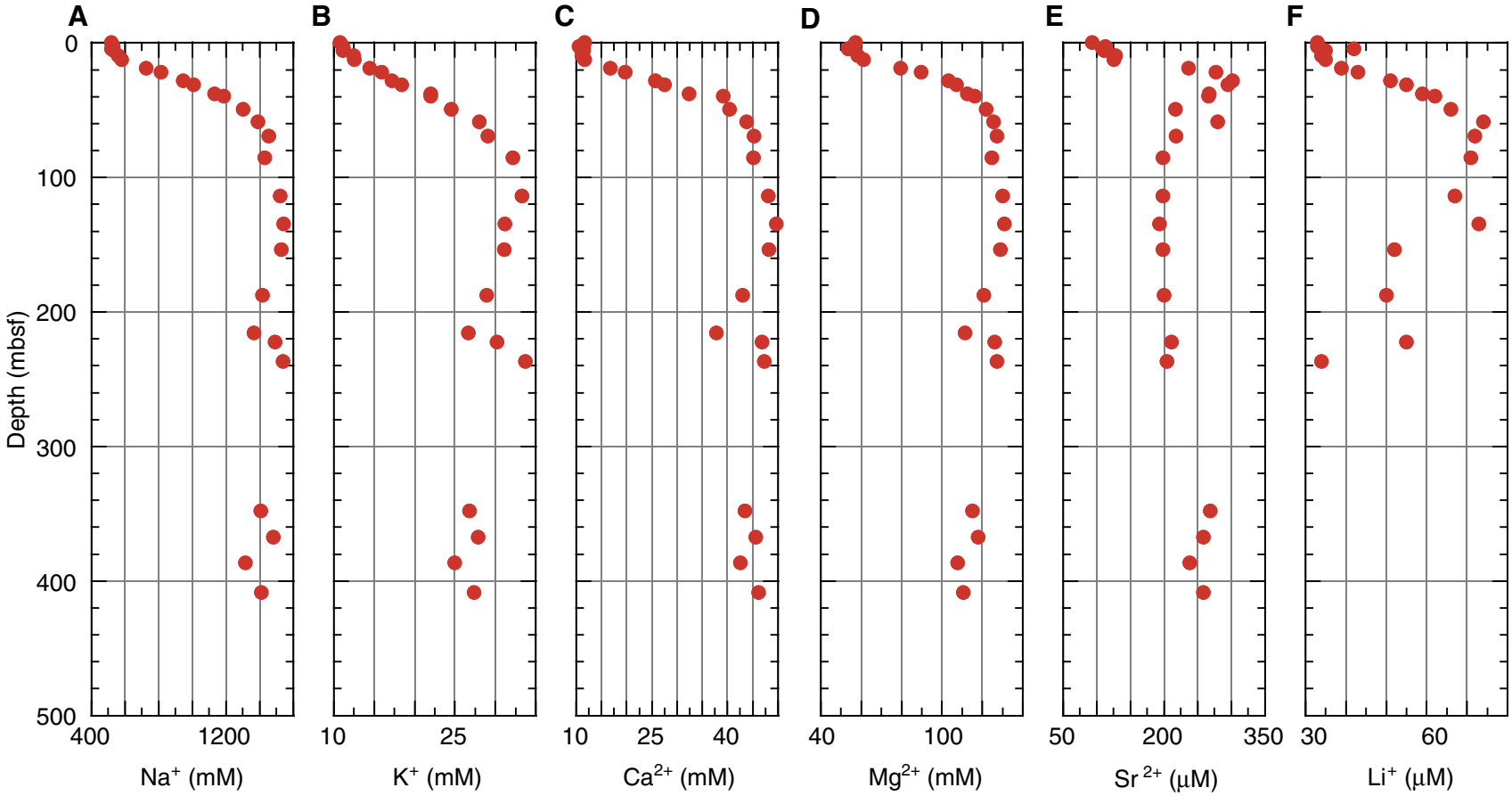

Figure F17. Summary of normalized trends in **(A)** Mg^{2+} and Ca^{2+} and **(B)** SO_4^{2-} and alkalinity.

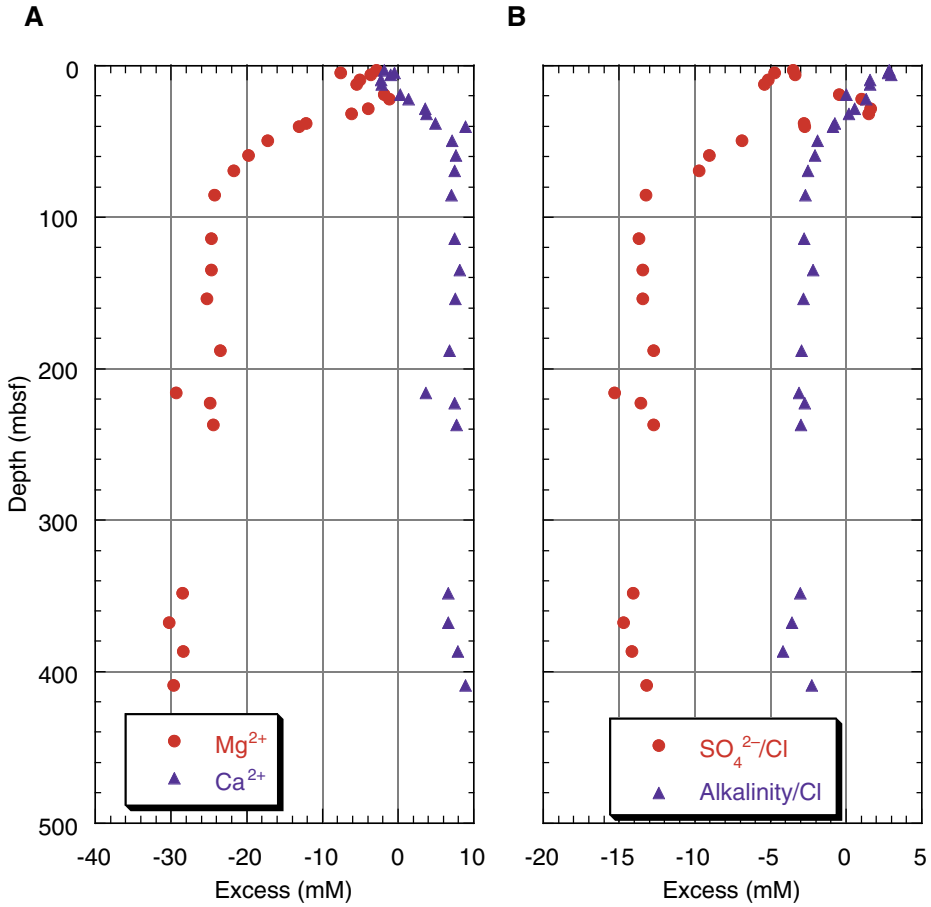

Figure F18. Summary trends in the Na^+/Cl^- ratio with increasing depth. Data from Site 1126 plot along a line near 0.86 equal to the Na^+/Cl^- ratio in seawater. Fluids arising from a NaCl brine plot near a value of unity, whereas fluids originating from a $CaCl_2$ brine plot to the left of the figure.

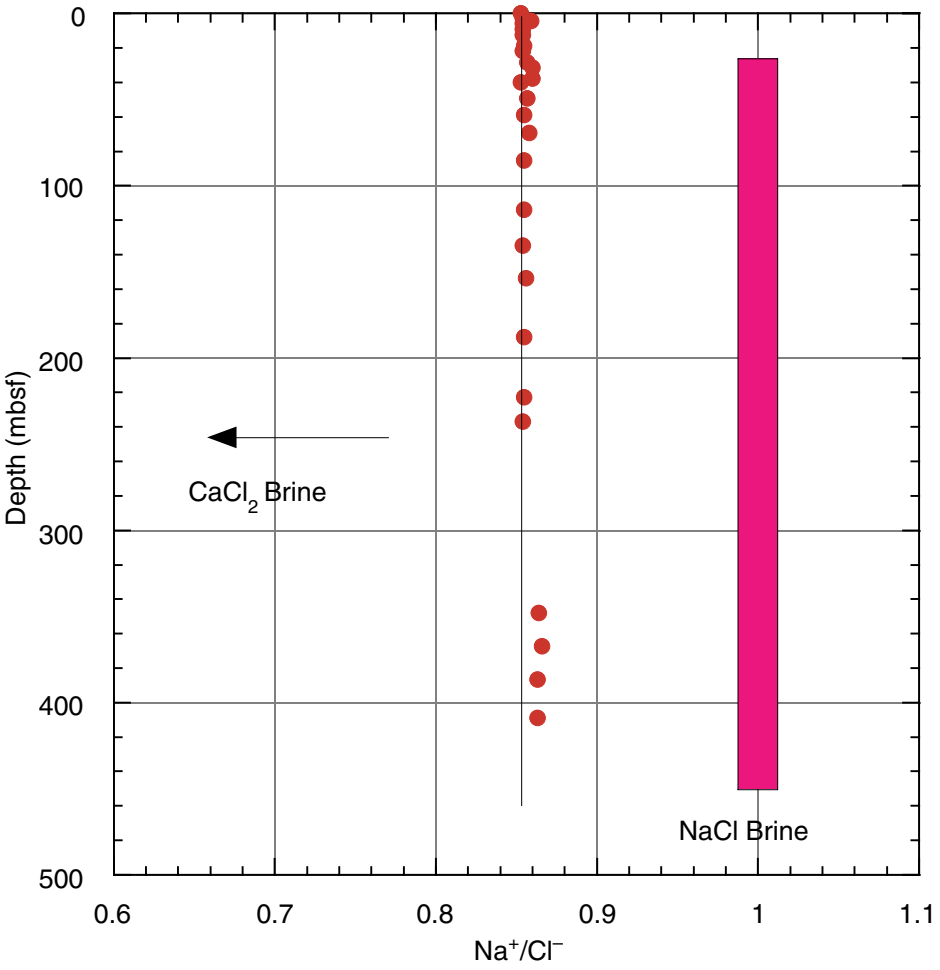

Figure F19. Downhole variation in the Sr^{2+}/Ca^{2+} ratio of pore waters.

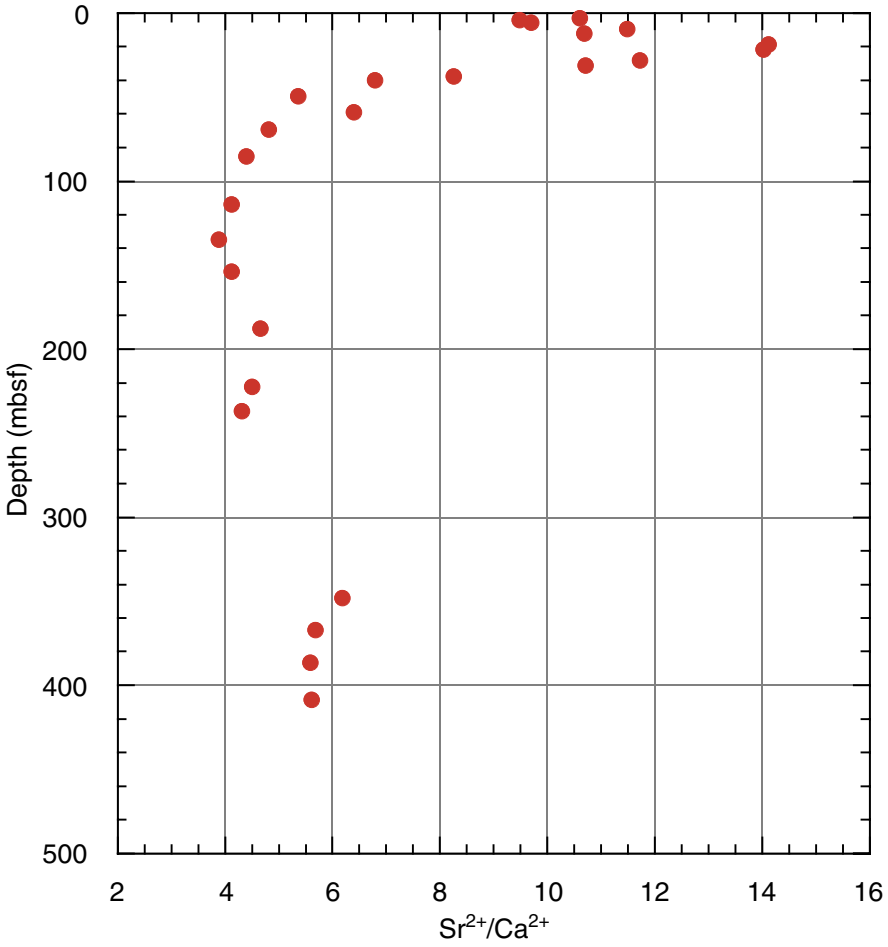

Figure F20. Variation in the percentage of aragonite (A), low-Mg calcite (LMC), high-Mg calcite (HMC), dolomite (D), and quartz (Q).

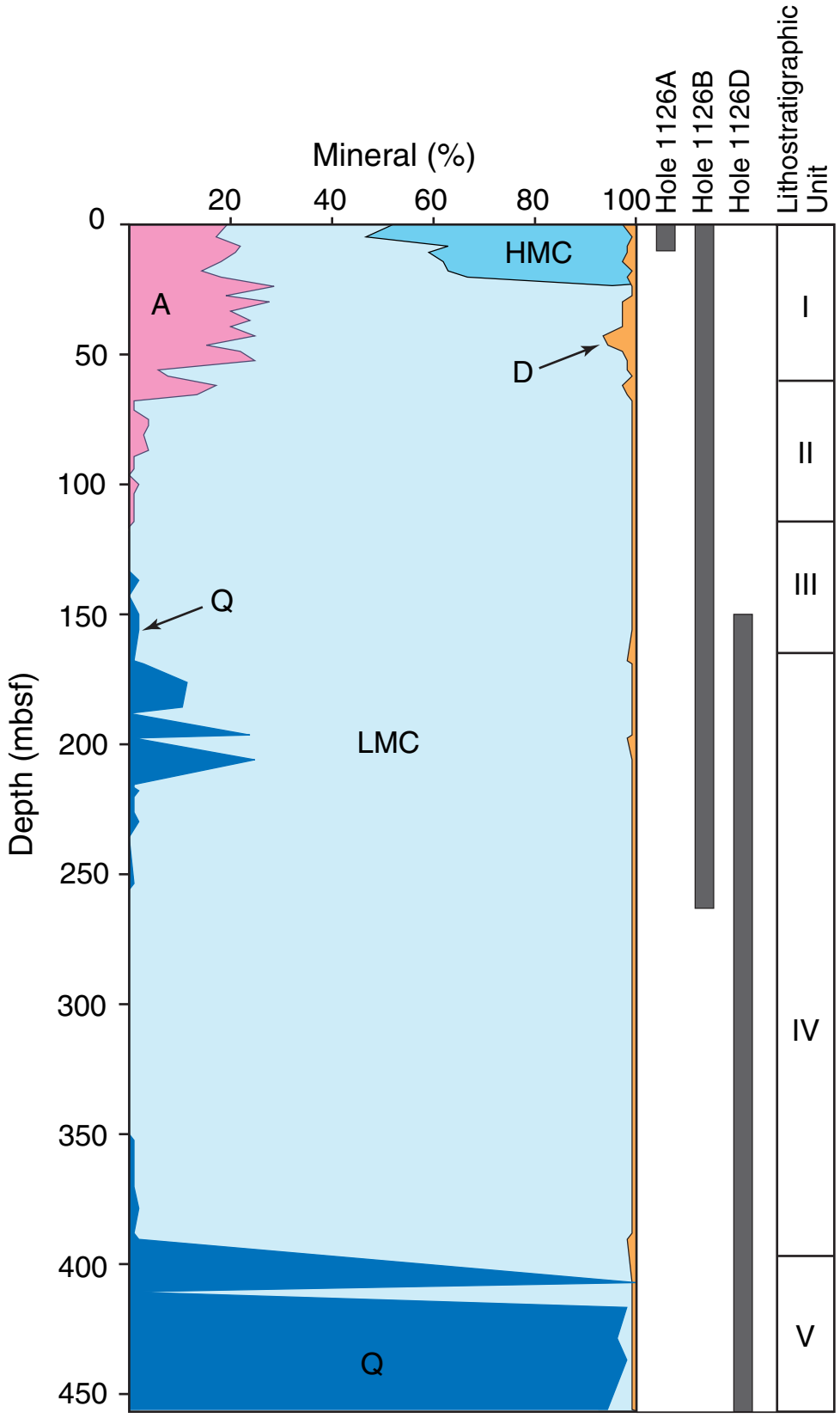

Figure F21. Comparison of **(A)** uncorrected and **(B)** corrected gamma-ray attenuation (GRA) densiometry values vs. discrete bulk density measurements. Correction from Boyce (1976).

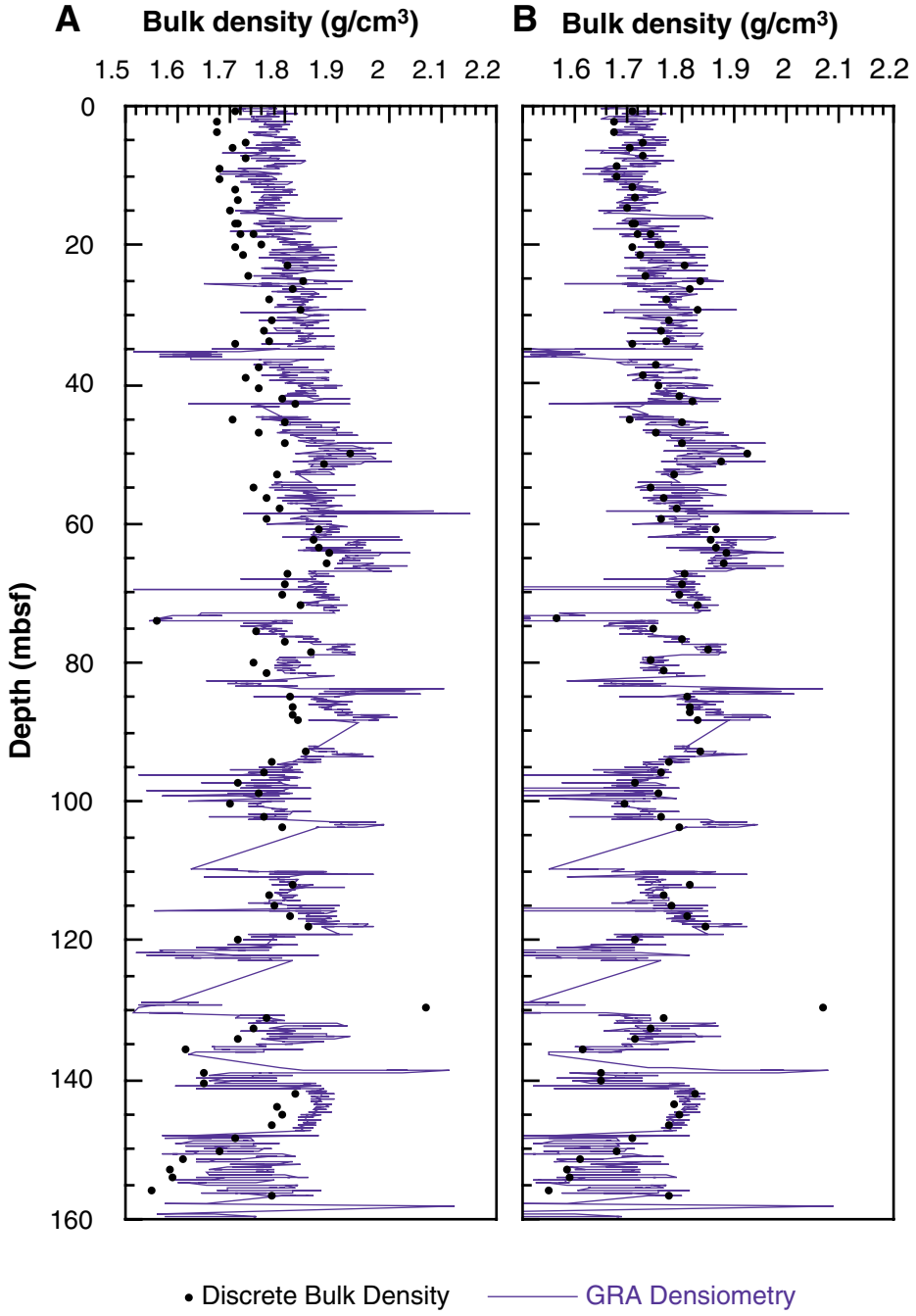

Figure F22. Combined plot of *P*-wave velocity (PWS1 and PWS2, blue; PWS3, red), gamma-ray attenuation (GRA; lines) and moisture and density (MAD; dots) bulk densities, porosity, magnetic susceptibility, and natural gamma radiation (NGR) from Site 1126. Black dots represent discrete density and porosity measurements. With the exception of *P*-wave velocity and porosity, Hole 1126A is indicated in green, Hole 1126B in blue, Hole 1126C in red, and Hole 1126D in dark green dots. Physical properties units (PP units) are indicated on the right. PWS3 velocities tend to be higher than those measured using PWS1 and PWS2 as a result of sediment compaction between the transducers. (**Figure shown on next page.**)

Figure F22. (Caption on previous page.)

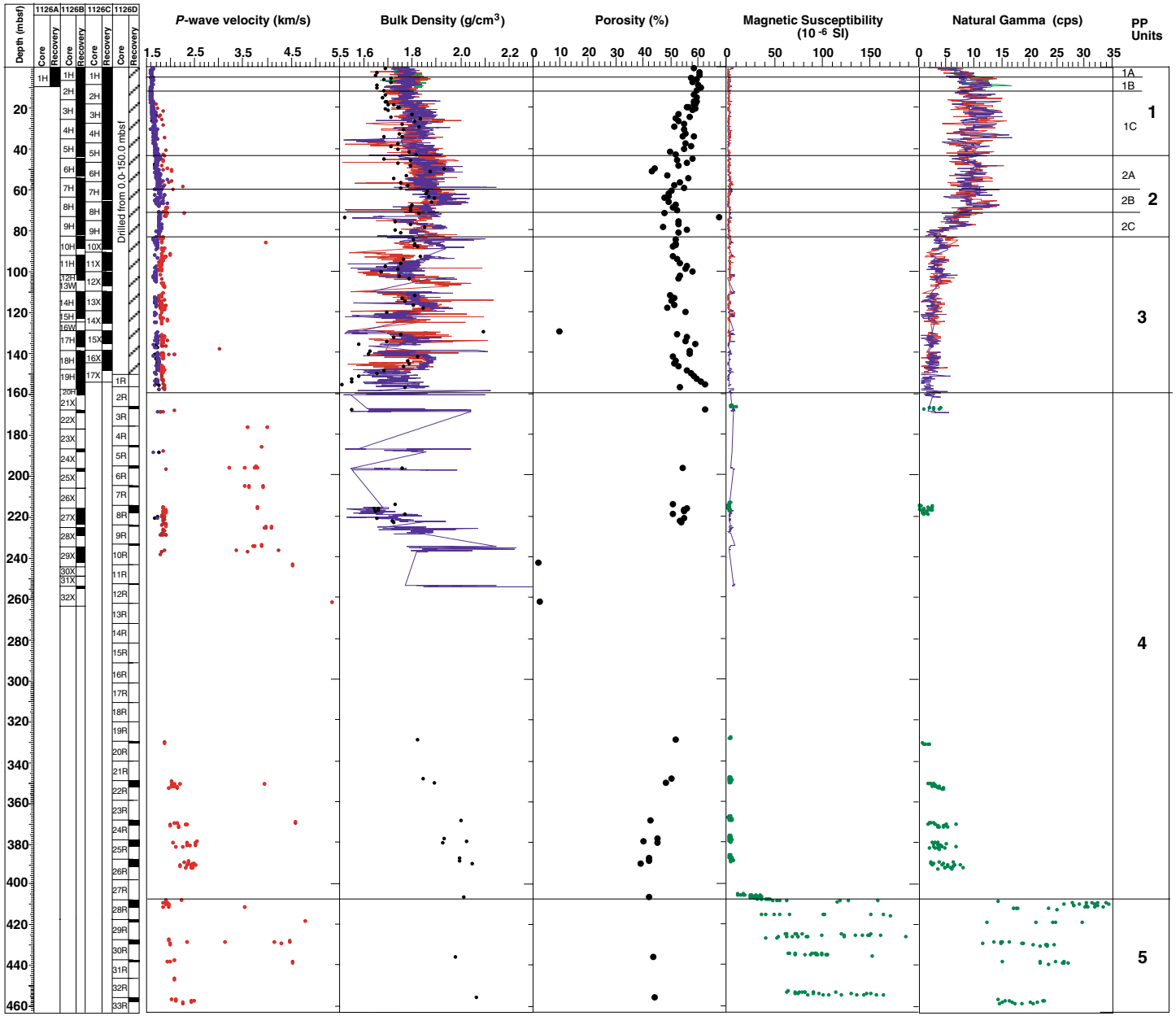

Figure F23. Combined plot of gamma-ray attenuation (GRA) and moisture and density (MAD) bulk densities, *P*-wave velocities, and natural gamma radiation (NGR) from the upper 170 m at Site 1126. Black dots represent discrete density measurements. With the exception of *P*-wave velocity, Hole 1126A is indicated in green, Hole 1126B in blue, and Hole 1126C in red. Physical properties units (PP units) are indicated on the right.

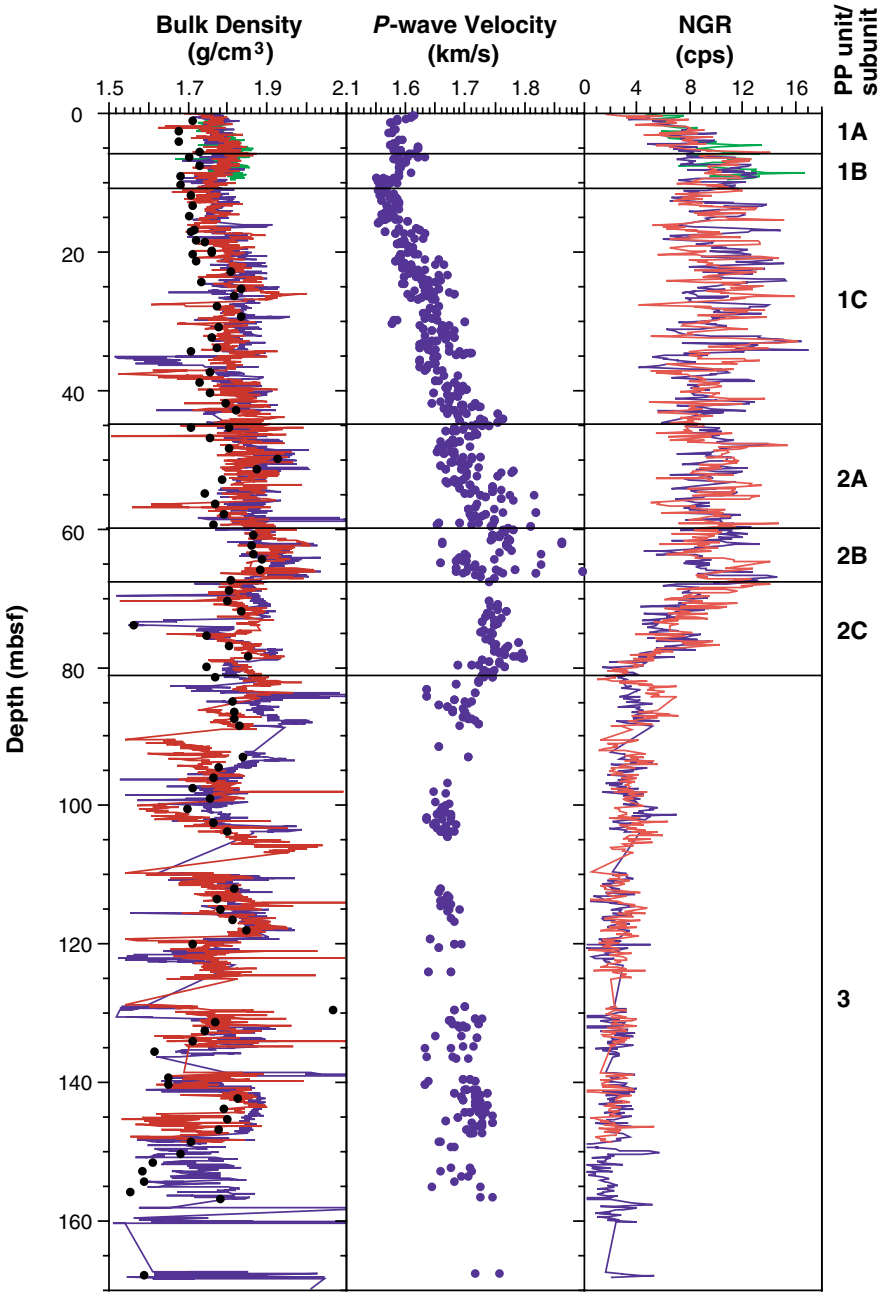

Figure F24. Shear strength from Holes 1126B (blue) and 1126C (red). Physical properties units (PP units) are indicated on the right.

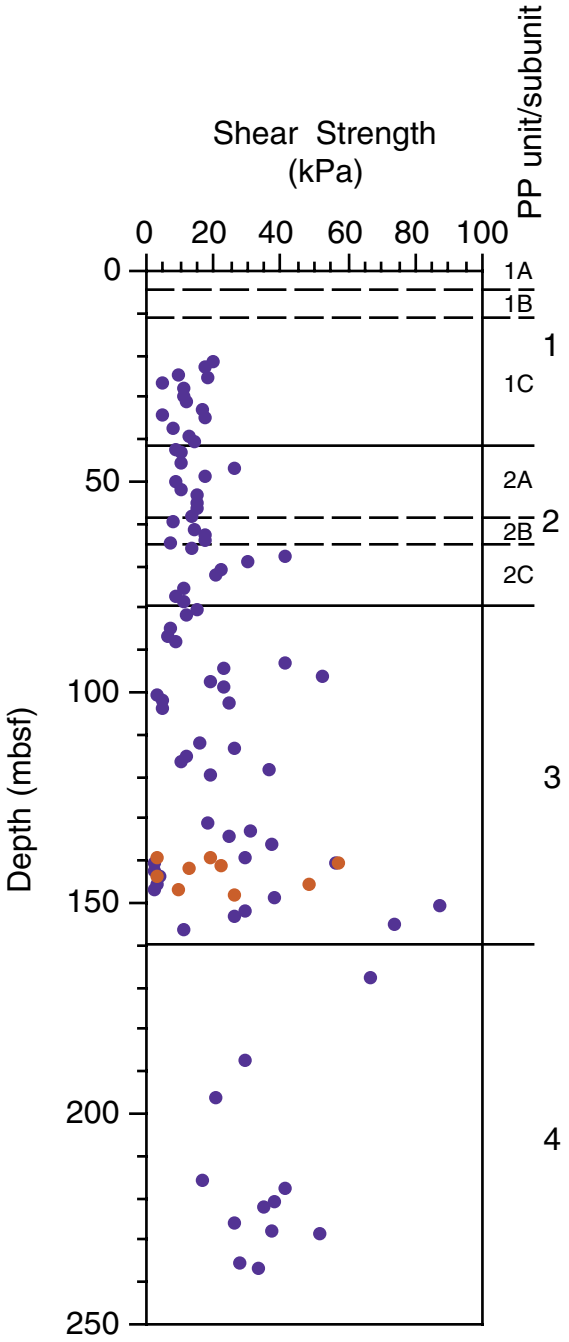

Figure F25. Thermal conductivity and *P*-wave velocity data which shows the close relationship between thermal conductivity and *P*-wave velocity. Physical properties units (PP units) are indicated on the right.

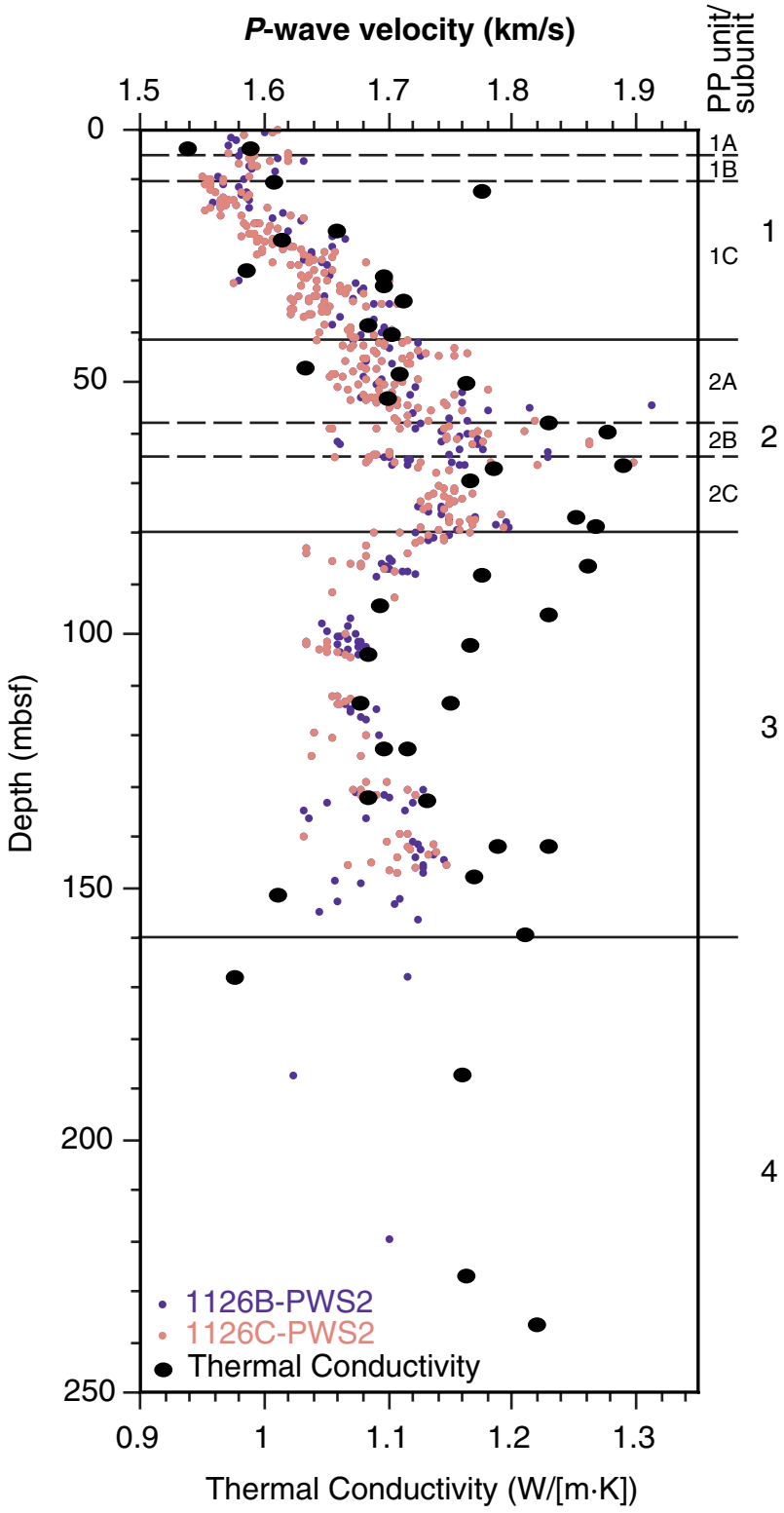

Figure F26. Summary of geophysical logs vs. depth from triple combination logging tool and sonic/geologic high-resolution magnetic tool for the open-hole (lower) part of the cored interval. From left to right, columns are core recovery; gamma radiation (HSGR) and caliper; porosity and density; photoelectric effect (PEF); shallow, medium and deep resistivity; sonic velocity; magnetic susceptibility; logging units; lithostratigraphic units; and biostratigraphic ages. (Continued on next page.)

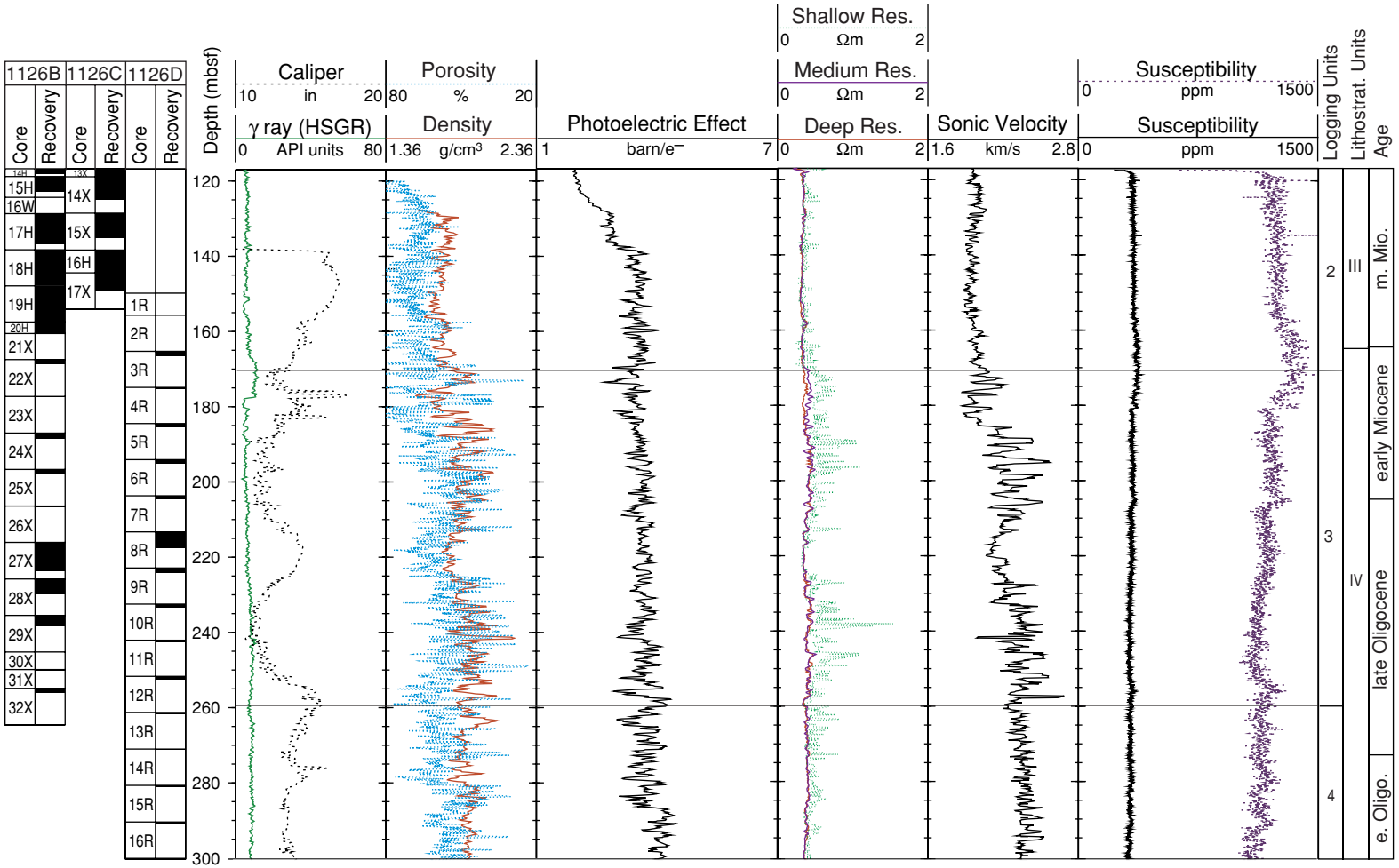

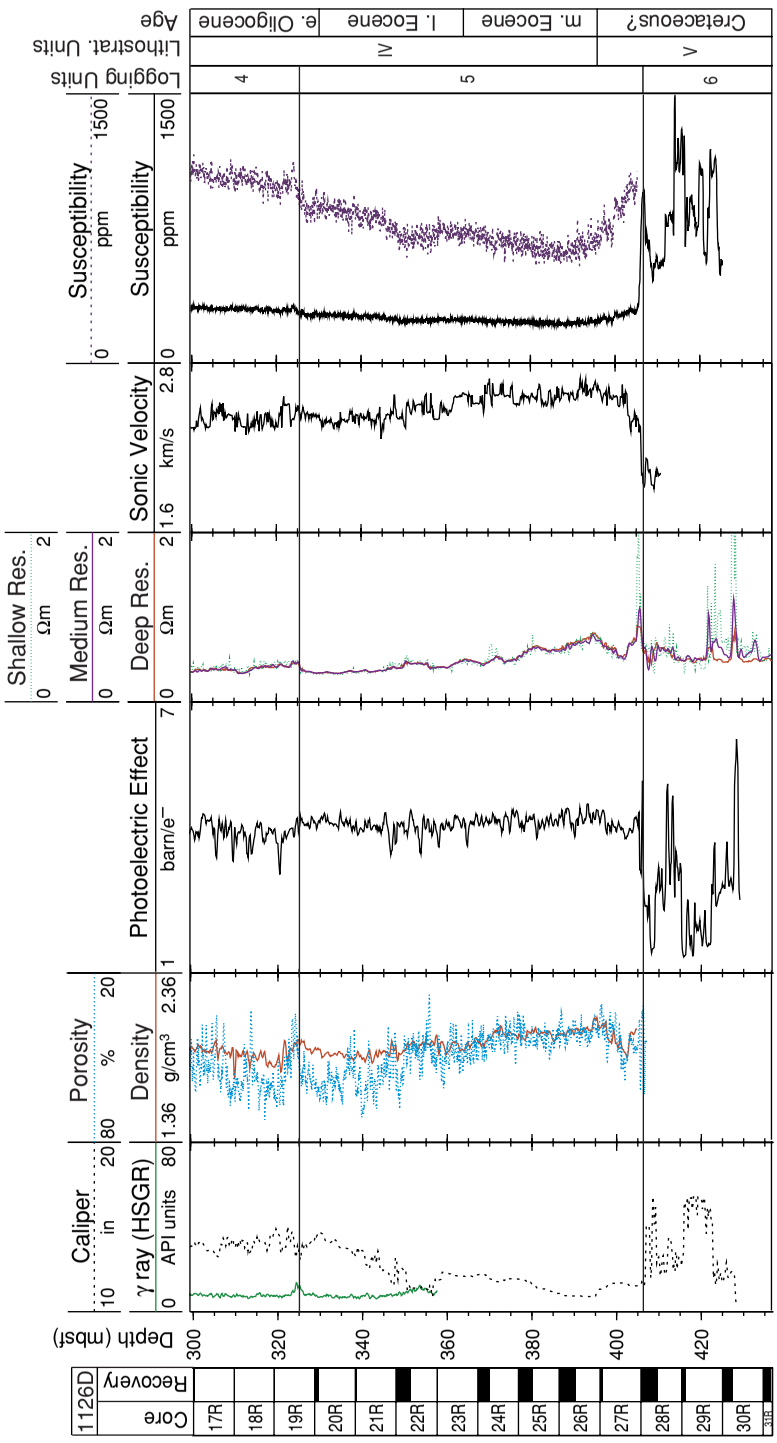

Figure F26 (continued).

Figure F27. Summary of spectral gamma-ray logs from the hostile environment natural gamma-ray sonde vs. depth, plotted on an expanded depth scale to highlight variations in the interval logged through pipe. From left to right, columns are core recovery; caliper, total gamma radiation (HSGR), and computed (uranium-free) gamma radiation (HCGR); uranium; thorium; potassium; logging units; lithostratigraphic units; and biostratigraphic ages.

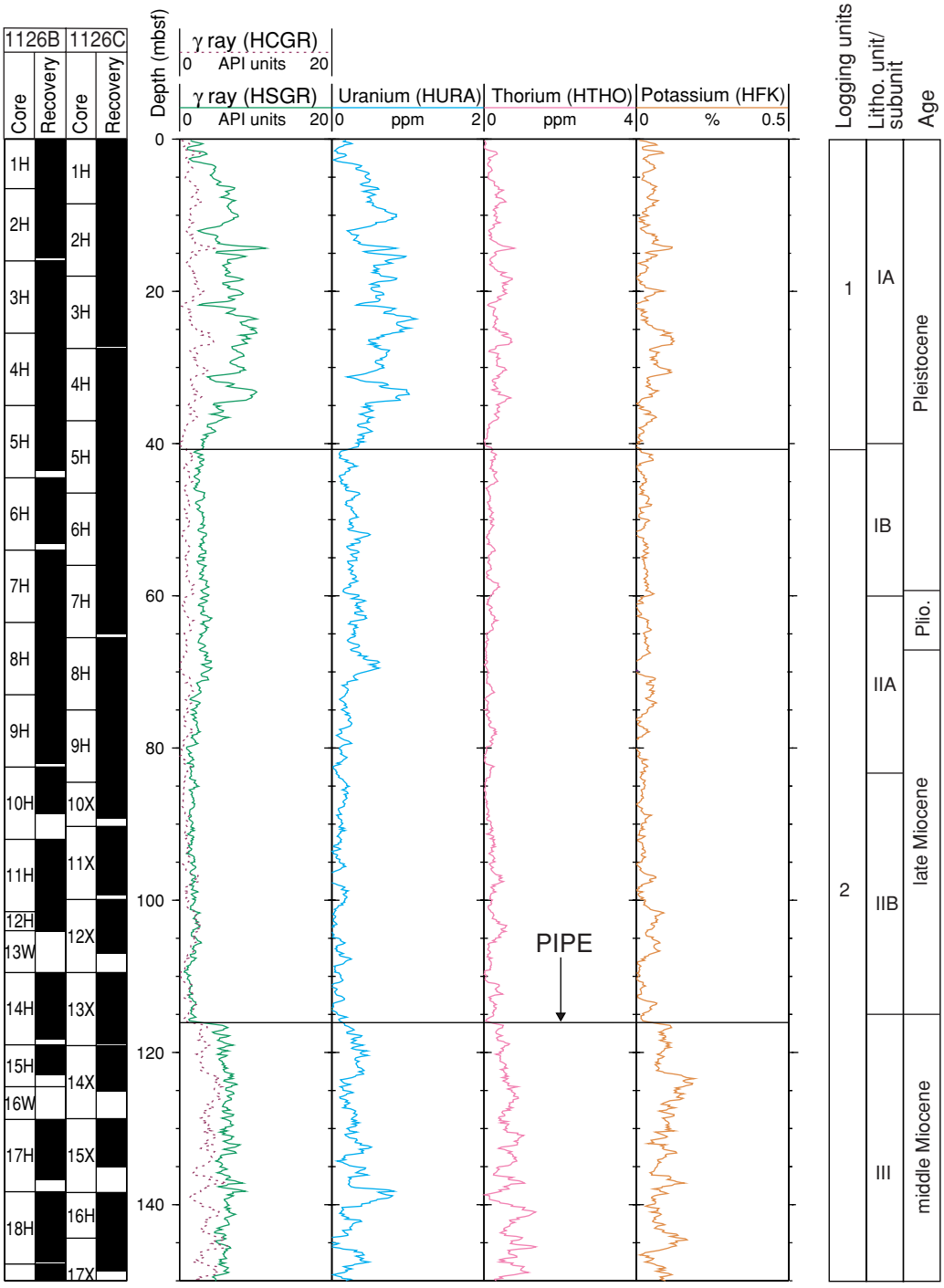

Figure F28. Summary of spectral gamma-ray logs vs. depth for the open-hole (lower) part of the cored interval. From left to right, columns are core recovery; caliper, total gamma radiation (HSGR), and computed (uranium-free) gamma radiation (HCGR); uranium; thorium; potassium; logging units; lithostratigraphic units; and biostratigraphic ages.

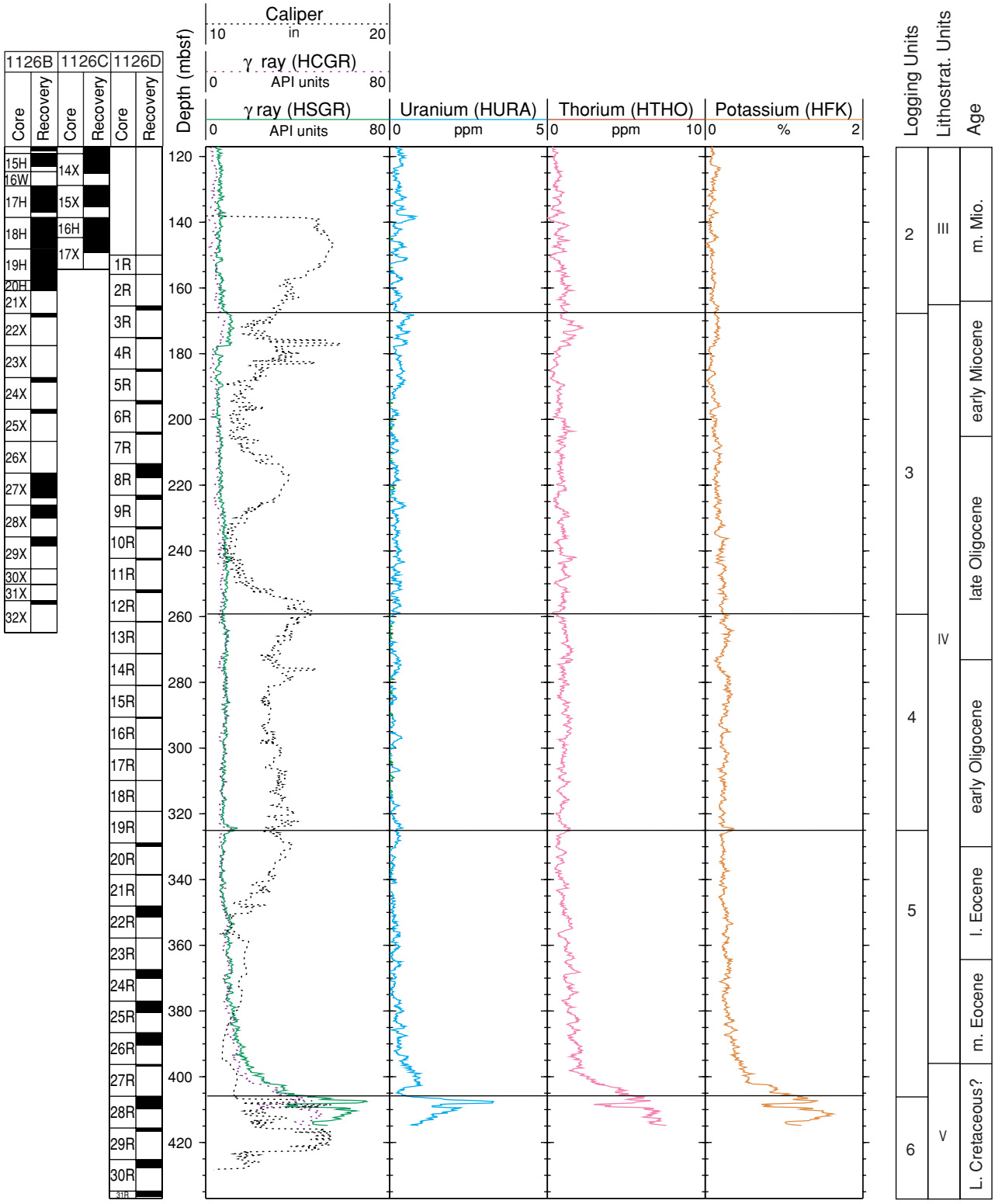

Figure F29. Log of acoustic impedance vs. depth calculated from density and sonic logs from Site 1126. Possible locations of seismic reflectors are shown. Dashed curve represents all data, whereas solid curve represents data smoothed using a 20-point running average.

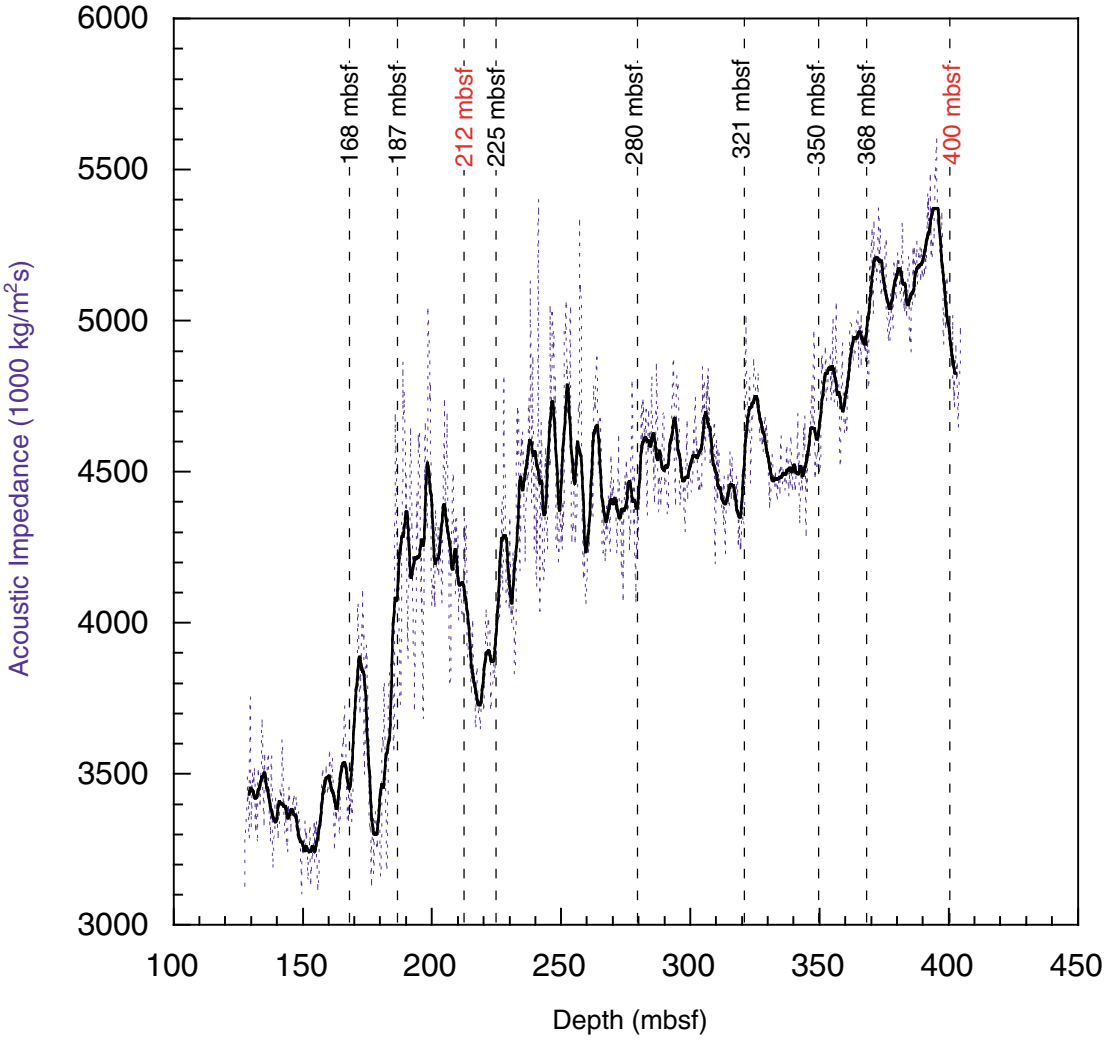

Figure F30. Map showing seismic site-survey tracks for Site 1126 (Line AGSO169/03) in relation to other Leg 182 sites and the AGSO169 site-survey seismic lines. The bold trackline (AGSO169/03g) corresponds to the seismic line segment shown in Figure **F31,** p. 81.

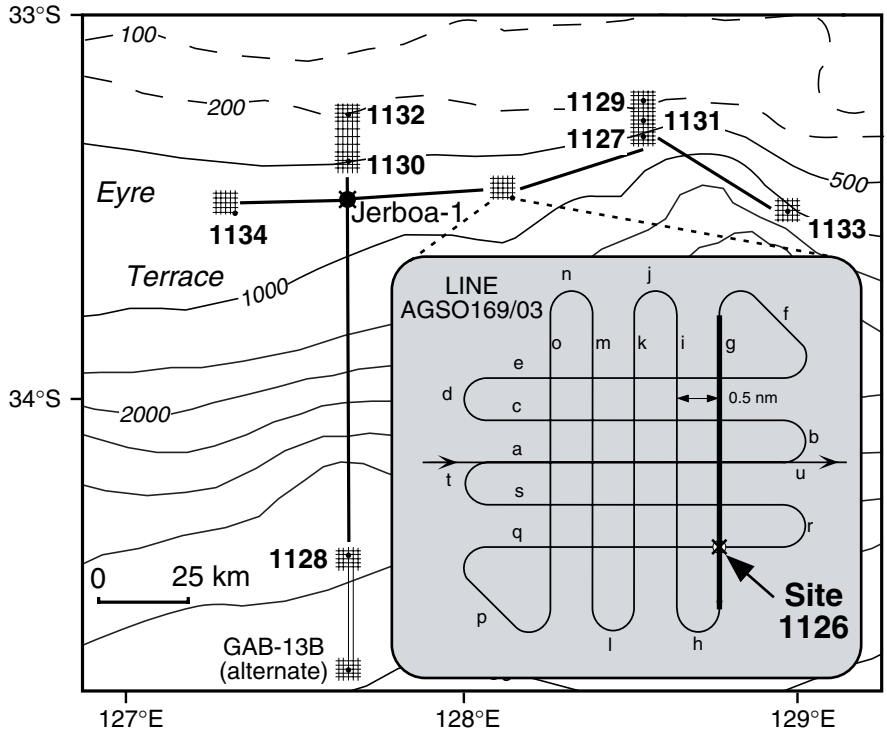

Figure F31. Portion of seismic Line AGSO169/03g showing interpreted seismic stratigraphic sequences planned (shown in white) and actually intersected (shown in black) at Site 1126.

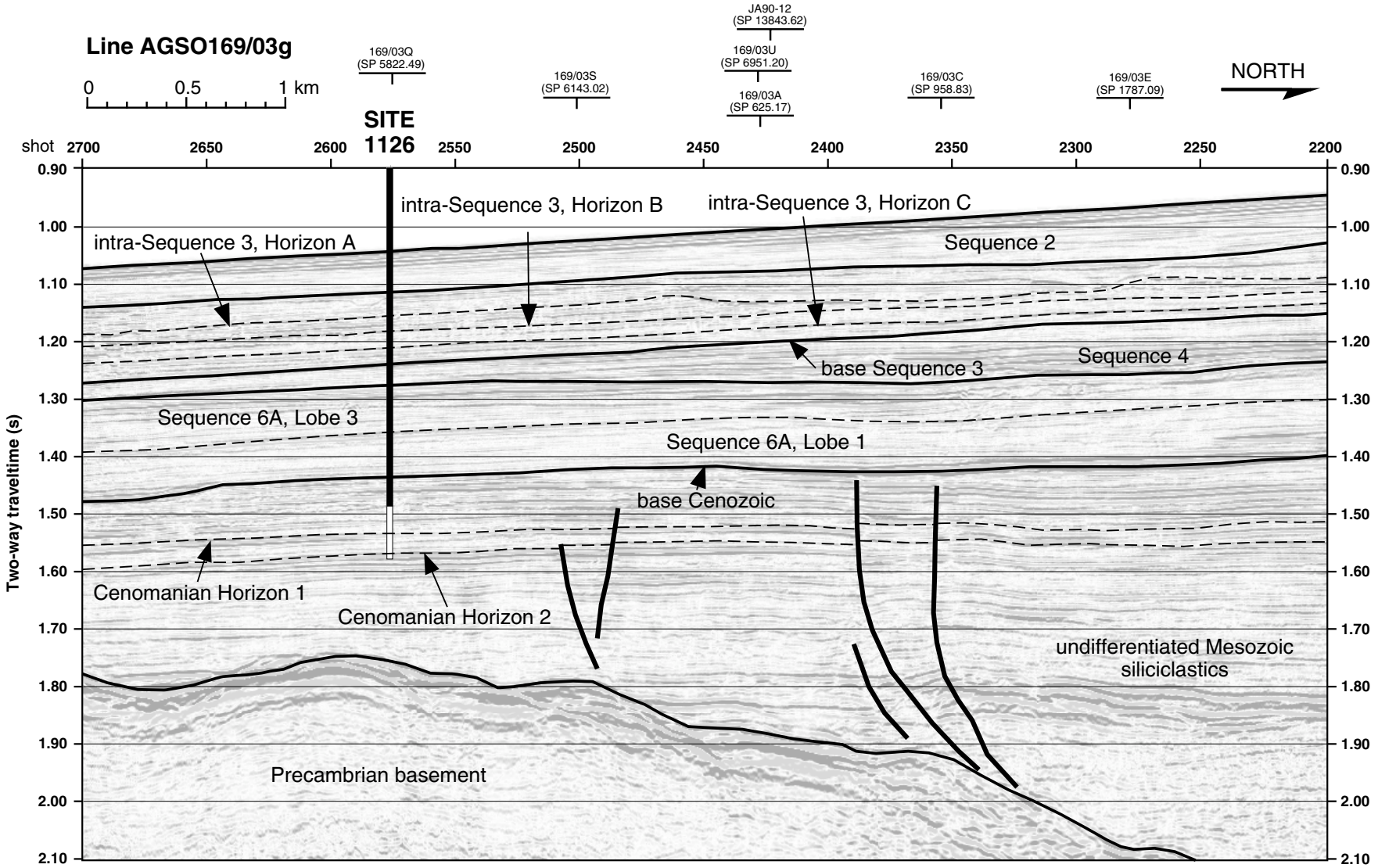

Figure F32. Check-shot stations and acquisition geometry for the well seismic tool (WST) survey at Site 1126, with corrected two-way traveltimes (TWT) and derived interval velocities.

Depth (mbrf)	Depth (mbsl)	Transit time (ms)	True path length (m)	Corrected TWT (ms)	Interval velocity (ms)
913.90	902.7	594.30	912.27	1190.72	2099.17
957.10	945.9	614.85	955.41	1231.88	2184.60
1024.80	1013.6	645.80	1023.02	1293.84	2188.06
1064.80	1053.6	664.06	1062.98	1330.40	2411.23
1108.90	1097.7	682.33	1107.03	1366.97	2367.74
1134.90	1123.7	693.30	1133.00	1388.92	2359.95
1158.90	1147.7	703.46	1156.98	1409.25	2641.48
1188.30	1177.1	714.58	1186.35	1431.50	1793.59
1203.90	1192.7	723.27	1201.94	1448.90	

Corrected TWT is TWT from sea level to WST tool along a vertical path

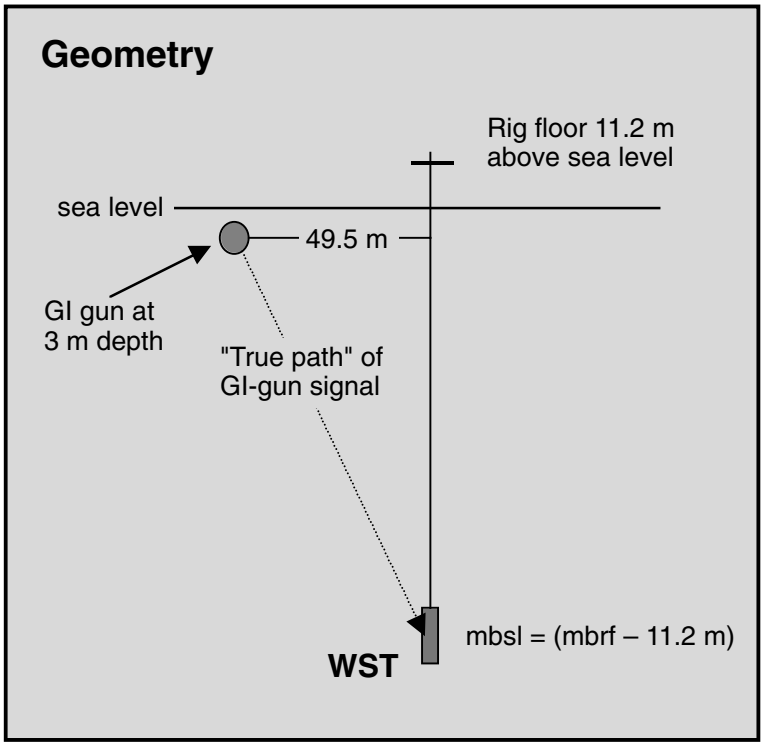

Figure F33. A. Plot showing relationship between predicted depths to key horizons and sequence boundaries (dashed) and corrected depths (arrowed). Corrected depths are based on the check-shot survey data (heavy line), shown plotted at the lower limit of the envelope of stacking velocities (derived from six common depth points from site-survey seismic data adjacent to this site). The integrated sonic log, based on interval transit-time data, is plotted as a heavy dashed line. **B.** Interval velocities derived from the nine check-shot stations shown overlying the velocity log (from compressional sonic trace).

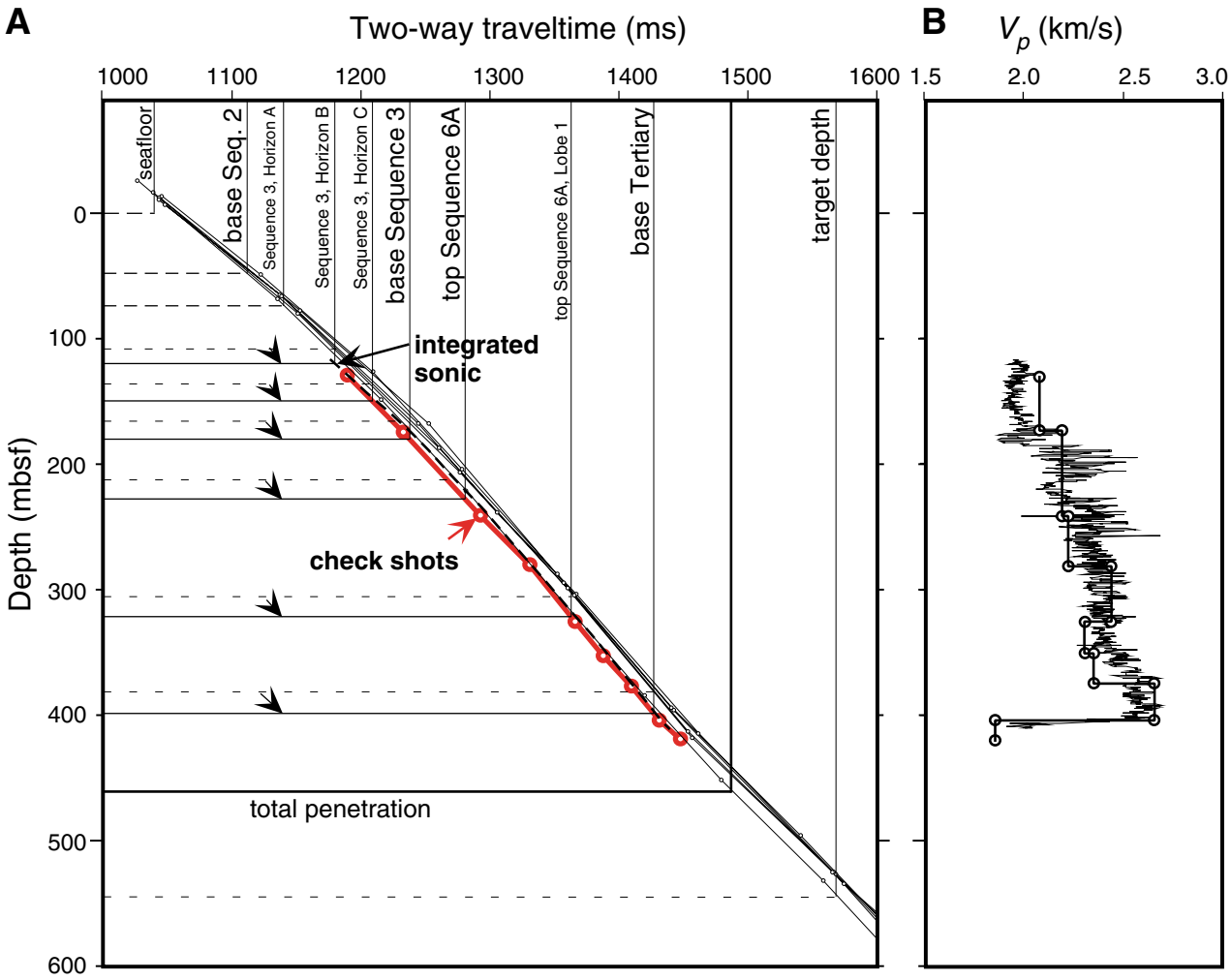

Figure F34. Tentative summary correlation between lithostratigraphic units, seismic sequences, biostratigraphic hiatuses, and ages at Site 1126. ? = seismic data shows missing section corresponding to these surfaces, although biostratigraphic data provide no constraint on the length of missing time.

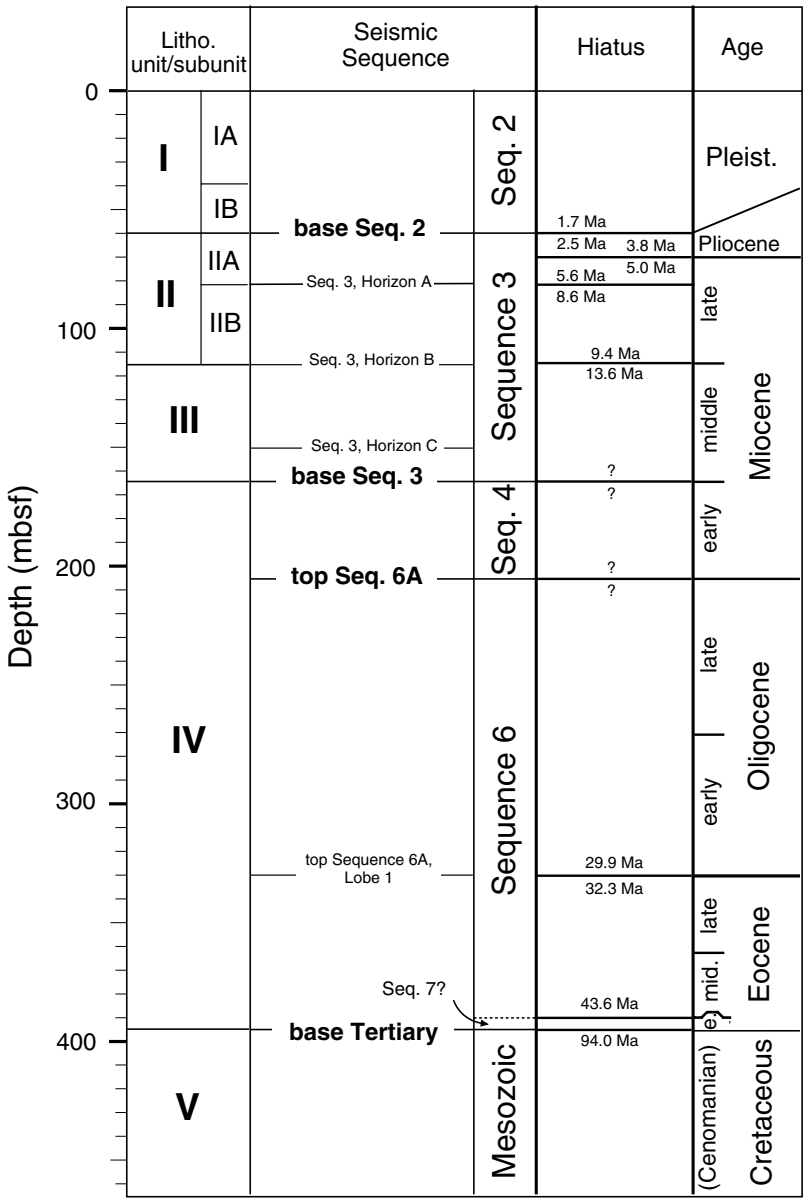

Table T1. Site 1126 coring summary. (See table note. Continued on next two pages.)

Hole 1126A

Latitude: –33.509358° (33°30.5615′S)
Longitude: 128.066595° (128°3.9957′E)
Seafloor (drill-pipe measurement from rig floor, mbrf): 796.00
Distance between rig floor and sea level (m): 11.20
Water depth (drill-pipe measurement from sea level, m): 784.80
Total depth (from rig floor, mbrf): 805.50
Penetration (mbsf): 9.50
Total number of cores: 1
Total length of cored section (m): 9.50
Total core recovered (m): 9.69
Core recovery (%): 102.00

Hole 1126B

Latitude: –33.509355° (33°30.5613′S)
Longitude: 128.066536° (128°3.9922′E)
Seafloor (drill-pipe measurement from rig floor, mbrf): 795.00
Distance between rig floor and sea level (m): 11.20
Water depth (drill-pipe measurement from sea level, m): 783.80
Total depth (from rig floor, mbrf): 1058.30
Penetration (mbsf): 263.30
Total number of cores: 32
Total length of cored section (m): 253.50
Total number of drilled intervals: 2
Total length of drilled intervals (m): 9.80
Total core recovered (m): 162.55
Core recovery (%): 64.12

Hole 1126C

Latitude: –33.509397° (33°30.5638′S)
Longitude: 128.066835° (128°4.0101′E)
Seafloor (drill-pipe measurement from rig floor, mbrf): 795.00
Distance between rig floor and sea level (m): 11.20
Water depth (drill-pipe measurement from sea level, m): 783.80
Total depth (from rig floor, mbrf): 949.00
Penetration (mbsf): 154.00
Total number of cores: 17
Total length of cored section (m): 154.00
Total core recovered (m): 138.52
Core recovery (%): 89.95

Hole 1126D

Latitude: –33.509355° (33°30.5613′S)
Longitude: 128.066407° (128°3.9844′E)
Seafloor (drill-pipe measurement from rig floor, mbrf): 795.00
Distance between rig floor and sea level (m): 11.20
Water depth (drill-pipe measurement from sea level, m): 783.80
Total depth (from rig floor, mbrf): 1258.30
Penetration (mbsf): 463.30
Total number of cores: 33
Total length of cored section (m): 313.30
Total number of drilled intervals: 1
Total length of drilled intervals (m): 150.00
Total core recovered (m): 40.47
Core recovery (%): 12.92

Core	Date (Oct 1998)	Time (UTC + 8 hr)	Depth (mbsf)	Length cored (m)	Length recovered (m)	Recovery (%)	Comment
182-1126A-							
1H	25	0545	0.00-9.50	9.5	9.69	102.0	
Totals:				9.5	9.69	102.0	
182-1126B-							
1H	26	0630	0.00-6.50	6.5	6.56	100.9	
2H	26	0710	6.50-16.00	9.5	9.18	96.6	
3H	26	0800	16.00-25.50	9.5	9.90	104.2	
4H	26	0830	25.50-35.00	9.5	9.56	100.6	

Table T1 (continued).

Core	Date (Oct 1998)	Time (UTC + 8 hr)	Depth (mbsf)	Length cored (m)	Length recovered (m)	Recovery (%)	Comment
5H	26	0900	35.00-44.50	9.5	8.55	90.0	
6H	26	0930	44.50-54.00	9.5	8.73	91.9	
7H	26	1005	54.00-63.50	9.5	9.93	104.5	
8H	26	1040	63.50-73.00	9.5	9.49	99.9	
9H	26	1115	73.00-82.50	9.5	9.05	95.3	
10H	26	1200	82.50-92.00	9.5	6.22	65.5	
11H	26	1310	92.00-101.50	9.5	10.12	106.5	
12H	26	1530	101.50-104.00	2.5	2.55	102.0	
13W	26	1630	104.00-109.50				
14H	26	1705	109.50-119.00	9.5	8.76	92.2	
15H	26	1800	119.00-124.50	5.5	3.96	72.0	
16W	26	1850	124.50-128.80				
17H	26	1930	128.80-138.30	9.5	8.05	84.7	
18H	26	2010	138.30-147.80	9.5	9.23	97.2	
19H	26	2045	147.80-157.30	9.5	9.31	98.0	
20H	26	2325	157.30-160.30	3.0	3.01	100.3	DVTP
21X	27	0055	160.30-167.20	6.9	0.20	2.9	
22X	27	0215	167.20-176.90	9.7	1.18	12.2	
23X	27	0310	176.90-186.50	9.6	0.03	0.3	
24X	27	0410	186.50-196.10	9.6	1.53	15.9	
25X	27	0520	196.10-205.70	9.6	1.21	12.6	
26X	27	0610	205.70-215.30	9.6	0.18	1.9	
27X	27	0700	215.30-224.90	9.6	7.62	79.4	
28X	27	0810	224.90-234.50	9.6	4.04	42.1	
29X	27	0910	234.50-244.10	9.6	2.85	29.7	
30X	27	1030	244.10-248.70	4.6	0.02	0.4	
31X	27	1145	248.70-253.70	5.0	0.19	3.8	
32X	27	1300	253.70-263.30	9.6	1.14	11.9	
Coring totals:				253.5	162.55	64.1	
Washed total:				9.8			
Total:				263.3			
182-1126C-							
1H	27	1545	0.00-8.50	8.5	8.48	99.8	
2H	27	1625	8.50-18.00	9.5	9.52	100.2	
3H	27	1655	18.00-27.50	9.5	9.30	97.9	
4H	27	1800	27.50-37.00	9.5	9.76	102.7	Adara
5H	27	1910	37.00-46.50	9.5	9.64	101.5	
6H	27	2010	46.50-56.00	9.5	9.55	100.5	Adara
7H	27	2045	56.00-65.50	9.5	8.99	94.6	
8H	27	2145	65.50-75.00	9.5	10.29	108.3	Adara
9H	27	2230	75.00-84.50	9.5	9.62	101.3	
10X	27	2255	84.50-90.30	5.8	4.70	81.0	
11X	27	2330	90.30-99.90	9.6	9.09	94.7	
12X	28	0000	99.90-109.50	9.6	7.08	73.8	
13X	28	0025	109.50-119.10	9.6	9.46	98.5	
14X	28	0110	119.10-128.70	9.6	6.06	63.1	
15X	28	0145	128.70-138.40	9.7	6.43	66.3	
16H	28	0215	138.40-144.40	6.0	6.12	102.0	
17X	28	0315	144.40-154.00	9.6	4.43	46.2	
Totals:				154.0	138.52	90.0	
182-1126D-							
			*****Drilled from 0 to 150.0 mbsf*****				
1R	28	1550	150.00-155.90	5.9	0.01	0.2	
2R	28	1630	155.90-165.50	9.6	0.03	0.3	
3R	28	1700	165.50-175.10	9.6	1.37	14.3	
4R	28	1745	175.10-184.70	9.6	0.38	4.0	
5R	28	1830	184.70-194.30	9.6	0.83	8.7	
6R	28	1915	194.30-203.90	9.6	1.01	10.5	
7R	28	2000	203.90-213.50	9.6	0.72	7.5	
8R	28	2040	213.50-223.10	9.6	4.21	43.9	
9R	28	2115	223.10-232.70	9.6	1.17	12.2	
10R	28	2205	232.70-242.30	9.6	0.72	7.5	
11R	28	2300	242.30-251.90	9.6	0.51	5.3	
12R	28	2340	251.90-261.50	9.6	0.80	8.3	
13R	29	0010	261.50-271.20	9.7	0.27	2.8	
14R	29	0035	271.20-280.90	9.7	0.23	2.4	
15R	29	0110	280.90-290.60	9.7	0.30	3.1	

Table T1 (continued).

Core	Date (Oct 1998)	Time (UTC + 8 hr)	Depth (mbsf)	Length cored (m)	Length recovered (m)	Recovery (%)	Comment
16R	29	0150	290.60-300.30	9.7	0.39	4.0	
17R	29	0250	300.30-309.90	9.6	0.17	1.8	
18R	29	0320	309.90-319.30	9.4	0.20	2.1	
19R	29	0350	319.30-328.90	9.6	0.12	1.3	
20R	29	0425	328.90-338.50	9.6	1.01	10.5	
21R	29	0500	338.50-348.10	9.6	0.38	4.0	
22R	29	0530	348.10-357.80	9.7	3.37	34.7	
23R	29	0610	357.80-367.40	9.6	0.08	0.8	
24R	29	0645	367.40-377.00	9.6	2.74	28.5	
25R	29	0720	377.00-386.60	9.6	3.49	36.4	
26R	29	0830	386.60-396.30	9.7	3.80	39.2	
27R	29	0935	396.30-405.90	9.6	0.60	6.3	
28R	29	0240	405.90-415.60	9.7	3.87	39.9	
29R	29	0335	415.60-425.20	9.6	1.02	10.6	
30R	29	0450	425.20-434.80	9.6	2.51	26.1	
31R	29	0550	434.80-444.10	9.3	1.64	17.6	
32R	29	0635	444.10-453.70	9.6	0.31	3.2	
33R	29	0800	453.70-463.30	9.6	2.21	23.0	
Coring totals:				313.3	40.47	12.9	
Drilled total:				150.0			
Total:				463.3			

Note: UTC = Universal Time Coordinated, DVTP = Davis-Villinger temperature probe, Adara = Adara temperature tool.

Table T2. Datum levels used for the calculation of the Site 1126 sedimentation rate.

Datum type	Datum level	Age (Ma)	Midpoint (mbsf)	Stratigraphic error (m)	Fossil group	Datum level code	Upper sample: Leg, hole, core, section, interval (cm)	Upper sample: Depth (mbsf)	Lower sample: Leg, hole, core, section, interval (cm)	Lower sample: Depth (mbsf)
T	*P. lacunosa*	0.41	13.25	4.77	1	1	182-1126C-1H-CC, 9-11	8.46	182-1126C-2H-CC, 8-11	17.99
T	*C. macintyrei*	1.65	51.35	4.71	1	2	182-1126C-5H-CC, 12-15	46.61	182-1126C-6H-CC, 26-29	56.02
T	*D. brouweri*	1.95	60.52	4.47	1	3	182-1126C-6H-CC, 26-29	56.02	182-1126C-7H-CC, 13-16	64.96
T	*R. pseudoumbilicus*	3.83	66.69	0.16	1	4	182-1126B-8H-3, 1-3	66.51	182-1126B-8H-3, 32-34	66.82
B	*Globorotalia puncticulata*	4.20	70.36	5.40	4	5	182-1126C-7H-CC, 13-16	64.96	182-1126C-8H-CC, 43-46	75.76
B	*Globorotalia crassaformis*	4.50	77.49	4.53	4	6	182-1126B-8H-CC, 13-16	72.96	182-1126B-9H-CC, 15-18	82.02
T	*Globoquadrina dehiscens*	5.60	81.88	0.38	4	7	182-1126C-9H-5, 45-50	81.45	182-1126C-9H-5, 120-125	82.20
T	*M. convallis*	7.80	77.52	4.53	1	8	182-1126B-8H-CC, 13-16	72.96	182-1126B-9H-CC, 15-18	82.02
T	*C. miopelagicus*	10.80	111.16	7.11	1	9	182-1126B-12H-CC, 15-20	104.00	182-1126B-14H-CC, 12-15	118.23
T	*S. heteromorphus*	13.60	120.58	2.32	1	10	182-1126B-14H-CC, 12-15	118.23	182-1126B-15H-CC, 0-4	122.85
B	*Orbulina suturalis*	15.10	142.16	5.34	4	11	182-1126B-17H-CC, 13-16	136.82	182-1126B-18H-CC, 21-25	147.49
	Base of C5Cn	16.70	155.70			12				
B	*Globigerinoides sicanus*	16.40	160.38	0.20	4	13	182-1126B-20H-CC, 6-9	160.28	182-1126B-21X-CC, 18-20	160.48
B	*S. heteromorphus*	18.20	172.63	4.28		14	182-1126B-22X-CC, 17-20	168.35	182-1126B-23X-CC, 0-3	176.90
B	*Globoconella praescitula*	18.50	178.18	9.83	4	15	182-1126B-22X-CC, 17-20	168.35	182-1126B-24X-CC, 23-26	188.00
	Top of C7n	24.70	217.80			16				
T	*Globigerina euapertura*	23.80	214.37	8.52	4	17	182-1126B-26X-CC, 15-18	205.85	182-1126B-27X-CC, 28-32	222.88
T	*D. bisectus*	23.90	214.40	8.52	1	18	182-1126B-26X-CC, 15-18	205.85	182-1126B-27X-CC, 28-32	222.88
T	*C. altus*	26.10	233.15	4.21	1	19	182-1126B-28X-CC, 22-25	228.91	182-1126B-29X-CC, 16-20	237.31
T	*Zeaglobigerina labiacrassata*	27.10	251.76	3.06	4	20	182-1126B-31X-CC, 0-1	248.70	182-1126B-32X-CC, 26-28	254.82
T	*Chiloguembelina cubensis*	28.50	286.10	4.90	4	21	182-1126D-15R-CC, 29-30	281.19	182-1126D-16R-CC, 38-39	290.98
T	*Globigerinatheka index*	34.30	334.40	4.48	4	22	182-1126D-20R-CC, 20-22	329.89	182-1126D-21R-CC, 18-19	338.87
B	*I. recurvus*	36.00	345.16	6.29	1	23	182-1126D-21R-CC, 18-19	338.87	182-1126D-22R-CC, 15-17	351.45
T	*Acarinina collactea*	37.70	375.27	5.13	4	24	182-1126D-24R-CC, 30-33	370.11	182-1126D-25R-CC, 15-17	380.38
T	*C. solitus*	40.40	385.40	5.00	1	25	182-1126D-25R-CC, 15-17	380.38	182-1126D-26R-CC, 23-25	390.38
T	*Acarinina primitiva*	39.00	385.40	5.00	4	26	182-1126D-25R-CC, 15-17	380.38	182-1126D-26R-CC, 23-25	390.38
T	*Acarinina bullbrooki*	40.50	393.53	3.13	4	27	182-1126D-26R-CC, 23-25	390.38	182-1126D-27R-CC, 0-2	396.63

Notes: T = top of taxon stratigraphic range, B = bottom of taxon stratigraphic range. Midpoint = the middle depth between the sample where the taxon occurs and the adjacent sample where it does not occur. Stratigraphic error = one-half the distance between the sample where the taxon occurs and the adjacent sample where it does not occur. Datum level code = the number assigned to the datum level on Figure F7, p. 54. Fossil groups = calcareous nannofossils (1) and planktonic foraminifers (4).

Table T3. Core and section depths in meters below seafloor (mbsf) and meters composite depth (mcd), Site 1126. (**See table notes.** Continued on next three pages.)

Leg	Site	Hole	Core	Type	Section	Depth (mbsf)	Offset	Depth (mcd)
182	1126	A	1	H	1	0.00	–0.34	–0.34
182	1126	A	1	H	2	1.44	–0.34	1.10
182	1126	A	1	H	3	2.94	–0.34	2.60
182	1126	A	1	H	4	4.44	–0.34	4.10
182	1126	A	1	H	5	5.94	–0.34	5.60
182	1126	A	1	H	6	7.44	–0.34	7.10
182	1126	A	1	H	7	8.94	–0.34	8.60
182	1126	B	1	H	1	0.00	0.00	0.00
182	1126	B	1	H	2	1.50	0.00	1.50
182	1126	B	1	H	3	3.00	0.00	3.00
182	1126	B	1	H	4	4.50	0.00	4.50
182	1126	B	1	H	5	6.00	0.00	6.00
182	1126	B	2	H	1	6.50	1.39	7.89
182	1126	B	2	H	2	8.00	1.39	9.39
182	1126	B	2	H	3	9.50	1.39	10.89
182	1126	B	2	H	4	11.00	1.39	12.39
182	1126	B	2	H	5	12.50	1.39	13.89
182	1126	B	2	H	6	14.00	1.39	15.39
182	1126	B	3	H	1	16.00	2.68	18.68
182	1126	B	3	H	2	17.50	2.68	20.18
182	1126	B	3	H	3	19.00	2.68	21.68
182	1126	B	3	H	4	20.50	2.68	23.18
182	1126	B	3	H	5	22.00	2.68	24.68
182	1126	B	3	H	6	23.50	2.68	26.18
182	1126	B	3	H	7	25.00	2.68	27.68
182	1126	B	4	H	1	25.50	2.68	28.18
182	1126	B	4	H	2	27.00	2.68	29.68
182	1126	B	4	H	3	28.50	2.68	31.18
182	1126	B	4	H	4	30.00	2.68	32.68
182	1126	B	4	H	5	31.50	2.68	34.18
182	1126	B	4	H	6	33.00	2.68	35.68
182	1126	B	4	H	7	34.50	2.68	37.18
182	1126	B	5	H	1	35.00	3.80	38.80
182	1126	B	5	H	2	36.50	3.80	40.30
182	1126	B	5	H	3	38.00	3.80	41.80
182	1126	B	5	H	4	39.50	3.80	43.30
182	1126	B	5	H	5	41.00	3.80	44.80
182	1126	B	5	H	6	42.50	3.80	46.30
182	1126	B	6	H	1	44.50	4.68	49.18
182	1126	B	6	H	2	46.00	4.68	50.68
182	1126	B	6	H	3	47.50	4.68	52.18
182	1126	B	6	H	4	49.00	4.68	53.68
182	1126	B	6	H	5	50.50	4.68	55.18
182	1126	B	6	H	6	52.00	4.68	56.68
182	1126	B	7	H	1	54.00	5.53	59.53
182	1126	B	7	H	2	55.50	5.53	61.03
182	1126	B	7	H	3	57.00	5.53	62.53
182	1126	B	7	H	4	58.50	5.53	64.03
182	1126	B	7	H	5	60.00	5.53	65.53
182	1126	B	7	H	6	61.50	5.53	67.03
182	1126	B	7	H	7	63.00	5.53	68.53
182	1126	B	8	H	1	63.50	7.18	70.68
182	1126	B	8	H	2	65.00	7.18	72.18
182	1126	B	8	H	3	66.50	7.18	73.68
182	1126	B	8	H	4	68.00	7.18	75.18
182	1126	B	8	H	5	69.50	7.18	76.68
182	1126	B	8	H	6	71.00	7.18	78.18
182	1126	B	8	H	7	72.50	7.18	79.68
182	1126	B	9	H	1	73.00	8.17	81.17
182	1126	B	9	H	2	74.50	8.17	82.67
182	1126	B	9	H	3	76.00	8.17	84.17
182	1126	B	9	H	4	77.50	8.17	85.67
182	1126	B	9	H	5	79.00	8.17	87.17
182	1126	B	9	H	6	80.50	8.17	88.67
182	1126	B	10	H	1	82.50	11.33	93.83
182	1126	B	10	H	2	84.00	11.33	95.33

Table T3 (continued).

Leg	Site	Hole	Core	Type	Section	Depth (mbsf)	Offset	Depth (mcd)
182	1126	B	10	H	3	85.50	11.33	96.83
182	1126	B	10	H	4	87.00	11.33	98.33
182	1126	B	10	H	5	87.60	11.33	98.93
182	1126	B	11	H	1	92.00	10.09	102.09
182	1126	B	11	H	2	93.50	10.09	103.59
182	1126	B	11	H	3	95.00	10.09	105.09
182	1126	B	11	H	4	96.50	10.09	106.59
182	1126	B	11	H	5	98.00	10.09	108.09
182	1126	B	11	H	6	99.50	10.09	109.59
182	1126	B	11	H	7	101.00	10.09	111.09
182	1126	B	12	H	1	101.50	11.67	113.17
182	1126	B	12	H	2	102.73	11.67	114.40
182	1126	B	14	H	1	109.50	14.56	124.06
182	1126	B	14	H	2	111.00	14.56	125.56
182	1126	B	14	H	3	112.50	14.56	127.06
182	1126	B	14	H	4	114.00	14.56	128.56
182	1126	B	14	H	5	115.50	14.56	130.06
182	1126	B	14	H	6	117.00	14.56	131.56
182	1126	B	15	H	1	119.00	14.56	133.56
182	1126	B	15	H	2	120.50	14.56	135.06
182	1126	B	15	H	3	122.00	14.56	136.56
182	1126	B	17	H	1	128.80	13.46	142.26
182	1126	B	17	H	2	130.30	13.46	143.76
182	1126	B	17	H	3	131.80	13.46	145.26
182	1126	B	17	H	4	133.30	13.46	146.76
182	1126	B	17	H	5	134.80	13.46	148.26
182	1126	B	18	H	1	138.30	16.70	155.00
182	1126	B	18	H	2	139.80	16.70	156.50
182	1126	B	18	H	3	141.30	16.70	158.00
182	1126	B	18	H	4	142.80	16.70	159.50
182	1126	B	18	H	5	144.30	16.70	161.00
182	1126	B	18	H	6	145.80	16.70	162.50
182	1126	B	19	H	1	147.80	16.22	164.02
182	1126	B	19	H	2	149.30	16.22	165.52
182	1126	B	19	H	3	150.80	16.22	167.02
182	1126	B	19	H	4	152.30	16.22	168.52
182	1126	B	19	H	5	153.80	16.22	170.02
182	1126	B	19	H	6	155.30	16.22	171.52
182	1126	B	19	H	7	156.30	16.22	172.52
182	1126	B	20	H	1	157.30	16.22	173.52
182	1126	B	20	H	2	158.80	16.22	175.02
182	1126	B	22	X	1	167.20	16.22	183.42
182	1126	B	22	X	2	168.18	16.22	184.40
182	1126	B	24	X	1	186.50	16.22	202.72
182	1126	B	24	X	2	187.77	16.22	203.99
182	1126	B	25	X	1	196.10	16.22	212.32
182	1126	B	27	X	1	215.30	16.22	231.52
182	1126	B	27	X	2	216.80	16.22	233.02
182	1126	B	27	X	3	218.30	16.22	234.52
182	1126	B	27	X	4	219.80	16.22	236.02
182	1126	B	27	X	5	221.30	16.22	237.52
182	1126	B	28	X	1	224.90	16.22	241.12
182	1126	B	28	X	2	226.40	16.22	242.62
182	1126	B	28	X	3	227.90	16.22	244.12
182	1126	B	29	X	1	234.50	16.22	250.72
182	1126	B	29	X	2	236.00	16.22	252.22
182	1126	B	32	X	1	253.70	16.22	269.92
182	1126	C	1	H	1	0.00	0.39	0.39
182	1126	C	1	H	2	1.50	0.39	1.89
182	1126	C	1	H	3	3.00	0.39	3.39
182	1126	C	1	H	4	4.50	0.39	4.89
182	1126	C	1	H	5	6.00	0.39	6.39
182	1126	C	1	H	6	7.50	0.39	7.89
182	1126	C	2	H	1	8.50	1.13	9.63
182	1126	C	2	H	2	10.00	1.13	11.13
182	1126	C	2	H	3	11.50	1.13	12.63
182	1126	C	2	H	4	13.00	1.13	14.13
182	1126	C	2	H	5	14.50	1.13	15.63
182	1126	C	2	H	6	16.00	1.13	17.13

Table T3 (continued).

Leg	Site	Hole	Core	Type	Section	Depth (mbsf)	Offset	Depth (mcd)
182	1126	C	2	H	7	17.50	1.13	18.63
182	1126	C	3	H	1	18.00	1.05	19.05
182	1126	C	3	H	2	19.50	1.05	20.55
182	1126	C	3	H	3	21.00	1.05	22.05
182	1126	C	3	H	4	22.50	1.05	23.55
182	1126	C	3	H	5	24.00	1.05	25.05
182	1126	C	3	H	6	25.50	1.05	26.55
182	1126	C	4	H	1	27.50	2.06	29.56
182	1126	C	4	H	2	29.00	2.06	31.06
182	1126	C	4	H	3	30.50	2.06	32.56
182	1126	C	4	H	4	32.00	2.06	34.06
182	1126	C	4	H	5	33.50	2.06	35.56
182	1126	C	4	H	6	35.00	2.06	37.06
182	1126	C	4	H	7	36.50	2.06	38.56
182	1126	C	5	H	1	37.00	4.40	41.40
182	1126	C	5	H	2	38.50	4.40	42.90
182	1126	C	5	H	3	40.00	4.40	44.40
182	1126	C	5	H	4	41.50	4.40	45.90
182	1126	C	5	H	5	43.00	4.40	47.40
182	1126	C	5	H	6	44.50	4.40	48.90
182	1126	C	5	H	7	46.00	4.40	50.40
182	1126	C	6	H	1	46.50	4.30	50.80
182	1126	C	6	H	2	48.00	4.30	52.30
182	1126	C	6	H	3	49.50	4.30	53.80
182	1126	C	6	H	4	51.00	4.30	55.30
182	1126	C	6	H	5	52.50	4.30	56.80
182	1126	C	6	H	6	54.00	4.30	58.30
182	1126	C	6	H	7	55.00	4.30	59.30
182	1126	C	7	H	1	56.00	6.04	62.04
182	1126	C	7	H	2	57.50	6.04	63.54
182	1126	C	7	H	3	59.00	6.04	65.04
182	1126	C	7	H	4	60.50	6.04	66.54
182	1126	C	7	H	5	62.00	6.04	68.04
182	1126	C	7	H	6	63.50	6.04	69.54
182	1126	C	8	H	1	65.50	6.04	71.54
182	1126	C	8	H	2	67.00	6.04	73.04
182	1126	C	8	H	3	68.50	6.04	74.54
182	1126	C	8	H	4	70.00	6.04	76.04
182	1126	C	8	H	5	71.50	6.04	77.54
182	1126	C	8	H	6	73.00	6.04	79.04
182	1126	C	8	H	7	74.50	6.04	80.54
182	1126	C	9	H	1	75.00	8.51	83.51
182	1126	C	9	H	2	76.50	8.51	85.01
182	1126	C	9	H	3	78.00	8.51	86.51
182	1126	C	9	H	4	79.50	8.51	88.01
182	1126	C	9	H	5	81.00	8.51	89.51
182	1126	C	9	H	6	82.50	8.51	91.01
182	1126	C	9	H	7	83.50	8.51	92.01
182	1126	C	10	X	2	86.00	8.51	94.51
182	1126	C	10	X	3	87.50	8.51	96.01
182	1126	C	11	X	1	90.30	8.83	99.13
182	1126	C	11	X	2	91.80	8.83	100.63
182	1126	C	11	X	3	93.30	8.83	102.13
182	1126	C	11	X	4	94.80	8.83	103.63
182	1126	C	11	X	5	96.30	8.83	105.13
182	1126	C	11	X	6	97.80	8.83	106.63
182	1126	C	12	X	1	99.90	10.35	110.25
182	1126	C	12	X	2	101.40	10.35	111.75
182	1126	C	12	X	3	102.90	10.35	113.25
182	1126	C	12	X	4	104.40	10.35	114.75
182	1126	C	12	X	5	105.90	10.35	116.25
182	1126	C	13	X	1	109.50	7.34	116.84
182	1126	C	13	X	2	111.00	7.34	118.34
182	1126	C	13	X	3	112.50	7.34	119.84
182	1126	C	13	X	4	114.00	7.34	121.34
182	1126	C	13	X	5	115.50	7.34	122.84
182	1126	C	13	X	6	117.00	7.34	124.34
182	1126	C	13	X	7	118.00	7.34	125.34
182	1126	C	14	X	1	119.10	13.84	132.94

Table T3 (continued).

Leg	Site	Hole	Core	Type	Section	Depth (mbsf)	Offset	Depth (mcd)
182	1126	C	14	X	2	120.60	13.84	134.44
182	1126	C	14	X	3	122.10	13.84	135.94
182	1126	C	14	X	4	123.60	13.84	137.44
182	1126	C	15	X	1	128.70	15.70	144.40
182	1126	C	15	X	2	130.20	15.70	145.90
182	1126	C	15	X	3	131.70	15.70	147.40
182	1126	C	15	X	4	133.20	15.70	148.90
182	1126	C	15	X	5	134.20	15.70	149.90
182	1126	C	16	H	1	138.40	14.94	153.34
182	1126	C	16	H	2	139.90	14.94	154.84
182	1126	C	16	H	3	141.40	14.94	156.34
182	1126	C	16	H	4	142.90	14.94	157.84
182	1126	C	17	X	1	144.40	14.94	159.34
182	1126	C	17	X	2	145.90	14.94	160.84
182	1126	C	17	X	3	147.40	14.94	162.34

Notes: Depths are measured at the top of each section. This table is also available in **ASCII format.**

Table T4. Biostratigraphic data used for splice correlation, Site 1126.

Datum	Taxon	Age (Ma)	Leg, hole, core, section, interval (cm)	Depth (mbsf)	Leg, hole, core, section, interval (cm)	Depth (mbsf)
FAD	*Globorotalia truncatulinoides*	2	182-1126C-4H-CC, 16	37.23	182-1126B-9-H-CC, 15	82.02
FAD	*G. truncatulinoides*	2	182-1126B-4H-CC, 5	35.03	182-1126B-9-H-CC, 15	81.87
LAD	*Globorotalia margaritae*	3.58	182-1126C-6H-CC, 26	56.02	182-1126C-8-H-CC, 43	75.76
FAD	*Globorotalia puncticulata*	4.2	182-1126C-7H-CC, 16	64.96	182-1126C-9-H-CC, 50	81.45
FAD	*G. puncticulata*	4.2	182-1126B-8H-CC, 13	72.96	182-1126B-8-H-CC, 13	72.96
FAD	*Globorotalia crassaformis*	4.5	182-1126B-8H-CC, 18	72.96	182-1126C-11-X-CC, 16	99.36
FAD	*G. crassaformis*	4.5	182-1126C-7H-CC, 13	64.96	182-1126C-12-X-CC, 18	106.96
LAD	*Globoquadrina dehiscens*	5.6	182-1126C-9H-5, 120	82.20	182-1126B-12-H-CC, 15	104.00
LAD	*G. dehiscens*	5.6	182-1126B-9H-CC, 15	82.02	182-1126B-18-H-CC, 21	147.49
FAD	*Zeaglobigerina nepenthes*	11.8	182-1126C-10X-CC, 20	89.17	182-1126B-22-H-CC, 17	168.35
LAD	*Fohsella peripheroronda*	14.6	182-1126C-12X-CC, 18	106.96	182-1126C-16-H-CC, 10	144.50
LAD	*F. peripheroronda*	14.6	182-1126B-14H-CC, 12	118.23	182-1126B-12-H-CC, 15	104.00
LAD	*Orbulina suturalis*	15.1	182-1126B-18H-CC, 21	147.49	182-1126B-18-H-CC, 21	147.49
LAD	*Globoconella praescitula*	18.5	182-1126B-24X-CC, 23	188.00	182-1126B-24-X-CC, 23	188.00

Note: FAD = first appearance datum, LAD = last appearance datum.

Table T5. Splice tie points, Site 1126.

Site	Hole	Core	Type	Section	Interval (cm)	Depth (mbsf)	Depth (mcd)		Site	Hole	Core	Type	Section	Interval (cm)	Depth (mbsf)	Depth (mcd)
1126	B	1	H	3	100	4.00	4.00	Tie to	1126	C	1	H	3	60	3.61	4.00
1126	C	1	H	6	19	7.69	8.08	Tie to	1126	B	2	H	1	19	6.69	8.08
1126	B	2	H	3	76	10.26	11.65	Tie to	1126	C	2	H	2	52	10.52	11.65
1126	C	2	H	7	32	17.82	18.95	Tie to	1126	B	3	H	1	27	16.27	18.95
1126	B	3	H	1	80	16.80	19.48	Tie to	1126	C	3	H	1	43	18.43	19.48
1126	C	3	H	6	144	26.94	27.99	Append to	1126	B	4	H	1	0	25.50	28.18
1126	B	4	H	4	75	30.75	33.43	Tie to	1126	C	4	H	3	87	31.37	33.43
1126	C	4	H	7	44	36.94	39.00	Tie to	1126	B	5	H	1	16	35.20	39.00
1126	B	5	H	6	80	43.30	47.10	Tie to	1126	C	5	H	4	120	42.70	47.10
1126	C	5	H	7	24	46.24	50.64	Tie to	1126	B	6	H	1	145	45.96	50.64
1126	B	6	H	4	36	49.36	54.04	Tie to	1126	C	6	H	3	24	49.74	54.04
1126	C	6	H	7	35	55.35	59.65	Tie to	1126	B	7	H	1	11	54.12	59.65
1126	B	7	H	5	107	61.07	66.60	Tie to	1126	C	7	H	4	6	60.56	66.60
1126	C	7	H	6	128	64.78	70.82	Append to	1126	C	8	H	1	0	65.50	71.54
1126	C	8	H	7	80	75.30	81.34	Append to	1126	B	9	H	1	0	73.00	81.17
1126	B	9	H	4	35	77.85	86.02	Tie to	1126	C	9	H	2	100	77.51	86.02
1126	C	9	H	7	88	84.38	92.89	Append to	1126	C	10	X	1	0	84.50	93.01
1126	C	10	X	3	40	87.90	96.41	Tie to	1126	B	10	H	2	108	85.08	96.41
1126	B	10	H	5	92	88.52	99.85									

Note: This table is also available in **ASCII format.**

Table T6. Composition of hydrocarbon gases, Site 1126.

Core, section	Depth (mbsf)	Sample method	C_1 (ppmv)	C_2 (ppmv)	C_1/C_2
182-1126A-					
1H-5	5.9	HS	13.6		
182-1126B-					
2H-5	12.50	HS	3.2		
3H-4	20.50	HS	3.9		
4H-5	31.50	HS	5.0		
5H-5	41.00	HS	7.2		
6H-5	50.50	HS	4.6		
7H-5	60.00	HS	8.2		
8H-5	69.50	HS	5.0		
9H-5	79.00	HS	6.8		
10H-3	85.50	HS	5.4		
11H-4	97.27	VAC	31.8	1.3	24.5
11H-5	98.00	HS	8.3		
14H-4	114.00	HS	12.1		
15H-2	120.50	HS	6.3		
17H-5	134.80	HS	8.3		
18H-3	141.30	HS	7.8		
19H-5	153.80	HS	7.6		
22X-1	167.20	HS	7.3		
24X-1	186.50	HS	11.3	1.1	10.3
25X-1	197.10	HS	8.6	1.2	7.2
27X-5	221.30	HS	12.0	2.7	4.4
28X-2	226.40	HS	9.2	2.1	4.4
29X-2	236.00	HS	8.5	2.1	4.1
32X-1	253.70	HS	2.7		
182-1126D-					
12R-1	252.45	HS	3.8		
20R-1	328.90	HS	2.7		
21R-1	338.68	HS	2.8		
22R-3	350.60	HS	2.3		
24R-1	367.40	HS	2.6		
25R-3	379.83	HS	2.2		
26R-2	387.65	HS	2.5		
27R-1	396.62	HS	5.0		
28R-3	408.84	HS	3.3		
29R-1	415.60	HS	2.3		
30R-2	426.29	HS	2.4		
31R-1	436.18	HS	2.3		
33R-1	453.70	HS	5.4		

Note: HS = headspace, VAC = vacutainer, blank = not detected.

Table T7. Calcium carbonate, organic carbon, nitrogen, and sulfur data, Site 1126. (See table note. Continued on next page.)

Core, section, interval (cm)	Depth (mbsf)	$CaCO_3$ (wt%)	C_{org} (wt%)	N (wt%)	S (wt%)
182-1126B-					
1H-1, 49-50	0.49	88.2	0.81	0.07	0.3
1H-3, 49-50	3.49	90.4	0.53	0.06	0.27
2H-1, 48-49	6.98	89.1	0.43		0.28
2H-3, 48-49	9.98	90.0	0.46		0.24
2H-5, 48-49	12.98	88.6	0.48		0.17
3H-1, 48-49	16.48	88.8	0.56		0.25
3H-3, 48-49	19.48	87.0	0.70		0.17
3H-5, 48-49	22.48	84.9	0.69		0.26
4H-1, 49-50	25.99	87.5	0.39		0.11
4H-3, 49-50	28.99	84.2	0.49		0.22
4H-5, 49-50	31.99	85.6	0.28		0.2
5H-1, 48-49	35.48	86.2	0.38		0.26
5H-3, 48-49	38.48	86.4	0.26		0.29
5H-5, 48-49	41.48	83.0	0.54		
6H-1, 47-48	44.97	85.6	0.55		0.29
6H-3, 47-48	47.97	88.0	0.31		0.15
6H-5, 47-48	50.97	85.6	0.22		0.28
7H-1, 48-49	54.48	91.2	0.03		0.18
7H-3, 48-49	57.48	88.7	0.05		
7H-5, 48-49	60.48	86.5	0.12		
8H-1, 48-49	63.98	90.7	0.53		0.1
8H-3, 49-49	66.98	88.1	0.25		0.12
5H-5, 48-49	69.98	89.1			
9H-1, 48-49	73.48	88.2	0.38		0.14
9H-3, 48-49	76.48	84.2			
9H-5, 48-49	79.48	86.6	0.13		0.13
10H-3, 49-50	85.99	85.5	0.62		
10H-5, 49-50	88.09	88.9	0.10		
11H-1, 48-50	92.48	83.9			0.09
11H-3, 48-50	95.48	83.5	0.18		
11H-5, 48-50	98.48	79.9			0.13
12H-1, 49-50	101.99	84.2	0.10		
14H-3, 49-50	112.99	82.6	0.16		
14H-5, 49-50	115.99	88.8			
15H-1, 64-65	119.64	76.1	0.41	0.09	
17H-3, 48-49	132.28	82.0	0.09		
17H-5, 48-49	135.28	58.2			0.16
18H-3, 48-49	141.78	89.1	0.07		
18H-5, 48-49	144.78	85.5	0.23		
19H-1, 48-49	148.28	59.2			
19H-3, 48-49	151.28	66.8			
19H-5, 48-49	154.28	53.3	0.03		0.13
22X-1, 48-49	167.68	59.1			
24X-1, 48-49	186.98	80.3	0.08		
25X-1, 45-46	196.55	91.2	0.19		0.01
27X-1, 48-49	215.78	74.2	0.19		
27X-3, 48-49	218.78	71.9	0.16		
27X-5, 49-50	221.79	73.0	0.07		
28X-1, 47-48	225.37	88.0			
28X-3, 47-48	228.37	68.0			
29X-1, 46-47	234.96	84.9	0.12		
32X-1, 47-48	254.17	93.2			
182-1126D-					
3R-1, 71-72	166.21	80.9	0.18		
4R-CC, 13-14	175.23	45.0			
5R-1, 17-19	184.87	47.0			
6R-1, 41-44	194.71	33.9			
7R-1, 38-39	204.28	30.6			
8R-1, 48-49	213.98	73.9	0.44		
8R-3, 48-49	216.98	66.6	0.30		
12R-1, 49-50	252.39	91.6	0.31		
22R-1, 49-50	348.59	90.0			
22R-3, 49-50	351.09	85.2	0.04		
24R-1, 49-50	367.89	84.1	0.19		
24R-2, 49-50	369.39	89.1			

Table T7 (continued).

Core, section, interval (cm)	Depth (mbsf)	$CaCO_3$ (wt%)	C_{org} (wt%)	N (wt%)	S (wt%)
25R-1, 49-50	377.49	84.4	0.10		
26R-1, 48-49	387.08	79.5	0.14		
26R-3, 48-49	389.63	85.0	0.11		
28R-1, 48-49	406.38	0.5	0.86	0.05	1.62
28R-3, 48-49	409.32	69.3	0.40		
29R-1, 34-35	415.94	0.4	0.76	0.04	
30R-2, 66-68	426.95	0.5	0.79	0.04	0.11
31R-1, 48-49	435.28	0.6	0.41		0.35
33R-1, 80-81	454.50	0.6	1.33	0.1	

Note: Blank = not detected.

Table T8. Interstitial water geochemistry, Site 1126.

Core, section, interval (cm)	Depth (mbsf)	pH	ppH	Alkalinity (mM)	Salinity	Cl^- (mM)	Cl^- (IC)	Na^+ (mM)	K^+ (mM)	Mg^{2+} (mM)	Ca^{2+} (mM)	$H_4SiO_4^0$ (µM)	SO_4^{2-} (mM)	Sr^{2+} (µM)	Li^+ (µM)
SSW	0			2.4		575	539	521	10.8	57.4	11.7		30.3	93	33
182-1126A-															
1H-2, 145-150	2.95	7.11	7.66	4.05	36.0	577	543	528	11.1	55.9	10.7	544	28.4	113	33
182-1126B-															
1H-3, 145-150	4.45	7.35	7.56	4.02	35.5	581	554	520	11.2	53.6	11.5	544	27.9	109	42
182-1126A-															
1H-4, 145-150	5.95	7.58	7.66	4.25	36.0	594	531	532	11.2	57.1	11.5	516	29.3	111	35
182-1126B-															
2H-2, 140-150	9.40	7.08	7.51	3.55	36.7	617	576	559	12.5	58.5	11.1	561	29.4	128	34
2H-4, 140-150	12.40	7.10	7.51	3.72	40.0	648	603	582	12.6	61.1	11.8	571	30.7	126	35
3H-2, 140-150	18.90	6.89	7.19	3.40	50.0	813	766	728	14.5	79.6	16.7	584	42.5	237	39
3H-4, 140-150	21.90	6.89	7.13	4.98	56.0	909	864	815	15.9	89.6	19.7	580	48.8	277	43
4H-2, 140-150	28.40	6.95	6.98	5.10	68.0	1078	1025	945	17.3	103.3	25.7	569	58.6	302	51
4H-4, 140-150	31.45	6.82	6.81	4.98	72.0	1145	1097	1007	18.4	107.2	27.5	590	62.0	295	55
5H-2, 140-150	37.90	6.77	6.72	4.37	81.0	1285	1230	1132	22.0	112.6	32.4	596	64.1	267	59
5H-4, 140-150	40.90	6.84	6.75	4.40	84.0	1341	1303	1187	22.1	116.3	39.1	628	67.0	266	62
6H-4, 140-150	50.40	6.79	6.76	3.34	92.0	1478	1445	1302	24.5	122.0	40.4	575	67.7	217	66
7H-4, 140-150	59.90	6.50	6.92	3.30	96.0	1570	1553	1391	28.0	125.6	43.8	434	68.5	280	74
8H-4, 140-150	69.40	6.58	6.90	2.66	100.0	1630	1630	1454	29.0	127.2	45.3	398	70.1	218	72
10H-2, 140-150	85.40	6.75	6.91	2.46	100.0	1652	1600	1431	32.2	124.7	45.1	565	65.2	198	71
14H-3, 140-150	113.90	6.81	7.00	2.40	105.0	1734	1714	1524	33.3	130.2	48.1	644	67.6	198	67
17H-4, 140-150	134.70	6.80	7.10	3.41	106.0	1744	1751	1543	31.2	130.9	49.7	659	68.5	193	73
19H-4, 140-150	153.70	7.06	7.35	2.30	106.0	1731	1738	1528	31.1	128.9	48.2	723	68.0	198	52
24X-1, 117-127	187.67	7.18	7.22	1.92	96.0	1586	1594	1419	28.9	120.9	43.0	615	63.4	200	50
182-1126D-															
8R-2, 140-150	216.40	7.15		1.66	96	1580	1512	1365	26.7	111.3	37.9		59.1	339	90
182-1126B-															
27X-4, 140-150	221.20	7.07	7.24	2.42	102.5	1685	1689	1491	30.2	126.2	46.8	788	66.0	211	55
29X-1, 140-150	235.90	7.02	7.18	1.95	102.0	1690	1718	1537	33.7	127.3	47.3	758	67.6	204	34
182-1126D-															
22R-1, 0-10	349.50	6.96		1.83	100	1616	1572	1409	26.9	115.2	43.5		62.4	269	119
24R-1, 0-10	367.40	7.24		1.02	102	1697	1647	1480	27.9	118.0	45.6		64.5	259	123
26R-1, 0-10	386.60	6.71			92	1510	1464	1315	25.0	107.8	42.5		58.2	238	107
28R-2, 140-150	408.74	7.42		2.97	97	1579	1554	1410	27.4	110.7	46.2		62.4	259	114

Note: SSW = surface seawater.

Table T9. Summary of X-ray diffraction analysis, Site 1126. (See table notes. Continued on next page.)

Leg	Site	Hole	Core	Type	Section	Top (cm)	Bottom (cm)	Depth (mbsf)	Aragonite (%)	Quartz (%)	LMC (%)	HMC (%)	Dolomite (%)
182	1126	B	1	H	1	49	50	0.49	18	1	32	47	2
182	1126	B	1	H	3	49	50	3.49	17	1	29	54	0
182	1126	B	2	H	1	48	49	6.98	20	1	41	36	1
182	1126	B	2	H	3	48	49	9.98	20	1	38	40	1
182	1126	B	2	H	5	48	49	12.98	17	1	44	37	2
182	1126	B	3	H	1	48	49	16.48	13	1	48	38	0
182	1126	B	3	H	3	48	49	19.48	17	1	48	32	1
182	1126	B	3	H	5	48	49	22.48	27	1	72	0	0
182	1126	B	4	H	1	49	50	25.99	18	1	81	0	0
182	1126	B	4	H	3	49	50	28.99	26	1	71	0	2
182	1126	B	4	H	5	49	50	31.99	18	2	78	0	2
182	1126	B	5	H	1	48	49	35.48	22	1	75	0	2
182	1126	B	5	H	3	48	49	38.48	19	1	78	0	2
182	1126	B	5	H	5	48	49	41.48	23	2	70	0	6
182	1126	B	6	H	1	47	48	44.97	14	1	81	0	5
182	1126	B	6	H	3	47	48	47.97	21	1	76	0	2
182	1126	B	6	H	5	47	48	50.97	23	2	74	0	1
182	1126	B	7	H	1	48	49	54.48	5	1	93	0	1
182	1126	B	7	H	3	48	49	57.48	7	1	92	0	0
182	1126	B	7	H	5	48	49	60.48	15	1	82	0	2
182	1126	B	8	H	1	48	49	63.98	13	0	85	0	1
182	1126	B	8	H	3	48	49	66.98	0	1	99	0	0
182	1126	B	8	H	5	48	49	69.98	0	1	99	0	0
182	1126	B	9	H	1	48	49	73.48	3	1	96	0	0
182	1126	B	9	H	3	48	49	76.48	0	4	96	0	0
182	1126	B	9	H	5	48	49	79.48	0	3	97	0	0
182	1126	B	10	H	3	49	50	85.99	0	4	96	0	0
182	1126	B	10	H	5	49	50	88.09	0	1	99	0	0
182	1126	B	11	H	1	48	50	92.48	0	1	99	0	0
182	1126	B	11	H	3	48	50	95.48	0	0	100	0	0
182	1126	B	11	H	5	48	50	98.48	0	2	98	0	0
182	1126	B	12	H	1	49	50	101.99	0	1	99	0	0
182	1126	B	14	H	3	49	50	112.99	0	1	99	0	0
182	1126	B	14	H	5	49	50	115.99	0	0	100	0	0
182	1126	B	15	H	1	64	65	119.64	0	0	100	0	0
182	1126	B	17	H	3	48	49	132.28	0	0	100	0	0
182	1126	B	17	H	5	48	49	135.28	0	2	98	0	0
182	1126	B	18	H	3	48	49	141.78	0	0	100	0	0
182	1126	B	18	H	5	48	49	144.78	0	1	99	0	0
182	1126	B	19	H	1	48	49	148.28	0	2	98	0	0
182	1126	B	19	H	3	48	49	151.28	0	2	98	0	0
182	1126	B	19	H	5	48	49	154.28	0	2	98	0	0
182	1126	B	22	X	1	48	49	167.68	0	3	97	0	0
182	1126	B	24	X	1	48	49	186.98	0	0	100	0	0
182	1126	B	25	X	1	45	46	196.55	0	0	99	0	1
182	1126	B	27	X	1	48	49	215.78	0	1	99	0	0
182	1126	B	27	X	3	48	49	218.78	0	1	99	0	0
182	1126	B	27	X	5	49	50	221.79	0	1	99	0	0
182	1126	B	28	X	1	47	48	225.37	0	1	99	0	0
182	1126	B	28	X	3	47	48	228.37	0	2	98	0	0
182	1126	B	29	X	1	46	47	234.96	0	0	100	0	0
182	1126	B	32	X	1	47	48	254.17	0	0	100	0	0
182	1126	D	3	R	1	71	72	166.21	0	1	99	0	1
182	1126	D	4	R	CC	13	14	175.23	0	12	88	0	0
182	1126	D	5	R	1	17	19	184.87	0	11	89	0	0
182	1126	D	6	R	1	41	44	194.71	0	24	76	0	0
182	1126	D	7	R	1	38	39	204.28	0	25	75	0	0
182	1126	D	8	R	1	48	49	213.98	0	1	99	0	0
182	1126	D	8	R	3	48	49	216.98	0	1	98	0	0
182	1126	D	12	R	1	49	50	252.39	0	1	99	0	0
182	1126	D	22	R	1	49	50	348.59	0	0	100	0	0
182	1126	D	22	R	3	49	50	351.09	0	1	99	0	0
182	1126	D	24	R	1	49	50	367.89	0	1	99	0	0
182	1126	D	24	R	2	49	50	369.39	0	1	99	0	0
182	1126	D	25	R	1	49	50	377.49	0	1	98	0	0
182	1126	D	26	R	1	48	49	387.08	0	1	99	0	0
182	1126	D	26	R	3	48	49	389.63	0	1	98	0	1
182	1126	D	28	R	1	48	49	406.38	0	100	0	0	0
182	1126	D	28	R	3	48	49	409.32	0	0	100	0	0

Table T9 (continued).

Leg	Site	Hole	Core	Type	Section	Top (cm)	Bottom (cm)	Depth (mbsf)	Aragonite (%)	Quartz (%)	LMC (%)	HMC (%)	Dolomite (%)
182	1126	D	29	R	1	34	35	415.94	0	98	2	0	0
182	1126	D	30	R	2	66	68	426.95	0	96	4	0	0
182	1126	D	31	R	1	48	49	435.28	0	98	2	0	0
182	1126	D	33	R	1	80	81	454.50	0	95	5	0	0

Notes: LMC = low-Mg calcite, HMC = high-Mg calcite. This table is also available in **ASCII format.**

Table T10. *P*-wave velocity measurements from the multisensor track, Site 1126.

Leg	Site	Hole	Core	Type	Section	Interval (cm)	Depth (mbsf)	V_p (km/s)
182	1126	A	1	H	1	3.0	0.03	3.0425
182	1126	A	1	H	1	7.0	0.07	3.9388
182	1126	A	1	H	1	11.0	0.11	3.8996
182	1126	A	1	H	1	15.0	0.15	3.8732
182	1126	A	1	H	1	19.0	0.19	3.8915
182	1126	A	1	H	1	23.0	0.23	3.8687
182	1126	A	1	H	1	27.0	0.27	3.8709
182	1126	A	1	H	1	31.0	0.31	1.6456
182	1126	A	1	H	1	35.0	0.35	1.7836
182	1126	A	1	H	1	39.0	0.39	1.8580
182	1126	A	1	H	1	43.0	0.43	1.5851
182	1126	A	1	H	1	47.0	0.47	2.7200
182	1126	A	1	H	1	51.0	0.51	1.5596
182	1126	A	1	H	1	63.0	0.63	3.9498
182	1126	A	1	H	1	91.0	0.91	2.1284
182	1126	A	1	H	1	95.0	0.95	2.5060
182	1126	A	1	H	1	99.0	0.99	2.3941
182	1126	A	1	H	1	103.0	1.03	3.1290
182	1126	A	1	H	1	107.0	1.07	3.2349
182	1126	A	1	H	1	115.0	1.15	1.6817
182	1126	A	1	H	1	119.0	1.19	1.9422
182	1126	A	1	H	1	123.0	1.23	2.0857
182	1126	A	1	H	1	127.0	1.27	1.8217
182	1126	A	1	H	1	131.0	1.31	2.0344
182	1126	A	1	H	1	135.0	1.35	3.5784
182	1126	A	1	H	1	139.0	1.39	3.9304
182	1126	A	1	H	2	3.0	1.47	3.0483
182	1126	A	1	H	2	7.0	1.51	3.8962
182	1126	A	1	H	2	11.0	1.55	3.8768
182	1126	A	1	H	2	15.0	1.59	2.2369
182	1126	A	1	H	2	19.0	1.63	2.2048
182	1126	A	1	H	2	23.0	1.67	3.3515
182	1126	A	1	H	2	27.0	1.71	2.2960
182	1126	A	1	H	2	31.0	1.75	1.8379
182	1126	A	1	H	2	35.0	1.79	1.5754
182	1126	A	1	H	2	39.0	1.83	3.0926
182	1126	A	1	H	2	59.0	2.03	2.0072
182	1126	A	1	H	2	67.0	2.11	1.6206
182	1126	A	1	H	2	83.0	2.27	3.1128
182	1126	A	1	H	2	87.0	2.31	2.7144
182	1126	A	1	H	2	91.0	2.35	2.6426
182	1126	A	1	H	2	95.0	2.39	1.6522
182	1126	A	1	H	2	99.0	2.43	2.3332
182	1126	A	1	H	2	103.0	2.47	1.8680
182	1126	A	1	H	2	107.0	2.51	2.6955
182	1126	A	1	H	2	111.0	2.55	2.7984
182	1126	A	1	H	2	115.0	2.59	1.9079
182	1126	A	1	H	2	119.0	2.63	2.0091
182	1126	A	1	H	2	123.0	2.67	2.0301
182	1126	A	1	H	2	127.0	2.71	1.8802
182	1126	A	1	H	2	131.0	2.75	2.7010
182	1126	A	1	H	2	135.0	2.79	2.7819
182	1126	A	1	H	2	139.0	2.83	3.4943
182	1126	A	1	H	3	3.0	2.97	3.1610
182	1126	A	1	H	3	7.0	3.01	3.9215
182	1126	A	1	H	3	11.0	3.05	3.5753
182	1126	A	1	H	3	15.0	3.09	3.8836
182	1126	A	1	H	3	19.0	3.13	3.8973
182	1126	A	1	H	3	23.0	3.17	3.8893
182	1126	A	1	H	3	27.0	3.21	3.8688
182	1126	A	1	H	3	31.0	3.25	3.5760
182	1126	A	1	H	3	35.0	3.29	3.8620
182	1126	A	1	H	3	39.0	3.33	2.8559
182	1126	A	1	H	3	43.0	3.37	1.7406

Note: Only a portion of this table appears here. The complete table is available in **ASCII format.**

Table T11. Gamma-ray attenuation densiometry measurements from the multisensor track, Site 1126.

Leg	Site	Hole	Core	Type	Section	Interval (cm)	Depth (mbsf)	Density (g/cm^3)	Corrected density (g/cm^3)
182	1126	A	1	H	1	3.0	0.03	1.76	1.70
182	1126	A	1	H	1	7.0	0.07	1.73	1.66
182	1126	A	1	H	1	11.0	0.11	1.76	1.70
182	1126	A	1	H	1	15.0	0.15	1.78	1.72
182	1126	A	1	H	1	19.0	0.19	1.78	1.72
182	1126	A	1	H	1	23.0	0.23	1.78	1.72
182	1126	A	1	H	1	27.0	0.27	1.77	1.71
182	1126	A	1	H	1	31.0	0.31	1.76	1.69
182	1126	A	1	H	1	35.0	0.35	1.73	1.67
182	1126	A	1	H	1	39.0	0.39	1.76	1.70
182	1126	A	1	H	1	43.0	0.43	1.76	1.70
182	1126	A	1	H	1	47.0	0.47	1.75	1.68
182	1126	A	1	H	1	51.0	0.51	1.76	1.70
182	1126	A	1	H	1	55.0	0.55	1.79	1.73
182	1126	A	1	H	1	59.0	0.59	1.78	1.72
182	1126	A	1	H	1	63.0	0.63	1.77	1.71
182	1126	A	1	H	1	67.0	0.67	1.77	1.71
182	1126	A	1	H	1	71.0	0.71	1.76	1.70
182	1126	A	1	H	1	75.0	0.75	1.76	1.70
182	1126	A	1	H	1	79.0	0.79	1.77	1.71
182	1126	A	1	H	1	83.0	0.83	1.76	1.70
182	1126	A	1	H	1	87.0	0.87	1.77	1.70
182	1126	A	1	H	1	91.0	0.91	1.74	1.68
182	1126	A	1	H	1	95.0	0.95	1.77	1.71
182	1126	A	1	H	1	99.0	0.99	1.79	1.73
182	1126	A	1	H	1	103.0	1.03	1.76	1.70
182	1126	A	1	H	1	107.0	1.07	1.77	1.70
182	1126	A	1	H	1	111.0	1.11	1.78	1.72
182	1126	A	1	H	1	115.0	1.15	1.76	1.70
182	1126	A	1	H	1	119.0	1.19	1.75	1.69
182	1126	A	1	H	1	123.0	1.23	1.79	1.73
182	1126	A	1	H	1	127.0	1.27	1.76	1.70
182	1126	A	1	H	1	131.0	1.31	1.73	1.67
182	1126	A	1	H	1	135.0	1.35	1.72	1.66
182	1126	A	1	H	1	139.0	1.39	1.74	1.67
182	1126	A	1	H	2	3.0	1.47	1.77	1.71
182	1126	A	1	H	2	7.0	1.51	1.80	1.74
182	1126	A	1	H	2	11.0	1.55	1.79	1.73
182	1126	A	1	H	2	15.0	1.59	1.79	1.73
182	1126	A	1	H	2	19.0	1.63	1.77	1.71
182	1126	A	1	H	2	23.0	1.67	1.76	1.70
182	1126	A	1	H	2	27.0	1.71	1.79	1.73
182	1126	A	1	H	2	31.0	1.75	1.76	1.70
182	1126	A	1	H	2	35.0	1.79	1.76	1.69
182	1126	A	1	H	2	39.0	1.83	1.78	1.72
182	1126	A	1	H	2	43.0	1.87	1.78	1.72
182	1126	A	1	H	2	47.0	1.91	1.78	1.72
182	1126	A	1	H	2	51.0	1.95	1.79	1.73
182	1126	A	1	H	2	55.0	1.99	1.77	1.71
182	1126	A	1	H	2	59.0	2.03	1.76	1.70
182	1126	A	1	H	2	63.0	2.07	1.75	1.69
182	1126	A	1	H	2	67.0	2.11	1.74	1.68
182	1126	A	1	H	2	71.0	2.15	1.77	1.71
182	1126	A	1	H	2	75.0	2.19	1.72	1.66
182	1126	A	1	H	2	79.0	2.23	1.77	1.71
182	1126	A	1	H	2	83.0	2.27	1.80	1.74
182	1126	A	1	H	2	87.0	2.31	1.74	1.68
182	1126	A	1	H	2	91.0	2.35	1.78	1.72
182	1126	A	1	H	2	95.0	2.39	1.76	1.70
182	1126	A	1	H	2	99.0	2.43	1.75	1.69
182	1126	A	1	H	2	103.0	2.47	1.79	1.73
182	1126	A	1	H	2	107.0	2.51	1.74	1.68
182	1126	A	1	H	2	111.0	2.55	1.72	1.66

Note: Only a portion of this table appears here. The complete table is available in **ASCII format.**

Table T12. Magnetic susceptibility measurements from the multisensor track, Site 1126.

Leg	Site	Hole	Core	Type	Section	Interval (cm)	Depth (mbsf)	Magnetic susceptibility (10^{-6}; SI units)	Corrected susceptibility (10^{-6}; SI units)
182	1126	A	1	H	1	3.0	0.03	–1.6	–1.6
182	1126	A	1	H	1	11.0	0.11	–1.9	–1.9
182	1126	A	1	H	1	19.0	0.19	–2.8	–2.8
182	1126	A	1	H	1	27.0	0.27	–2.9	–2.9
182	1126	A	1	H	1	35.0	0.35	–3.5	–3.5
182	1126	A	1	H	1	43.0	0.43	–3.7	–3.7
182	1126	A	1	H	1	51.0	0.51	–3.4	–3.4
182	1126	A	1	H	1	59.0	0.59	–3.4	–3.4
182	1126	A	1	H	1	67.0	0.67	–3.5	–3.5
182	1126	A	1	H	1	75.0	0.75	–3.8	–3.8
182	1126	A	1	H	1	83.0	0.83	–3.6	–3.6
182	1126	A	1	H	1	91.0	0.91	–3.8	–3.8
182	1126	A	1	H	1	99.0	0.99	–4.6	–4.6
182	1126	A	1	H	1	107.0	1.07	–4.5	–4.5
182	1126	A	1	H	1	115.0	1.15	–5.0	–5.0
182	1126	A	1	H	1	123.0	1.23	–4.6	–4.6
182	1126	A	1	H	1	131.0	1.31	–4.7	–4.7
182	1126	A	1	H	1	139.0	1.39	–4.9	–4.9
182	1126	A	1	H	2	3.0	1.47	–2.2	–2.2
182	1126	A	1	H	2	11.0	1.55	–2.3	–2.3
182	1126	A	1	H	2	19.0	1.63	–2.3	–2.3
182	1126	A	1	H	2	27.0	1.71	–2.1	–2.1
182	1126	A	1	H	2	35.0	1.79	–2.1	–2.1
182	1126	A	1	H	2	43.0	1.87	–2.5	–2.5
182	1126	A	1	H	2	51.0	1.95	–2.5	–2.5
182	1126	A	1	H	2	59.0	2.03	–2.8	–2.8
182	1126	A	1	H	2	67.0	2.11	–2.8	–2.8
182	1126	A	1	H	2	75.0	2.19	–3.2	–3.2
182	1126	A	1	H	2	83.0	2.27	–3.3	–3.3
182	1126	A	1	H	2	91.0	2.35	–3.1	–3.1
182	1126	A	1	H	2	99.0	2.43	–3.3	–3.3
182	1126	A	1	H	2	107.0	2.51	–3.3	–3.3
182	1126	A	1	H	2	115.0	2.59	–3.7	–3.7
182	1126	A	1	H	2	123.0	2.67	–3.5	–3.5
182	1126	A	1	H	2	131.0	2.75	–4.1	–4.1
182	1126	A	1	H	2	139.0	2.83	–3.9	–3.9
182	1126	A	1	H	3	3.0	2.97	–2.4	–2.4
182	1126	A	1	H	3	11.0	3.05	–2.6	–2.6
182	1126	A	1	H	3	19.0	3.13	–2.4	–2.4
182	1126	A	1	H	3	27.0	3.21	–2.7	–2.7
182	1126	A	1	H	3	35.0	3.29	–2.4	–2.4
182	1126	A	1	H	3	43.0	3.37	–2.8	–2.8
182	1126	A	1	H	3	51.0	3.45	–2.9	–2.9
182	1126	A	1	H	3	59.0	3.53	–2.8	–2.8
182	1126	A	1	H	3	67.0	3.61	–2.5	–2.5
182	1126	A	1	H	3	75.0	3.69	–2.4	–2.4
182	1126	A	1	H	3	83.0	3.77	–2.8	–2.8
182	1126	A	1	H	3	91.0	3.85	–2.3	–2.3
182	1126	A	1	H	3	99.0	3.93	–3.1	–3.1
182	1126	A	1	H	3	107.0	4.01	–2.8	–2.8
182	1126	A	1	H	3	115.0	4.09	–3.3	–3.3
182	1126	A	1	H	3	123.0	4.17	–3.4	–3.4
182	1126	A	1	H	3	131.0	4.25	–3.0	–3.0
182	1126	A	1	H	3	139.0	4.33	–2.5	–2.5
182	1126	A	1	H	4	3.0	4.47	–0.2	–0.2
182	1126	A	1	H	4	11.0	4.55	–0.2	–0.2
182	1126	A	1	H	4	19.0	4.63	–1.2	–1.2
182	1126	A	1	H	4	27.0	4.71	–1.6	–1.6
182	1126	A	1	H	4	35.0	4.79	–2.3	–2.3
182	1126	A	1	H	4	43.0	4.87	–2.4	–2.4
182	1126	A	1	H	4	51.0	4.95	–2.1	–2.1
182	1126	A	1	H	4	59.0	5.03	–1.7	–1.7
182	1126	A	1	H	4	67.0	5.11	–2.3	–2.3

Note: Only a portion of this table appears here. The complete table is available in **ASCII format.**

Table T13. Natural gamma-ray measurements from the multisensor track, Site 1126.

Leg	Site	Hole	Core	Type	Section	Interval (cm)	Depth (mbsf)	NGR (cps)
182	1126	A	1	H	1	3.0	0.03	4.62
182	1126	A	1	H	1	19.0	0.19	5.92
182	1126	A	1	H	1	35.0	0.35	7.54
182	1126	A	1	H	1	51.0	0.51	7.15
182	1126	A	1	H	1	67.0	0.67	5.08
182	1126	A	1	H	1	83.0	0.83	5.42
182	1126	A	1	H	1	99.0	0.99	5.92
182	1126	A	1	H	1	115.0	1.15	6.50
182	1126	A	1	H	1	131.0	1.31	6.42
182	1126	A	1	H	2	3.0	1.47	5.35
182	1126	A	1	H	2	19.0	1.63	7.00
182	1126	A	1	H	2	35.0	1.79	6.08
182	1126	A	1	H	2	51.0	1.95	7.15
182	1126	A	1	H	2	67.0	2.11	8.54
182	1126	A	1	H	2	83.0	2.27	7.96
182	1126	A	1	H	2	99.0	2.43	7.77
182	1126	A	1	H	2	115.0	2.59	5.77
182	1126	A	1	H	2	131.0	2.75	7.62
182	1126	A	1	H	3	3.0	2.97	5.85
182	1126	A	1	H	3	19.0	3.13	6.42
182	1126	A	1	H	3	35.0	3.29	6.15
182	1126	A	1	H	3	51.0	3.45	7.69
182	1126	A	1	H	3	67.0	3.61	6.35
182	1126	A	1	H	3	83.0	3.77	8.08
182	1126	A	1	H	3	99.0	3.93	8.08
182	1126	A	1	H	3	115.0	4.09	9.96
182	1126	A	1	H	3	131.0	4.25	9.12
182	1126	A	1	H	4	3.0	4.47	11.69
182	1126	A	1	H	4	19.0	4.63	13.39
182	1126	A	1	H	4	35.0	4.79	10.08
182	1126	A	1	H	4	51.0	4.95	8.73
182	1126	A	1	H	4	67.0	5.11	8.39
182	1126	A	1	H	4	83.0	5.27	9.77
182	1126	A	1	H	4	99.0	5.43	10.54
182	1126	A	1	H	4	115.0	5.59	11.00
182	1126	A	1	H	4	131.0	5.75	13.31
182	1126	A	1	H	5	3.0	5.97	8.08
182	1126	A	1	H	5	19.0	6.13	9.54
182	1126	A	1	H	5	35.0	6.29	9.27
182	1126	A	1	H	5	51.0	6.45	12.62
182	1126	A	1	H	5	67.0	6.61	10.85
182	1126	A	1	H	5	83.0	6.77	11.31
182	1126	A	1	H	5	99.0	6.93	11.00
182	1126	A	1	H	5	115.0	7.09	9.77
182	1126	A	1	H	5	131.0	7.25	8.69
182	1126	A	1	H	5	147.0	7.41	7.15
182	1126	A	1	H	6	3.0	7.47	7.39
182	1126	A	1	H	6	19.0	7.63	9.27
182	1126	A	1	H	6	35.0	7.79	10.19
182	1126	A	1	H	6	51.0	7.95	12.23
182	1126	A	1	H	6	67.0	8.11	13.00
182	1126	A	1	H	6	83.0	8.27	12.69
182	1126	A	1	H	6	99.0	8.43	13.77
182	1126	A	1	H	6	115.0	8.59	16.73
182	1126	A	1	H	6	131.0	8.75	11.46
182	1126	A	1	H	7	3.0	8.97	9.50
182	1126	A	1	H	7	19.0	9.13	13.31
182	1126	A	1	H	7	35.0	9.29	12.73
182	1126	A	1	H	7	51.0	9.45	10.85
182	1126	B	1	H	1	3.0	0.03	5.15
182	1126	B	1	H	1	19.0	0.19	5.12
182	1126	B	1	H	1	35.0	0.35	4.69
182	1126	B	1	H	1	51.0	0.51	4.89
182	1126	B	1	H	1	67.0	0.67	3.31

Notes: NGR = natural gamma radiation. Only a portion of this table appears here. The complete table is available in **ASCII format.**

Table T14. Thermal conductivity measurements, Site 1126.

Leg	Site	Hole	Core	Type	Section	Interval (cm)	Depth (mbsf)	Thermal conductivity (W/[m·K])	Standard deviation
182	1126	B	1	H	3	75.0	3.75	0.939	0.006
182	1126	B	2	H	3	75.0	10.25	1.009	0.024
182	1126	B	3	H	3	75.0	19.75	1.063	0.014
182	1126	B	4	H	3	75.0	29.25	1.102	0.010
182	1126	B	5	H	3	75.0	38.75	1.088	0.021
182	1126	B	6	H	3	75.0	48.25	1.114	0.042
182	1126	B	7	H	3	75.0	57.75	1.238	0.049
182	1126	B	8	H	3	75.0	67.25	1.192	0.023
182	1126	B	9	H	3	75.0	76.75	1.261	0.040
182	1126	B	10	H	3	75.0	86.25	1.270	0.033
182	1126	B	11	H	3	75.0	95.75	1.238	0.022
182	1126	B	12	H	1	60.0	102.10	1.173	0.010
182	1126	B	14	H	3	75.0	113.25	1.157	0.045
182	1126	B	15	H	3	44.0	122.44	1.102	0.012
182	1126	B	17	H	3	75.0	132.55	1.136	0.017
182	1126	B	18	H	3	75.0	142.05	1.236	0.014
182	1126	B	19	H	3	75.0	151.55	1.014	0.018
182	1126	B	20	H	2	75.0	159.55	1.216	0.024
182	1126	B	22	X	1	75.0	167.95	0.977	0.006
182	1126	B	24	X	1	75.0	187.25	1.166	0.020
182	1126	B	27	X	4	75.0	220.55	1.045	0.026
182	1126	B	28	X	2	75.0	227.15	1.170	0.009
182	1126	B	29	X	2	75.0	236.75	1.228	0.015
182	1126	B	32	X	1	75.0	254.45	1.312	0.019
182	1126	C	1	H	3	75.0	3.75	0.990	0.015
182	1126	C	2	H	3	75.0	12.25	1.182	0.017
182	1126	C	3	H	3	75.0	21.75	1.017	0.033
182	1126	C	4	H	1	55.0	28.05	0.988	0.021
182	1126	C	4	H	3	55.0	31.05	1.101	0.050
182	1126	C	4	H	5	55.0	34.05	1.116	0.065
182	1126	C	5	H	3	75.0	40.75	1.109	0.017
182	1126	C	6	H	3	75.0	50.25	1.168	0.022
182	1126	C	6	H	1	75.0	47.25	1.037	0.017
182	1126	C	6	H	5	75.0	53.25	1.103	0.011
182	1126	C	7	H	3	100.0	60.00	1.287	0.027
182	1126	C	8	H	1	100.0	66.50	1.299	0.019
182	1126	C	8	H	3	100.0	69.50	1.173	0.137
182	1126	C	9	H	3	75.0	78.75	1.276	0.034
182	1126	C	10	X	3	75.0	88.25	1.181	0.026
182	1126	C	11	X	3	75.0	94.05	1.097	0.008
182	1126	C	12	X	3	75.0	103.65	1.086	0.020
182	1126	C	13	X	3	75.0	113.25	1.081	0.032
182	1126	C	14	X	3	75.0	122.85	1.119	0.057
182	1126	C	15	X	3	75.0	132.45	1.089	0.056
182	1126	C	16	H	3	75.0	142.15	1.194	0.027
182	1126	C	17	X	3	75.0	148.15	1.174	0.080

Note: This table is also available in **ASCII format.**

Table T15. Discrete *P*-wave velocity from measurements using PWS1, PWS2, and PWS3; Site 1126.

Leg	Site	Hole	Core	Type	Section	Interval (cm)	Depth (mbsf)	PWS 1, 2, or 3	V_p (km/s)
182	1126	B	1	H	1	0.65	0.65	1	1.5842
182	1126	B	1	H	1	0.65	0.65	2	1.6002
182	1126	B	1	H	1	1.33	1.33	1	1.5754
182	1126	B	1	H	1	1.33	1.33	2	1.5732
182	1126	B	1	H	2	0.65	2.15	1	1.5809
182	1126	B	1	H	2	0.65	2.15	2	1.5781
182	1126	B	1	H	2	1.36	2.86	1	1.5748
182	1126	B	1	H	2	1.36	2.86	2	1.5710
182	1126	B	1	H	3	0.65	3.65	1	1.5935
182	1126	B	1	H	3	0.65	3.65	2	1.5867
182	1126	B	1	H	3	1.24	4.24	1	1.5782
182	1126	B	1	H	3	1.24	4.24	2	1.5818
182	1126	B	1	H	4	0.65	5.15	1	1.5842
182	1126	B	1	H	4	0.65	5.15	2	1.5795
182	1126	B	1	H	4	1.34	5.84	1	1.6056
182	1126	B	1	H	4	1.34	5.84	2	1.6122
182	1126	B	1	H	5	0.29	6.29	1	1.6037
182	1126	B	1	H	5	0.29	6.29	2	1.6313
182	1126	B	2	H	1	0.5	7.00	1	1.5988
182	1126	B	2	H	1	1.3	7.80	1	1.5879
182	1126	B	2	H	1	0.5	7.00	2	1.5867
182	1126	B	2	H	1	1.3	7.80	2	1.5897
182	1126	B	2	H	2	0.51	8.51	1	1.5886
182	1126	B	2	H	2	1.3	9.30	1	1.5790
182	1126	B	2	H	2	0.51	8.51	2	1.6090
182	1126	B	2	H	2	1.3	9.30	2	1.5625
182	1126	B	2	H	3	0.5	10.00	1	1.5736
182	1126	B	2	H	3	1.3	10.80	1	1.5649
182	1126	B	2	H	3	0.5	10.00	2	1.5840
182	1126	B	2	H	3	1.3	10.80	2	1.5674
182	1126	B	2	H	4	0.5	11.50	1	1.5679
182	1126	B	2	H	4	1.3	12.30	1	1.5730
182	1126	B	2	H	4	0.5	11.50	2	1.5787
182	1126	B	2	H	4	1.3	12.30	2	1.5865
182	1126	B	2	H	5	0.5	13.00	1	1.5882
182	1126	B	2	H	5	1.3	13.80	1	1.5763
182	1126	B	2	H	5	0.5	13.00	2	1.5818
182	1126	B	2	H	5	1.3	13.80	2	1.5871
182	1126	B	2	H	6	0.5	14.50	1	1.5658
182	1126	B	2	H	6	1.3	15.30	1	1.5827
182	1126	B	2	H	6	0.5	14.50	2	1.5590
182	1126	B	2	H	6	1.3	15.30	2	1.5885
182	1126	B	3	H	1	0.64	16.64	1	1.5893
182	1126	B	3	H	1	1.3	17.30	1	1.5984
182	1126	B	3	H	1	0.64	16.64	2	1.6160
182	1126	B	3	H	1	1.3	17.30	2	1.6065
182	1126	B	3	H	2	0.5	18.00	1	1.6147
182	1126	B	3	H	2	1.3	18.80	1	1.5876
182	1126	B	3	H	2	0.5	18.00	2	1.6287
182	1126	B	3	H	2	1.3	18.80	2	1.5940
182	1126	B	3	H	2	0.9	18.40	3	1.6450
182	1126	B	3	H	3	0.5	19.50	1	1.6071
182	1126	B	3	H	3	1.3	20.30	1	1.6138
182	1126	B	3	H	3	0.5	19.50	2	1.6104
182	1126	B	3	H	3	1.3	20.30	2	1.6185
182	1126	B	3	H	3	0.9	19.90	3	1.6626
182	1126	B	3	H	4	0.5	21.00	1	1.6314
182	1126	B	3	H	4	1.3	21.80	1	1.6497
182	1126	B	3	H	4	0.5	21.00	2	1.6563
182	1126	B	3	H	4	1.3	21.80	2	1.6650
182	1126	B	3	H	4	0.8	21.30	3	1.7811
182	1126	B	3	H	5	0.5	22.50	1	1.6330
182	1126	B	3	H	5	1.3	23.30	1	1.6695
182	1126	B	3	H	5	0.5	22.50	2	1.6204

Note: Only a portion of this table appears here. The complete table is available in **ASCII format.**

Table T16. Index properties measurements, Site 1126.

Leg	Site	Hole	Core	Type	Section	Top (cm)	Bottom (cm)	Depth (mbsf)	Bulk water content (%)	Dry water content (%)	Bulk density (g/cm^3)	Dry density (g/cm^3)	Grain density (g/cm^3)	Porosity (%)	Void ratio
182	1126	B	1	H	1	89.0	91.0	0.89	35.1	54.0	1.71	1.11	2.68	58.5	1.41
182	1126	B	1	H	2	89.0	91.0	2.39	36.8	58.2	1.68	1.06	2.66	60.2	1.52
182	1126	B	1	H	3	89.0	91.0	3.89	37.1	59.0	1.67	1.05	2.67	60.6	1.54
182	1126	B	1	H	4	89.0	91.0	5.39	33.9	51.3	1.73	1.14	2.67	57.2	1.34
182	1126	B	1	H	5	14.0	17.0	6.14	35.7	55.6	1.70	1.10	2.70	59.4	1.47
182	1126	B	2	H	1	89.0	91.0	7.39	34.2	52.0	1.73	1.14	2.70	57.8	1.37
182	1126	B	2	H	2	89.0	91.0	8.89	36.7	58.0	1.68	1.06	2.67	60.1	1.51
182	1126	B	2	H	3	89.0	91.0	10.39	37.2	59.3	1.68	1.05	2.70	61.0	1.57
182	1126	B	2	H	4	89.0	91.0	11.89	35.7	55.5	1.71	1.10	2.71	59.5	1.47
182	1126	B	2	H	5	89.0	91.0	13.39	34.8	53.4	1.71	1.12	2.67	58.2	1.39
182	1126	B	2	H	6	89.0	91.0	14.89	35.6	55.3	1.70	1.10	2.68	59.1	1.45
182	1126	B	3	H	1	89.0	91.0	16.89	35.3	54.6	1.71	1.11	2.71	59.1	1.45
182	1126	B	3	H	1	93.0	95.0	16.93	35.1	54.0	1.71	1.11	2.67	58.5	1.41
182	1126	B	3	H	2	89.0	91.0	18.39	34.7	53.1	1.72	1.12	2.69	58.3	1.40
182	1126	B	3	H	2	93.0	95.0	18.43	34.5	52.6	1.74	1.14	2.76	58.6	1.42
182	1126	B	3	H	3	89.0	91.0	19.89	32.6	48.3	1.76	1.19	2.69	55.9	1.27
182	1126	B	3	H	3	92.0	94.0	19.92	32.7	48.5	1.76	1.18	2.69	56.1	1.28
182	1126	B	3	H	3	122.0	124.0	20.22	35.3	54.6	1.71	1.11	2.70	59.0	1.44
182	1126	B	3	H	4	89.0	91.0	21.39	34.4	52.5	1.72	1.13	2.68	57.8	1.37
182	1126	B	3	H	5	89.0	91.0	22.89	29.8	42.4	1.81	1.27	2.67	52.5	1.11
182	1126	B	3	H	6	89.0	91.0	24.39	33.7	50.8	1.73	1.15	2.67	57.0	1.33
182	1126	B	3	H	7	24.5	27.0	25.25	28.8	40.4	1.84	1.31	2.70	51.6	1.07
182	1126	B	4	H	1	89.0	91.0	26.39	29.7	42.3	1.82	1.28	2.70	52.7	1.11
182	1126	B	4	H	2	89.0	91.0	27.89	31.7	46.4	1.77	1.21	2.68	54.8	1.22
182	1126	B	4	H	3	89.0	91.0	29.39	28.5	39.9	1.83	1.31	2.68	51.1	1.04
182	1126	B	4	H	4	84.0	85.0	30.84	31.6	46.2	1.78	1.21	2.68	54.8	1.21
182	1126	B	4	H	5	89.0	91.0	32.39	32.2	47.6	1.76	1.19	2.68	55.4	1.24
182	1126	B	4	H	6	89.0	91.0	33.89	31.4	45.9	1.77	1.21	2.66	54.4	1.19
182	1126	B	4	H	6	119.0	121.0	34.19	35.1	54.1	1.71	1.11	2.67	58.5	1.41
182	1126	B	5	H	2	89.0	91.0	37.39	32.2	47.6	1.75	1.19	2.66	55.2	1.23
182	1126	B	5	H	3	89.0	91.0	38.89	33.9	51.3	1.73	1.14	2.67	57.2	1.34
182	1126	B	5	H	4	90.0	92.0	40.40	31.9	46.8	1.76	1.20	2.63	54.6	1.20
182	1126	B	5	H	5	89.0	91.0	41.89	28.3	39.5	1.80	1.29	2.56	49.6	0.99
182	1126	B	5	H	6	22.0	24.0	42.72	28.9	40.7	1.82	1.29	2.67	51.5	1.06
182	1126	B	6	H	1	71.0	73.0	45.21	34.8	53.3	1.71	1.11	2.64	57.9	1.38
182	1126	B	6	H	1	89.0	91.0	45.39	29.5	41.9	1.80	1.27	2.64	52.0	1.08
182	1126	B	6	H	2	89.0	91.0	46.89	32.5	48.1	1.75	1.18	2.67	55.6	1.25
182	1126	B	6	H	3	89.0	91.0	48.39	30.1	43.0	1.80	1.26	2.68	52.9	1.12
182	1126	B	6	H	4	89.0	91.0	49.89	23.4	30.6	1.93	1.47	2.64	44.1	0.79
182	1126	B	6	H	5	89.0	91.0	51.39	23.6	30.8	1.88	1.43	2.52	43.1	0.76
182	1126	B	6	H	6	89.0	91.0	52.89	27.8	38.5	1.79	1.29	2.50	48.5	0.94
182	1126	B	7	H	1	89.0	91.0	54.89	33.0	49.3	1.74	1.17	2.66	56.2	1.28
182	1126	B	7	H	2	89.0	91.0	56.39	30.8	44.4	1.77	1.22	2.60	53.0	1.13
182	1126	B	7	H	3	89.0	91.0	57.89	29.2	41.1	1.79	1.27	2.59	51.0	1.04
182	1126	B	7	H	4	89.0	91.0	59.39	31.7	46.5	1.77	1.21	2.66	54.7	1.21
182	1126	B	7	H	5	89.0	91.0	60.89	27.5	38.0	1.86	1.35	2.71	50.1	1.01
182	1126	B	7	H	6	89.0	91.0	62.39	27.1	37.2	1.86	1.35	2.67	49.2	0.97
182	1126	B	7	H	7	59.0	61.0	63.59	26.8	36.7	1.87	1.36	2.67	48.9	0.96
182	1126	B	8	H	1	89.0	91.0	64.39	25.8	34.8	1.89	1.40	2.67	47.6	0.91
182	1126	B	8	H	2	89.0	91.0	65.89	26.8	36.6	1.88	1.38	2.71	49.2	0.97
182	1126	B	8	H	3	89.0	91.0	67.39	29.4	41.7	1.81	1.28	2.65	51.9	1.08
182	1126	B	8	H	4	89.0	91.0	68.89	28.6	40.1	1.80	1.29	2.59	50.4	1.01
182	1126	B	8	H	5	89.0	91.0	70.39	29.7	42.2	1.80	1.27	2.64	52.1	1.09
182	1126	B	8	H	6	89.0	91.0	71.89	26.7	36.5	1.83	1.34	2.57	47.8	0.92
182	1126	B	9	H	1	89.0	91.0	73.89	44.2	79.4	1.56	0.87	2.68	67.5	2.08
182	1126	B	9	H	2	89.0	91.0	75.39	30.8	44.5	1.75	1.21	2.54	52.5	1.11
182	1126	B	9	H	3	89.0	91.0	76.89	29.9	42.7	1.80	1.26	2.66	52.6	1.11
182	1126	B	9	H	4	89.0	91.0	78.39	26.2	35.4	1.85	1.37	2.59	47.3	0.90
182	1126	B	9	H	5	89.0	91.0	79.89	32.7	48.6	1.75	1.17	2.65	55.7	1.26
182	1126	B	9	H	6	89.0	91.0	81.39	30.7	44.2	1.77	1.22	2.60	52.9	1.12
182	1126	B	10	H	2	89.0	91.0	84.89	29.2	41.3	1.81	1.28	2.66	51.7	1.07
182	1126	B	10	H	3	89.0	91.0	86.39	29.2	41.3	1.82	1.29	2.67	51.8	1.08
182	1126	B	10	H	4	40.0	41.0	87.40	29.1	41.0	1.82	1.29	2.66	51.6	1.07
182	1126	B	10	H	5	69.0	71.0	88.29	28.5	39.9	1.83	1.31	2.67	50.9	1.04
182	1126	B	11	H	1	89.0	91.0	92.89	28.1	39.1	1.84	1.32	2.67	50.5	1.02

Note: Only a portion of this table appears here. The complete table is available in **ASCII format.**

Table T17. Undrained shear strength measurements, Site 1126.

Leg	Site	Hole	Core	Type	Section	Interval (cm)	Depth (mbsf)	Maximum shear strength (kPa)	Peak (kPa)
182	1126	B	3	H	4	117.0	21.67	16.20	19.76
182	1126	B	3	H	5	110.0	23.10	14.58	17.78
182	1126	B	3	H	6	109.9	24.60	7.74	9.44
182	1126	B	3	H	7	41.9	25.42	15.03	18.33
182	1126	B	4	H	1	110.1	26.60	3.87	4.72
182	1126	B	4	H	2	110.0	28.10	8.91	10.87
182	1126	B	4	H	3	110.1	29.60	8.91	10.87
182	1126	B	4	H	4	110.5	31.10	9.45	11.53
182	1126	B	4	H	5	110.3	32.60	13.86	16.90
182	1126	B	4	H	6	110.1	34.10	3.87	4.72
182	1126	B	4	H	7	25.1	34.75	14.49	17.67
182	1126	B	5	H	2	110.1	37.60	6.39	7.79
182	1126	B	5	H	3	110.0	39.10	10.17	12.40
182	1126	B	5	H	4	110.0	40.60	11.61	14.16
182	1126	B	5	H	5	109.9	42.10	6.93	8.45
182	1126	B	5	H	6	66.0	43.16	8.73	10.65
182	1126	B	6	H	1	110.1	45.60	8.55	10.43
182	1126	B	6	H	2	110.1	47.10	21.42	26.13
182	1126	B	6	H	3	109.9	48.60	14.13	17.23
182	1126	B	6	H	4	110.0	50.10	7.47	9.11
182	1126	B	6	H	5	110.9	51.61	8.73	10.65
182	1126	B	6	H	6	106.6	53.07	12.24	14.93
182	1126	B	7	H	1	110.7	55.11	12.24	14.93
182	1126	B	7	H	2	110.1	56.60	12.51	15.26
182	1126	B	7	H	3	110.8	58.11	11.34	13.83
182	1126	B	7	H	4	113.1	59.63	6.21	7.57
182	1126	B	7	H	5	110.3	61.10	11.43	13.94
182	1126	B	7	H	6	110.8	62.61	14.13	17.23
182	1126	B	7	H	7	63.0	63.63	14.49	17.67
182	1126	B	8	H	1	110.6	64.61	5.58	6.81
182	1126	B	8	H	2	97.9	65.98	11.34	13.83
182	1126	B	8	H	3	110.6	67.61	33.84	41.27
182	1126	B	8	H	4	108.8	69.09	24.75	30.19
182	1126	B	8	H	4	108.8	69.09	24.75	30.19
182	1126	B	8	H	5	109.6	70.60	18.00	21.95
182	1126	B	8	H	6	110.6	72.11	17.01	20.75
182	1126	B	9	H	2	110.6	75.61	9.00	10.98
182	1126	B	9	H	3	110.5	77.11	7.11	8.67
182	1126	B	9	H	4	109.9	78.60	8.82	10.76
182	1126	B	9	H	5	110.0	80.10	12.60	15.37
182	1126	B	9	H	6	96.6	81.47	9.63	11.75
182	1126	B	10	H	2	110.7	85.11	6.12	7.46
182	1126	B	10	H	3	109.9	86.60	4.95	6.04
182	1126	B	10	H	5	67.8	88.28	7.47	9.11
182	1126	B	11	H	1	110.7	93.11	34.11	41.60
182	1126	B	11	H	2	107.6	94.58	19.17	23.38
182	1126	B	11	H	3	118.4	96.18	42.84	52.25
182	1126	B	11	H	4	107.2	97.57	15.84	19.32
182	1126	B	11	H	5	85.0	98.85	19.17	23.38
182	1126	B	11	H	6	110.8	100.61	2.88	3.51
182	1126	B	11	H	7	83.0	101.83	4.14	5.05
182	1126	B	12	H	1	106.0	102.56	20.07	24.48
182	1126	B	12	H	2	89.9	103.63	3.87	4.72
182	1126	B	14	H	2	109.3	112.09	12.96	15.81
182	1126	B	14	H	3	109.8	113.60	21.42	26.13
182	1126	B	14	H	4	113.8	115.14	9.81	11.97
182	1126	B	14	H	5	109.7	116.60	8.73	10.65
182	1126	B	14	H	6	105.5	118.06	30.15	36.77
182	1126	B	15	H	1	70.6	119.71	15.66	19.10
182	1126	B	17	H	2	100.0	131.30	14.76	18.00
182	1126	B	17	H	3	105.0	132.85	25.20	30.74
182	1126	B	17	H	4	105.0	134.35	19.89	24.26
182	1126	B	17	H	5	100.0	135.80	30.33	36.99
182	1126	B	18	H	1	116.1	139.46	24.03	29.31

Note: Only a portion of this table appears here. The complete table is available in **ASCII format.**

Table T18. Summary of tool strings, intervals logged, and logging speeds, Hole 1126D.

Tool string	First pass		Second pass	
	Interval (mbsf)	Speed (m/hr)	Interval (mbsf)	Speed (m/hr)
Triple combo/LDEO-TAP	0-443 (QC)	275	0-439 (main)	275
Sonic/GHMT	1-430 (main)	550		

Note: LDEO-TAP = Lamont-Doherty Earth Observatory temperature/acceleration/pressure tool, QC = quality control run, main = main logging run, GHMT = geologic high-resolution magnetic tool.

Table T19. Differences between depths to seismic horizons and corrected depths, Site 1126.

Seismic horizons	Predicted intersection (mbsf)	Check-shot corrected depth (mbsf)	Difference (m)
Base of Sequence 2	46		
Sequence 3, Horizon A	70		
Sequence 3, Horizon B	108	120	+12
Sequence 3, Horizon C	136	150	+14
Base of Sequence 3	166	180	+14
Top of Sequence 6A	212	227	+15
Top of Sequence 6A, Lobe 1	305	321	+16
Base of Cenozoic	381	398	

Notes: Predicted intersection depths were derived using high-resolution site-survey seismic data stacking velocities. Corrected depths were based on check-shot data and interval transit-time (ITT) data.